POLITECNICO DI MILANO

Facoltà in Ingegneria Industriale

Corso di Laurea in Ingegneria Aeronautica

"Assessment of advanced time integration approaches for Contra-Rotating Open Rotor simulations"

Relatore: Prof. Luigi Vigevano
Correlatore: Dr. Guillaume Dufour

Marco Burnazzi matr. 725575

Anno Accademico 2009/2010

Acknowledgement

Starting from the realization of this work, I deeply thank the whole AAM Cerfacs team to have been a trustworthy refuge to protect myself from the fury of *elsA*, providing answers and help, but always leaving me the place for my enthusiasm and to form my own CFD experience. In particular I would like to acknowledge my tutor Guillaume, to find every time the right suggestion to improve the quality of my work, giving me motivation and confidence. A last huge thanks is dedicated to all the other trainee students that have shared the office with me, which includes sweat, desperation, laughs and a lot of coffees.

On the university side I thank my supervisor professor Vigevano, to have been very helpful during the report revision.

I am grateful to my girlfriend Emilie. She has waited for me late in the night till I had finished my work, and brought a light of serenity in the gray days I passed between the office and the bed.

I also thank the other people who have made possible this experience, from all the friends I knew during my Erasmus year in Toulouse, to the dear fellows who have made these years in Milan a sequence of parties, dinners, Briscola matches and, of course, hours and hours of team working. In particular I am grateful to Domenico, who shared my passion for the aviation since we discovered what an airplane is, eleven years ago.

Finally a very special thanks to my parents, who supported me during all these years, increasing my enthusiasm, sharing my efforts and bringing wisdom to my choices.

Contents

List of Figures

List of Tables

Abstract

The industrial application of contra-rotating open rotor configurations may represent a milestone in the evolution of aeronautical propulsion systems. In fact these kinds of propeller allow to obtain a very high gain of efficiency, thanks to the low swirl component present in the wake and the high by-pass ratio. This principle is not a new idea, but problems related to noise emissions and installation effects have prevented its application from being diffused in a large industrial context during the last thirty years. Nowadays the interest in this technical solution is supported by economic and environmental motivations as well as innovative mathematical and computational capabilities.

The goal of this work is the set up of CROR CFD simulations by using the *elsA* code, developed by Cerfacs and Onera. The main purpose is the application of unsteady time integration methods, in order to allow a complete analysis of rotor-rotor interactions. Therefore the challenge of the presented calculations is the assessment of some simulation techniques typically used in turbomachine analysis, in a context of external aerodynamics. In particular the steady mixing plane technique and the unsteady chorochronic approach have been applied.

The simulation set up is presented through the steps of physical consistency analysis, verification and validation. These three sections represent the whole process from the prediction of the reality, to the analysis of the results. This allows to show all the particularities that have been brought to light in the use of the mesh generator Autogrid, the solver elsA, and in the post-processing of the results.

Keywords
Contra-rotating open rotor, CROR, phase lag, mixing plane, unsteady turbomachine simulations, RANS

Sommario

L'applicazione industriale della configurazione a rotori non carenati contro-rotanti può costituire un vera e propria svolta nell'evoluzione dei sistemi propulsivi aeronautici. Questo tipo di eliche, infatti, assicura un elevato incremento di efficienza grazie alla ridotta componente di velocità tangenziale nella scia e all'altissimo rapporto di diluizione che è possibile ottenere senza carenatura. Tale configurazione non si basa su un principio innovativo, ma una sua larga diffusione in ambito industriale è stata impedita durante gli ultimi trent'anni da problemi legati all'elevato rumore e a fenomeni di accoppiamento aeroelastico con il resto del velivolo. Oggi l'interesse verso questa soluzione tecnica è rinato supportato da motivazioni economiche e ambientali che possono basarsi su metodi numerici innovativi ed elevate potenze di calcolo.

L'obiettivo di questo lavoro è la messa a punto di simulazioni numeriche di rotori non carenati contro-rotanti utilizzando il codice *elsA*, sviluppato da Cerfacs e Onera. Lo scopo principale

è l'applicazione di metodi d'integrazione temporale non stazionari, al fine di permettere una completa e accurata analisi delle interazioni tra i due rotori. La peculiarità di questo studio è quindi costituita dall'utilizzo di tecniche di simulazione specifiche per analisi di turbomacchine, in un contesto di aerodinamica esterna. In particolare sono stati utilizzati gli approcci mixing-plane e chorochronic.

La trattazione presenta le tre fasi che costituiscono il processo di simulazione, dalla previsione della fisica da modellare, all'analisi dei risultati: analisi fisica, verifica e validazione. Esse permettono di illustrare gli elementi che contraddistinguono il caso in esame rispetto alla simulazione di una turbomacchina convenzionale. In particolare le seguenti peculiarità sono emerse nell'utilizzo del programma di generazione della griglia e nell'applicazione dei metodi di integrazione temporale per il calcolo non stazionario:

- bassa qualità della griglia nelle zone del dominio più lontane dall'asse di rotazione della macchina;
- elevato numero di punti necessari per un'accurata simulazione dei fenomeni d'interazione tra i rotori e delle dinamiche d'estremità di pala (vortici d'estremità e fenomeni di comprimibilità);
- passo temporale estremamente ridotto rispetto a quelli tipicamente utilizzati in simulazioni di turbomacchine convenzionali (fino a 15 volte più piccolo).

Il primo punto trova la sua motivazione nella tecnica di generazione della griglia utilizzata. É innanzi tutto necessario specificare che non è attualmente possibile utilizzare una griglia non strutturata con il codice *elsA*, quindi la scelta è stata obbligata verso una griglia strutturata. Il programma Autogrid consente di ottenere tale tipo di mesh in maniera semi-automatica, essendo sviluppato specificatamente per turbomacchine. Tuttavia la presenza del campo esterno, cioè al di sopra delle estremità delle pale, non rientra nelle configurazioni previste dal programma, in quanto questo è tipicamente utilizzato per ambiti di aerodinamica interna. Quindi i punti, la cui distribuzione può essere controllata su piani a raggio costante fino all'altezza delle pale, vengono proiettati automaticamente sulla superficie esterna del cilindro che costituisce il domino numerico ed è distante dall'asse circa cinque volte l'apertura delle pale. Le celle della mesh che si trovano nelle zone esterne hanno quindi forme decisamente irregolari.

Tale condizione è probabilmente una delle ragioni per la quale non è stato possibile applicare la formulazione di velocità relativa, di comune utilizzo in simulazioni di turbomacchine. Tale formulazione è basata sull'espressione delle grandezze cinematiche secondo il sistema di riferimento locale, cioè che segue le pale nel loro moto di rotazione. Quindi attraversando il piano di interfaccia tra i due rotori, le incognite del flusso subirebbero una forte discontinuità, passando da un sistema di riferimento all'altro. La formulazione utilizzata è stata quindi quella che esprime la velocità secondo il sistema riferimento globale. Tale variazione dalle consuetudini non comporta alcuna limitazione teorica, ma necessita di alcune accortezze nell'applicazione dei metodi di simulazione mixing plane e chorochronic e nell'analisi dei risultati.

Anche dal punto di vista della discretizzazione temporale si sono riscontrate alcune particolarità. Infatti l'analisi di convergenza del passo temporale ha evidenziato la necessità di intervalli estremamente ridotti rispetto a quelli deducibili dalle caratteristiche geometriche e di funzionamento dei rotori con i parametri tipicamente utilizzati per analisi di compressori, turbine o fan. Questo implica l'esistenza di fenomeni aerodinamici caratterizzati da una frequenza molto più alta della "blade passing frequency", come, ad esempio, i vortici d'estremità.

L'analisi dei risultati ha consentito di valutare l'effetto dei metodi numerici, dei modelli di turbolenza e delle tecniche d'integrazione temporale.

Infine il funzionamento del sistema è stato studiato in maniera qualitativa dimostrando la fisicità dei risultati ottenuti.

Parole chiave
rotori contro-rotanti, chorochronic, mixing plane, turbomacchine, RANS

Chapter 1

Introduction

Contents

1.1 Context and motivation

Since the birth of the aviation, the success of aeronautical companies has always been based on the ability to find the right solutions to the numerous problems prompted by the wish to improve flight performances. Notably in this field a "right" solution is the most efficient but also the cheapest idea to reach the goal. This is why in more than a century, since the first human powered flight, the aeronautical history has been full of bright intuitions, often born by simple feelings raised by experience and observation of physical phenomena. Nevertheless the biggest challenge has always been to achieve the idea with the available technologies. This has led to compromises between physical requests and technological limitations. That is why new technologies could now allow to solve the problems which have prevented some ideas from being realized. This work is actually part of one of these attempts.

In the context of significantly increased costs of fuel a consensus has emerged among airframers, engine manufacturers and airliners: future commercial transport aircraft must deliver significant improvements in operating costs, through both efficiency improvements and maintenance cost reductions. This has brought the Contra Rotating Open Rotor (CROR), also simply referred to as Open Rotor, back into focus, as this propulsion system promises a step change in efficiency levels over turbofan engines due to its ultra high bypass ratio. The principle of creating thrust by imparting a little acceleration to a big mass of air is already used by conventional turboprops but, at high flight speeds, propellers suffer from a rapid loss of efficiency caused by increased compressibility effects. An advanced contra-rotating open rotor engine may extend the fuel efficiency of a turboprop, usually limited to Mach values around 0.7, to Mach 0.8. Nonetheless that is still less than the typical operating regime of modern commercial turbofan-powered aircrafts [1]. Therefore the open rotors represent an effective

solution particularly for the single-aisle transport aircraft class, now dominated by the Airbus A320 and the Boeing B737 families.

CROR powerplants had previously been the focus of a large research undertaking led by NASA and the US industry in the late 1970s and 1980s, motivated by the high fuel costs arising from the 1973 oil crisis. Significant advances in the development of CROR engines were achieved, but primarily due to the decrease in oil prices that followed, interest in bringing these engines to market waned. With today's revived interest in this propulsion system, out of economic and environmental considerations, the largest challenge for the realization of such a commercially viable engine relates to the issue of noise emissions and installation effects with the airframe. The rapid improvement of numerical methods in aerodynamics and aeroacoustics achieved in recent years have enabled these tools to play an important role in the research and design of CRORs to address these concerns.

The first methods that have been employed, of increasing complexity and computational cost, include the lifting line, transonic potential and Euler calculations [2]. The lifting line methods represent each propeller blade by a single line of bound vorticity at the blade quarter-chord location and include effects of twist and sweep. Although the required computational time for these methods is very low, their treatment of compressibility is approximate and the results give a limited amount of flow field information. This led to the development of the transonic potential method. This approach yields detailed blade surface flow properties and information about the flow field around the propeller. However, at the beginning of 1990s, state-of-the-art Euler methods were the most accurate. Euler methods have a demonstrated capability for predicting both steady and unsteady high-speed propeller flow fields, but cannot reveal any information regarding viscous phenomena.

(a) **(b)**

Figure 1.1: Example of studied CROR configurations (source: web)

To enable further improvements in open rotor aerodynamics and performance prediction, more sophisticated numerical methods are required such as full three-dimensional Navier-Stokes calculations. This approach gives greater detail especially in the areas of boundary layer development and viscous wakes, which are actually the phenomena at the origin of the acoustics and structure integration problems that still prevent CRORs to be used. Therefore taking into account viscosity effects is fundamental to analyze and find solutions to these concerns. Moreover this kind of dynamics has an unsteady inherent nature which rises the need of specific

time integration methods to numerically model the interactions between the two rotors. The present work finds his motivation from this context, assessing advanced classical turbomachinery methods applied to an Open Rotor configuration.

Many of the difficulties encountered in the application of a Navier-Stokes solver to an open rotor arise because of the removal of the casing that is present in conventional arranging turbomachinery. The lack of an outer solid wall requires a new meshing strategy and careful application of boundary conditions in the far-field. The combination of turbomachinery and external aerodynamics flows makes the analysis of open rotor configurations a real challenge. The computational mesh needs to give good resolution of the important flow features near the blade surface such as the boundary layers, the regions of transonic flow, wakes and the tip vortex formation, but also extend a significant distance away from the open rotor to a location where appropriate boundary conditions can be imposed.

1.2 Working principle

The benefit of two contra-rotating propellers is quite clearly visible by simple considerations based on the third principle of dynamics. If the motion of the accelerated air flow after the propulsion system is parallel to the direction of flight, the thrust will be maximum, while every tangential component of the velocity vector is a loss of energy. Unfortunately a well known effect of a traditional propeller is the presence of a strong rotating slipstream. Therefore to obtain a straight flow after the propulsion system a new component of motion is necessary. From this simple consideration the idea of a second propeller turning in the opposite direction is born.

In particular the energy of the slipstream depends on the load of the propeller, defining the load as the ratio between the momentum increase provided by the rotor, and its area. The more the propeller is loaded, the more energy is present in the slipstream. The configuration tested in the present study can by classified between a turbofan and a turbopropeller, in relation to its number of blades and diameter (figure 1.2). This is the reason of the appellation this configuration is commonly referred to: prop-fan.

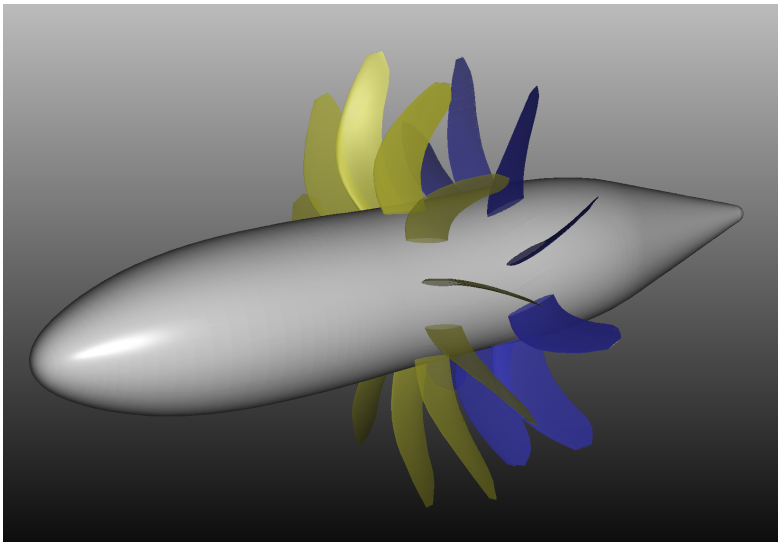

Figure 1.2: The studied prop-fan configuration

Therefore the prop-fan is lightly loaded with respect to a high pressure ratio turbofan but it is highly loaded in relation to turbopropellers designed for lower flight speed [3]. The turbofan has the smallest diameter and imparts the highest swirl velocity to the airstream. The swirl from the turbofan rotor is turned to the axial direction by a downstream row of stator blades. These stators convert tangential velocity to a static pressure rise which appears as an increase in propulsive thrust and efficiency. The lightly loaded propellers of a turboprop do not impart a high swirl velocity and as a result do not have a significant amount of energy in the slipstream. Prop-fan diameters are about 50 percent smaller than the conventional propellers. Swirl velocities for the prop-fans are higher and the full recovery of the swirl energy by employing counter rotation can significantly improve the design point cruise efficiency [3].

1.3 Framework for the numerical approach: trust in CFD

One of the useful applications of CFD is the possibility of using numerical results to analyze the performances of several configurations. This is typical of conceptual design phase, during which windtunnel experiments are very expensive. Therefore the need to evaluate the degree of similarity between results and reality rises immediately.

The first attempts to answer these questions were made in the cases where an experimental validation is not possible, like nuclear energy phenomena or missile tests. Therefore since the end of 1970s some official organizations (most of all in US), like the *Society for Computer Simulations*, performed efforts to improve simulation quality and evaluate errors. In 1980s the *Defense Modeling and Simulation Organization* of the United States Department of Defense began to look for a normalization about this subject: the terms *validation* and *verification* are introduced.

Thanks to these works a CFD simulation can now be considered as composed by three elements [4]:

1. **Reality:** the phenomena that need to be simulated.

2. **Mathematical model:** the equations that describe the reality with a degree of approximation and limited by some assumptions. In Fluid Mechanics this is performed by the Navier-Stokes equation system, which is based on the assumption that the fluid, at the scale of interest, is a continuum. To be applied, the model needs some boundary and initial conditions as well as a turbulence model if the considered variables are averaged quantities, like in the case of the *Reynolds Averaged Navier Stokes* (RANS) equations, as will be described in chapter 4. In particular the boundary conditions setting may become quite complicated when numerous domains are present in the calculation field. In fact in these cases some specific methods are necessary to transfer information from a block boundary to the near ones, which may involved a time dependence if the domains are in relative motion between each other.

3. **Numerical Solution:** the results obtained by the equations, most of the time through a numerical method. This allows the use of the model in a discrete domain in order to perform the simulation using a computer.

These elements constitute some steps which can make the solution quite far from the reality. Therefore a thorough knowledge of the processes that connect each element with the others is

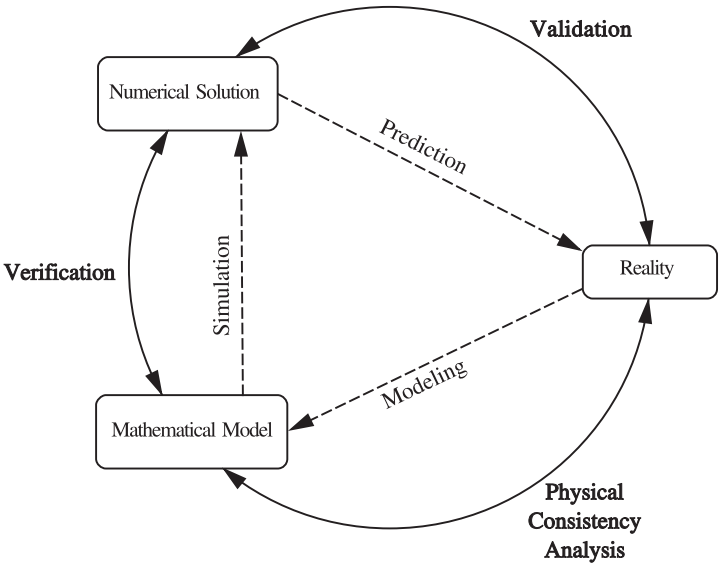

Figure 1.3: The main steps of a CFD simulation

necessary to be aware of the limitations the solution can be trusted with. Moreover the quality of both the Mathematical Model and the Numerical Solution has to be checked by some specific methods.

1. **Modeling and Physical Consistency Analysis:** description of physical phenomena by equations. It is the first step to perform a simulation. This process begins with a thorough observation of the nature and the "fitting" of the reality in mathematical rational schemes. For this last purpose conservation laws are very effective instruments providing methods based on natural fundamental relations. A typical issue in turbomachinery is the interactions among different speed rotating parts. Thence some specific methods to transfer information from a moving domain to another are needed. Moreover the assumptions established about the simulated phenomena allow to set the limits of applicability of the mathematical model and to evaluate the result information content. The two methods that have been used for the present work are treated in the chapter 2 and a comparison between their results is presented in chapter 5. Besides a brief description of the equations solved to simulate the flow is presented in the chapter 4.

2. **Simulation and Verification:** solution of equations in the numerical reality of the computers. This means, first of all, the transition from a continuum nature to a world where only discrete variations are admitted. To perform this passage a discretization of the geometry and the computational domain is required as well as some space and time integration methods. Therefore many sources of error could be involved in the simulation, among which the most important are:

   - iteration process error
   - space discretization error
   - time discretization error

   The purpose of the *Verification* process is just the evaluation of these errors, which means to check if the equations of the mathematical model have been solved properly.

To monitor the evolution of the results during the iteration process, the residuals are calculated at each iteration and some criteria are used to evaluate the convergence of the solution. In particular a calculation is considered converged if the residual values have lost at least 2.5 order of magnitude, comparing to the first iteration value, and a stabilized trend is established.

The space and time convergence methods that have been applied in the present study are briefly described in the following:

- Space discretization
  Based on the exact problem, formulated as a system of conservation laws in integral form, the space discretization has been performed by using the method of the *Finite Volumes*. Therefore the unknowns are averaged values assigned to the center of the discretization cells. Thus a Riemann problem is established at every interfaces between two cells. To calculate the flux through the interfaces two methods have been used and compared: the *Jameson Scheme* and the *Roe Scheme*. The first is a second order centered scheme, which needs a term of artificial viscosity to be stabilized, whereas the second is an upwind scheme that can reach the second or the third order depending on the associated limiter. These techniques are treated in chapter 4, while a comparison and their consequences on the simulation results are presented in chapter 5. The calculation field is defined by a three-dimensional multi-domain block-structured grid, realized using Autogrid.[1] The most important characteristics of the obtained domain are described in chapter 3 and their effects are shown on some result comparisons in chapter 5.
- Time discretization
  Used to model unsteady phenomena, the tested time integration methods are the *Backward Euler Scheme*, the *Gear Scheme* and the *Dual Time Stepping*. The first one is an explicit method, precise to first order in time, which is particularly adapted to high frequency phenomena, not allowing the use of large time steps but involving a relatively low cost in calculation time. To increase the precision of the time dependence the more expensive second order implicit Gear Scheme and Dual Time Stepping have also been tested.

After the choice of the numerical scheme and the time integration method some parameters need to be set to perform an efficient calculation. In particular the effects of the time step and the mesh size have been analyzed using the Richardson method, to relate the result quality to the calculation cost. That is the possibility to find the convergence conditions in terms of maximum time step and minimum number of cells.

3. **Prediction and Validation:** comparison of the calculation results with the reality and extrapolation to new configurations. The objective of a fluid dynamics simulation is, most of the times, the prediction of the flow generated by a specific geometry. Nevertheless a process of *validation* is necessary to evaluate the accuracy of the simulated flow, that actually is to check that the mathematical model previously chosen was well adapted to the studied flow. During this phase the similarity between results and reality is estimated

[1] Autogrid is a semi-automatic software particularly dedicated to the mesh generation for turbomachinery simulations.

using an available trusted solution. Obviously the geometry used for the validation must be similar to those that are the final object of the study, thence it is usually not possible to dispose of an analytical solution. That is why to validate a numerical model some windtunnel experiments have to be conducted. Unfortunately the present work do not dispose of such a term of comparison, therefore the validation process is simply based on a qualitative description of the physical phenomena that occur in the simulated flow. For this purpose the results of each methods used in the present work are presented in chapter 6.

1.4 Objectives

In this framework, the present study focus on the verification phase. Nonetheless the processes of modeling and validation are briefly described to give an idea of the final results information content and of its limitations. In other words this project aims at assessing numerical methods, already in use for turbomachine simulations, applied to a generic CROR configuration. Therefore the reader should keep in mind that the working characteristics of the treated geometry are not the object of the study and should not be directly compared with existing engine performances. As mentioned above, since acoustics and airframe integration are important concerns for open rotors, the emphasis is put on unsteady time integration methods. In particular two methods have been tested. Both allow to limit the calculation domain to a single channel. This means that only one blade for each rotor is present in the numerical field, and some specific periodic conditions are used to take into account the presence of the other blades.

Mixing Plane Method: a technique to take into account the effects of each rotor on the other in a conservative steady manner. At each side of the interface plane between the two rotors all the physical variables are averaged over the azimuthal direction to obtain some radius dependent functions. These are then transmitted unchanged to the opposite side of the plane. The lateral faces of the channel are simply treated as space periodic boundaries, according to the axial symmetry of the geometry. This method allows, with a relatively low computational cost, to get the mean overall flow features, but it lacks provision for the interactions between the two rotors. It can also provide a good initial solution for the unsteady method.

Chorochronic Method: an unsteady technique to model rotor-rotor interactions. The transmission of information from a rotor to the other, and from one side of the channel to the opposite, is based on a time and space periodicity. In this way both the viscous and potential effects of each row are correctly transmitted to the other. This physical accuracy involves a quite high cost in term of calculation time. In fact, to reach an established periodic state more than a rotor revolution are needed.

Quantifying the relative accuracy and computational efficiency of these methods is a central point of the present work. This will hopefully give some help to next studies focused on the engine performances rather than the numerical simulation.

1.5 Structure of the report

The philosophy of the entire study is performing the simulations being aware of the consistency and the quality of the obtained results. The structure of this report follows this idea describing the steps that connect the simulation to the physics of the phenomena.

Therefore the first step is the discussion of some techniques that allow to model rotor-rotor interactions, focusing on their pros and cons, which finally lead the choice of the methods applied in the present work, chapter 2. The field of calculation is then discretized, by using the Autogrid software, whose principal features are described in chapter 3. In the following chapter the Navier Stokes equations are obtained, thus the assumptions and the degree of uncertainty involved by the modeling process are determined. In the same chapter the different methods that have been used to take into account turbulence dynamics and to discretize the equations in time and space, are also presented.

Once the modeling step is accomplished the calculation can be performed, and the results verified. Therefore the last two chapters are dedicated to the analysis of the solutions obtained by using different methods. In particular the chapter 5 is dedicated to the verification of the solving process. Results obtained by different numerical methods are here compared and the error due to the time and space discretization is determined. Moreover this chapter carries out a comparison between the mixing plane and the chorochronic approach, evaluating the consistency of each techniques and bringing to light their limits.

Finally the step of validation has to ensure a high degree of similarity between the simulations and the foreseen reality, thence a reference solution should be used to be compared with the numerical results. Unfortunately, as mentioned above, there are no experimental data available to accomplish this phase. Nonetheless a kind of validation is performed in the last chapter, where some aspects of the results are explained under qualitative physical considerations.

Chapter 2

Turbomachinery simulation approach: state of the art

Contents

2.1 Introduction

The relative motion between successive blade rows in presence of boundary layers, wakes, shocks and tip leakages are the major sources of unsteadiness that may affect turbomachinery flows. All these interactions are strongly coupled, increasing in magnitude as the gap between the blade rows is decreased, and affecting consequently the performance of the machine.

A distinction has to be made between *potential* and *wake* interactions phenomena.

Potential interactions result from the relative motion of blade rows, and propagate in both upstream and downstream directions of the flow. The potential field generated by a rotor is felt as an unsteady disturbance by the front row and by the non rotating annulus. One major consequence of potential interactions is the generation of fluctuating forces on the blades. The prediction of these unsteady forces constitutes essential data for aeroelastic design.

Wake interactions are due to the presence of viscous boundary layers, wakes and secondary flows, which propagate through the downstream airfoils. As wakes and boundary layers leaving a row meet another row, they are transported towards the pressure side of the passage affecting significantly the redistribution of the stagnation pressure and enthalpy

across the blade row. The impingement of the wakes affects also the laminar-turbulent transition. In addition, the wakes leaving a rotor in a boundary layer have higher swirl component of velocity than the mainstream air, making the wake propagation generally three-dimensional.

The first level of approximation is based on the assumption of steady relative flows, neglecting hereby all unsteady components. The second step, allowing a higher level of accuracy, consists in considering the time evolution of the flow, in order to take into account some kinds of unsteadiness. The first section of this chapter will briefly present the shape of a typical turbomachine numerical domain and its components. This will introduce the following sections where some simulation techniques are described.

2.2 The numerical domain

Both in steady and unsteady calculations the purpose of the simulation technique is to manage the presence of different domains in relative motion to each other. Except for the 360° approach (see section 2.6), this problem is faced to by exploiting the time periodicity of the row interaction phenomena and the geometrical axial symmetry of the turbomachine. In fact these characteristics allow to limit the dimensions of the numerical domain by imposing some particular conditions at its boundaries. As shown in figure 2.1 there are two kinds of boundaries, that present different problems:

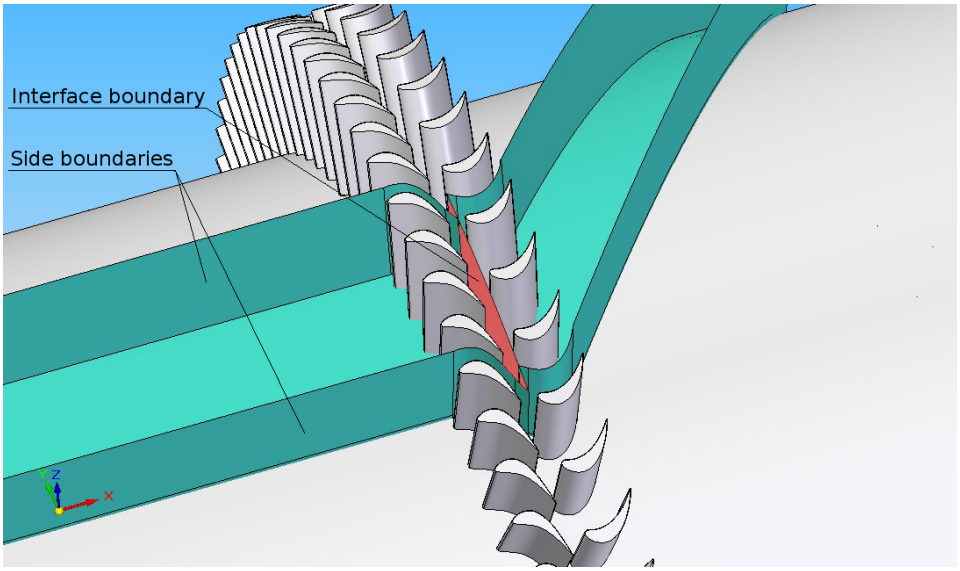

Figure 2.1: Example of a typical turbomachine numerical domain

Channel side boundaries . They are the borders between the blades included in the numerical domain and the other blades of the same row. Therefore the condition applied to this surfaces has to take into account the presence of the row portion that is not included in the domain.

Interface boundary . It forms the surface between two sub-domains that belong to different

rows. This boundary must transmit the interaction effects between the two rows and consider their relative motion.

2.3 Mixing plane method

If, in the rows interface region, flow variations in the pitch-wise direction are neglected, one can assume that the relative flow field across successive rotors and stators is steady. This technique is referred to as *Mixing Plane Approach*, and has been widely used since the publication of Denton & Singh [25]; see also Arts [26]. This approach not only neglects the unsteady effects of rows interactions, but also introduces an error generated by the artificial mixing process applied at the interface. On the other hand the advantages of this technique are the low calculation time, allowed by a steady simulation, and the reduction of the numerical domain to a single channel (only one blade for each row is included in the domain).

Periodic side boundaries

The azimuthal reduction of the domain dimension is realized by imposing periodic conditions between the upper and lower side boundaries of the domain, which can include only a portion of the blade rows. This means that the flow calculated in the grid cells near one side boundary is use to fulfill the ghost cells of the opposite side, as shown in figure 2.2.

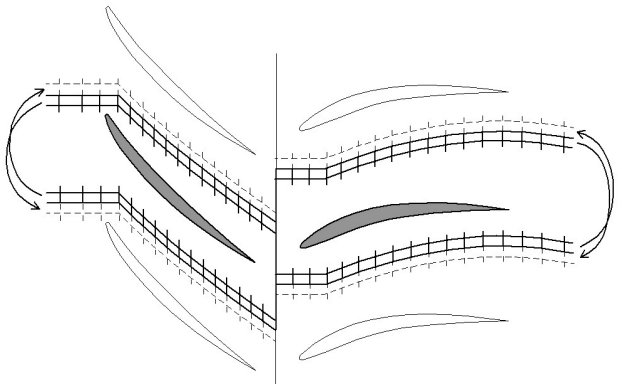

Figure 2.2: Principle of periodical side boundaries

Mixing plane interface

Mixing plane simulations can be seen as coupled steady calculations performed on the successive rows, exchanging boundary conditions at the interfaces [28]. One side of the interface can be seen as an inlet, the physical boundary condition being provided by the average of the flow on the other side. The opposite side is treated as an outlet, with the exit boundary condition being in the same way provided by the flow on the first side. The quite particular character of this boundary condition is that it usually adapts itself to the sense of propagation of the flow, which can be different from one span-wise position to the other. Under this approach, all variables are circumferentially averaged and mixed-out at the rows interfaces, whereby all unsteady components of the rows interaction are lost.

The main problem is to ensure conservation at the interface, which cannot be obtained for all averaged quantities, since it is not possible to satisfy all the averaged conservation laws and conserve the averaged entropy at the same time. Hence error sources from numerical mixing are introduced, generating entropy jumps if conservative variables are averaged, which is some sort of numerical counterpart of the mixing loss that would occur if the flow was actually mixed between the two rows [18]. Different choices for the averaged variables lead to different error sources. For instance mass, energy and two momentum averaged conservation, plus entropy can be imposed. Another alternative consists in imposing a strict conservation of the pitch-averaged mass flow, swirl, total temperature and total pressure. This is not a trivial issue on the theoretical side, as no option appears to be absolutely superior to the others. In the present work the quantities that are imposed to be conserved are the Riemann invariants.

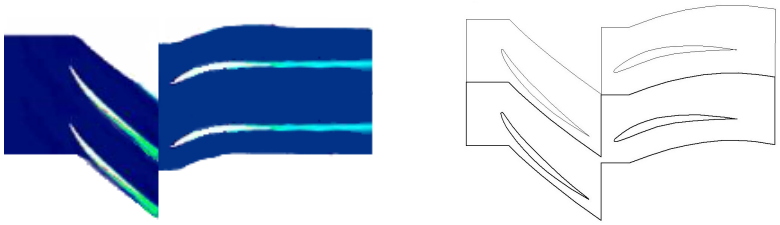

(a) (b)

Figure 2.3: Example of a flow field obtained by a mixing plane approach (entropy contours). The domain is duplicate once by geometric periodicity.

2.4 Unsteady simulations with periodic side boundaries

An unsteady calculation is fundamental to capture the unsteadiness of the interaction between different rows. In this kind of simulation boundary conditions take a key role by introducing in each domain associated to a blade row the effects of the other rows. This has to be made with time dependent boundary conditions. In this section the case where an axial symmetry common to all the rows can be established, is considered. In figure 2.4 on the facing page an example of this kind of configuration is represented.

This characteristic allows to impose a condition of spatial periodicity between the two opposite sides of the domain (see section 2.3). In fact in the case of an unsteady simulation, where the row interactions are captured, also the dynamics of the flow must have an axial symmetry that match with the lateral dimension of the domain. This involves a common periodicity for all the rows and limits the simulated phenomena to the dynamics due to the passage of a row blades in front of the considered portion of another row.

2.4.1 Side boundary conditions

Periodic conditions at the side boundaries can be applied in two cases:

- an azimuthal periodicity common to all the rows occurs, which may include several channels of the real geometry;
- a limited modification of the given geometry can be afforded, in order to restore periodicity.

In the following the two approaches are briefly described.

Multi-channel simulation with periodic boundaries

In the particular case where the different number of blades of the considered rows have a common divisor factor m, the numerical domain can be reduced to $360°/m$. In fact a simple axial periodic condition can be applied to the two sides of the considered row portion, by using the flow calculated near the limit of the domain as boundary condition at the opposite side.

With this approach only the deterministic interactions can be captured, in fact the condition of spatial periodicity is required for the simulated phenomena as well. This means that, for instance, rotating stall or upstream localized disturbances cannot be simulated.

The most important drawback of this method is the requirement on the geometry of the machine. In fact the factor m directly determine the size of the numerical domain. For instance in the case of the open rotor configuration treated in the present study the multi-channel periodic boundaries technique would involve no advantages with respect to a 360° approach (described at the end of this chapter).

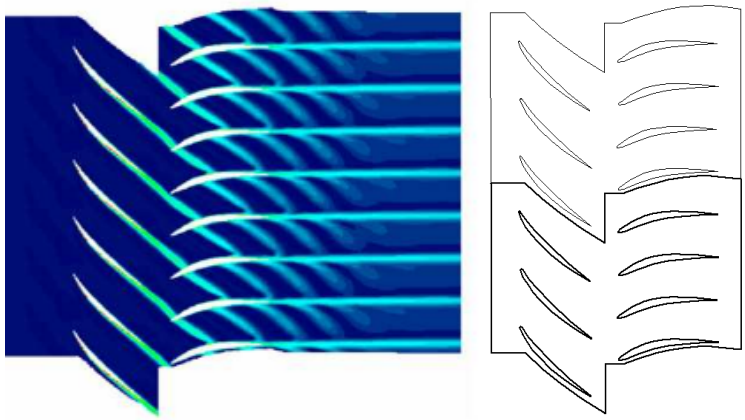

(a) **(b)**

Figure 2.4: Multi-channel simulation 4:3, performed by N. Gourdain (entropy contours). The domain is duplicate once by geometric periodicity.

Blade number reduction with periodic boundaries

This technique, proposed by Arnone and Pacciani [34], allows to apply an unsteady approach to a portion of a modified geometry when no common divisor factor exists among the blades number of the considered rows. The idea is to use a different number of blades in order to find a common divisor factor and then be able to apply the periodic boundary conditions discussed above. For instance, Bardoux [35] applied this technique to the turbine VEGA2 changing the number of blades of the row to pass from a configuration 23:37 to a configuration 23:46, obtaining two row blades for each nozzle guide vane, as shown in figure 2.5 on the next page. Actually one can notice that performing the simulation on a configuration 24:36, that means two row blades in front of 3 nozzle guides vanes, would provide a geometry more similar to the real one.

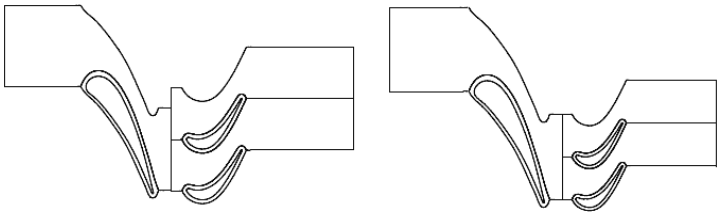

Figure 2.5: Blade number reduction performed by Bardoux analyzing the turbine VEGA2. Modification from a 23:37 to a 23:46 geometry, obtaining azimuthal periodic boundaries at the sides of a 360/23° sector

The obvious drawback of this approach is the modification of the original geometry. This involves differences both in the flow and in the working point characteristics, as the choking condition. In some cases, in order to get the solution closer to the reality, the chord of the blade profiles can be modified, keeping constant the chord-pitch ratio. Nonetheless the frequency and amplitude of the unsteady fluctuations are different from those of the real geometry.

2.4.2 Interface boundary conditions

The interaction plane between two rows needs to transmit information between two domains in relative motion to each other. This is treated by a *sliding mesh* approach.

Sliding mesh approach

The sliding mesh model allows adjacent grids to slide relative to one another. In doing so, the faces of the the grid cells do not need to be aligned on the grid interface. This situation requires a means of computing the flux across a non-conformal interface boundary. This is performed by determining the intersection between the grid interfaces at each new time step. The resulting intersection produces one interior zone (a zone with fluid cells on both sides) and one or more periodic zones. The resultant interior zone corresponds to where the two interface surfaces overlap; the resultant periodic zone corresponds to where they do not.

The number of cell faces in these intersection zones will vary as the grid interfaces move relative to one another. Subsequently, fluxes across the grid interface are computed using the portion of cell faces resulting from the intersection of the two interfaces. In the example shown in figure 2.6 on the facing page, the grid interfaces are composed of cell faces A-B and B-C for grid #1, and call faces D-E and E-F for grid #2. The intersection of these interfaces produces the faces d-a, a-e, e-b, etc. Faces produced in the region where the two cell zones overlap (a-e, e-b, and b-f) are grouped to form an interior zone, while the remaining faces (d-a and f-c) are paired up to form a periodic zone. To compute the flux across the interface into cell IV, for example, face E-F is ignored and faces e-b and b-f are used instead, bringing information into cell IV from cells I and II, respectively. In a similar way, the periodic zone is realized by considering the faces d-a and f-c as the same face, connecting cells II and III.

2.5 Chorochronic method

The chorochronic method, also called phase-lag or phase-shift, is based on a spatio-temporal periodicity between the side boundaries, which allows to limit the calculation field to a single channel still being able to capture the deterministic unsteadiness of the flow. This means

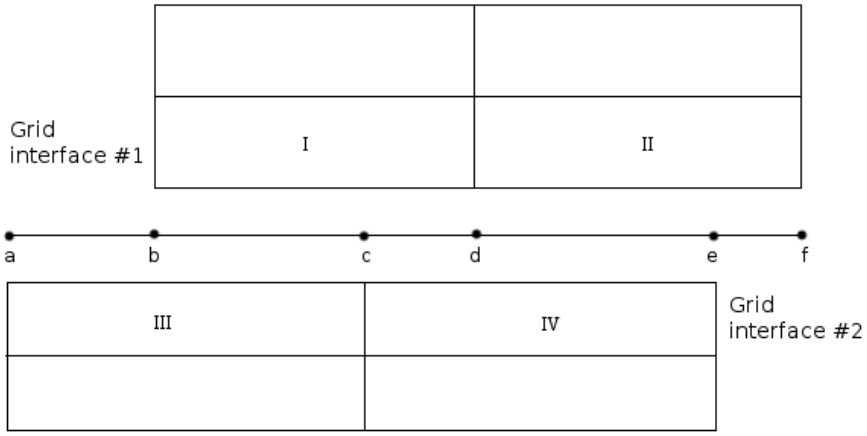

Figure 2.6: Two-dimensional grid interface, treated with sliding mesh technique

treating only one blades per row, extending the discretized volume in the pitch-wise direction just to reach an axial periodicity of the numerical domain. Such a characteristic is fundamental for an open rotor simulation because of the very high number of grid cells required by the external field mesh. The fundamental assumption this simplification is based on, is that all the simulated time-dependent phenomena are due to deterministic causes:

- passage of a row blades in front of the considered channel of another row, which generates both potential and wake effects;
- phase displacement between the blades of the same row to analyze flutter dynamics;
- turning wave at the inlet of the row.

Therefore the chorochronic methods does not allow to take into account phenomena not directly dependent from the turning speed of the machine as, for instance, the vortex emissions at the blades trailing edge or the rotating stall. On the other hand, the required assumption means that a relation exists between the flow time evolution and the motion of the considered blades. This relation can be specified by a mathematical expression that connects the flow around a blade in a certain time instant, to that around the next blade of the same row in another time instant, as explained in the following.

In the present report only the single-frequency approach is described, considering that the studied configuration is composed by just one stage, but being aware that more complicated approaches are needed if the effects of several stages have to be considered.

2.5.1 Side boundary treatment: spatio-temporal phase displacement

In the following pictures the two blades that are included in the numerical domain are gray colored, and the bold lines define the field boundaries. The rows represent a typical turbine configuration, where the front row is a stator (thence actually $\Omega_1 = 0$) and the following a rotor. The streamlines represent different time instant flows, and they are referred to the local coordinate system (moving with the blades).

Taking into consideration the channel side boundaries, the *phase-shift* δt is the time after which the flow calculated at a boundary cell can be used as boundary condition for the

corresponding cell at the opposite side of the channel:

$$\phi(x, r, \theta, t) = \phi\left(x, r, \theta + \frac{2\pi}{Z}, t + \delta t\right) \tag{2.1}$$

where ϕ is a physical quantity of the solution and Z the number of blades of the considered row. According to figure 2.7, this is performed by filling the ghost cells of a boundary, represented with dotted lines, with the solution calculated near the opposite side, as shown by the arrows. In order to apply this process, the chorochronic period is defined as the necessary time step δt for the flow around a blade to occur around the next or the previous blade of the same row. This depends on the rotation direction of the considered rotor and the relative number of blades between the two rows, as explained in the following paragraph.

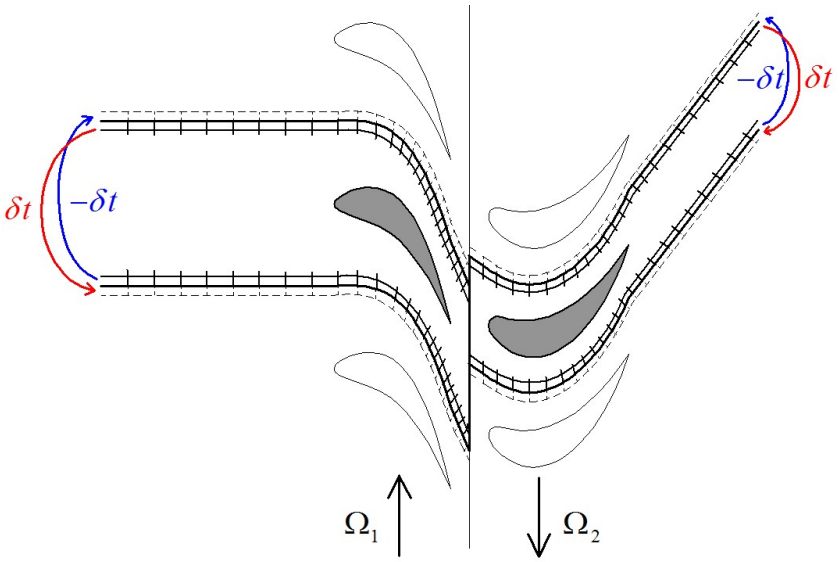

Figure 2.7: Example configuration with the numerical domain δt

The entity of this time step depends on the physical unsteady phenomena that have to be considered. In the present study the considered interactions between the two rotors are only time-dependent effects, which means no turning waves or phase displacement between the blades of the same row. In this case the time step δt is called *chorochronic period*, and is treated in detail in the next paragraph.

Chorochronic period

The purpose of this paragraph is to obtain the expression of the spatio-temporal phase displacement in the case of interaction between two rows. More detailed discussions can be found in the Neubauer's thesis [33] for a heuristic explanation, or in the article of Wang and Chen [32] for a more mathematical derivation.

Referring to figure 2.8 on the facing page, at the time instant t_0 the leading edge of the considered rotor blade is in front of the trailing edge of the stator blade. This relative position defines the flow represented by continuous lines, which is the solution at the time t_0. As one can see the same relative position occurs at the time instants $t_0 - \delta t$ and $t_0 + \delta t$ in the channels adjacent to the discretized one. Therefore, in these cases the solution obtained at t_0 can be

applied as boundary condition, in order to determine the flows at different times, represented by dotted lines in parts (a) and (c) of the figure. Conversely the calculation of the t_0 solution needs the boundary condition obtained by the $t_0 + \delta t$ flow, for the upper side of the channel, and by the $t_0 - \delta t$ flow, for the bottom side.

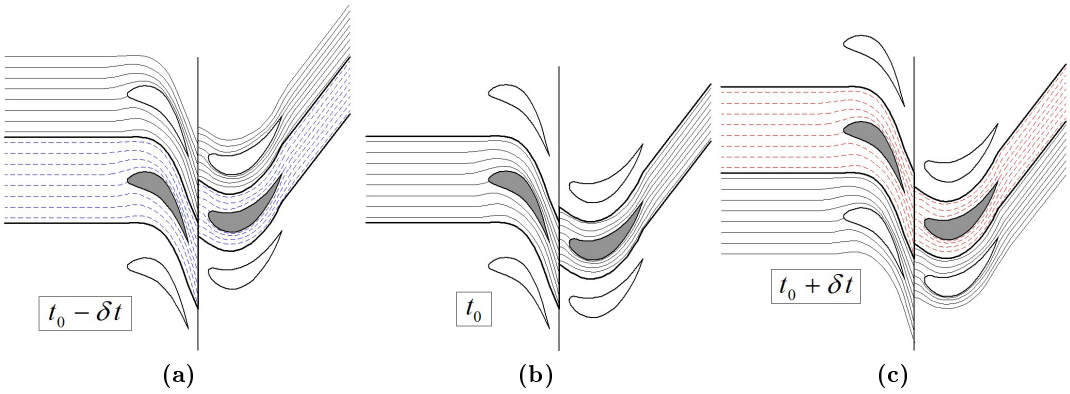

Figure 2.8: Physical description of the chorochronic period δt

The need to know the flow at the time $t_0 + \delta t$ for the calculation of the t_0 solution is the cause of the long time of convergence that typically affects chorochronic calculations. In fact the updating of the boundary condition depends on the quality of the solution that, obviously, is affected by the boundary conditions. In practice the future instant condition is taken by the previous period (so that the $t_0 - T + \delta t$ flow is used instead of the $t_0 + \delta t$ one, where T is the blade passing period). This means that for the simulation of a certain time instant, the flow obtained some hundreds of iterations before is used. It is worth to remark that the convergence speed is lower than that of a calculation performed with periodic boundaries. The experience has shown that a factor of about 3 exists between the lengths of time required to reach the convergence state by the chorochronic method and the multichannel periodic boundaries technique.

As one can see, the chorochronic period corresponds to a relative rotation equal to the difference between the pitches of the two rows. Thence it can be expressed in the form:

$$\delta t = \left| \frac{\frac{2\pi}{Z_1} - \frac{2\pi}{Z_2}}{\Omega_1 - \Omega_2} \right| \tag{2.2}$$

with

$$Z_1 = \text{number of blades of the upstream row} \tag{2.3}$$

$$Z_2 = \text{number of blades of the downstream row} \tag{2.4}$$

The monitoring of the variation of the boundary conditions during the calculation can be an efficient way to control the convergence of the iterative process. In fact the convergence state corresponds to a perfectly periodic trend of these fluctuations. In the present work a similar technique has been applied, as explained in section 5.2.3.

2.5.2 Interface boundary treatment

As mentioned above the main advantage of the chorochronic method is the reduction of the numerical domain to a single channel, without any requirements on the geometry of the machine.

This is allowed by phase-lag conditions on the side boundaries, nevertheless it has a strong effect on the interface boundary too. In fact in this case the calculations on the two sub-domains, which belong to different rows, have different spatial evolutions by following the discretized blades during their rotation around the machine. Therefore one side of the interface is uncovered for the most of time.

This situation requires to associate the sliding mesh technique with a process intended to cover each interface surface with a reconstruction of the opposite side of the interface boundary. As shown in figure 2.9, the reconstruction of one side cover uses the different solutions of the other side taken at different time instants. In the first picture the relative position of the two sub-domains at an initial instant t_0 is shown. After a blade passing period of the front row (T_1), the downstream sub-domain takes the right position to completely cover the upstream interface boundary with the initial t_0 solution[1].

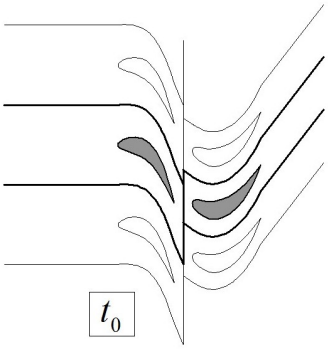

(a) Initial time

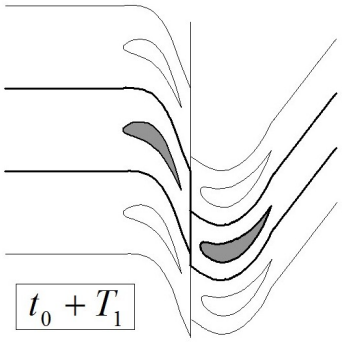

(b) A T_1, after the initial time

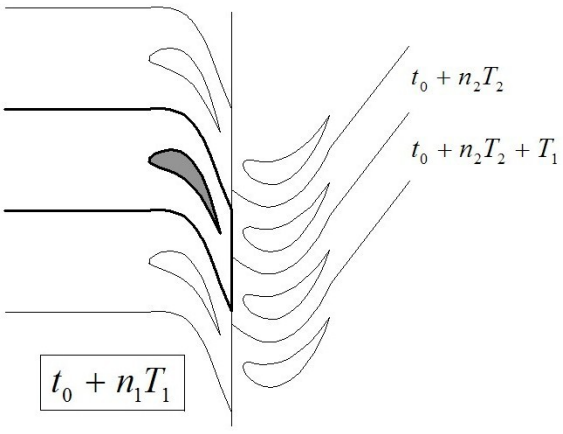

(c) Covering of the upstream interface boundary, $n_1\,T_1$ after the initial time

Figure 2.9: Covering of the interface boundary front side with two instant solutions of the downstream channel

The figure 2.9c shows the position of the upstream sub-domain after n_1 blade passing

[1] The *blade passing period* is the period by which the blade of a row sees the blades of the other row passing. This depends on the relative rotation speed between the rows and on the number of blades of the opposite row: $T_1 = \frac{2\,\pi}{Z_2\,|\Omega_1 - \Omega_2|}$ and $T_2 = \frac{2\,\pi}{Z_1\,|\Omega_1 - \Omega_2|}$.

periods. During the time elapsed from t_0, the rear sub-domain has moved downward, leaving the front side of the interface boundary completely uncovered. Thence, in order to cover it, two solutions of the downstream side, which differ from each other of the time T_1, need to be used. The applied values are taken by the last fields computed in rear domain that correspond to the right instants. The whole factor n_2 represents the number of blade passing periods T_2 elapsed for the downstream domain since the initial time, therefore the most updated solutions of the rear channel that can be used, have been calculated in the instant $t_0+n_2\,T_2$ and $t_0+n_2\,T_2+T_1$.

Actually, the absence of a geometrical interpolation among the cell faces of the two interface boundary sides, allows to simulate the motion of the two sub-domains just by applying the time-dependent condition described above. That is, the two domain portions do not move. This means that vectors and frames of reference are not turned to follow the movements of the blades, reducing the computational cost of each iteration. On the other hand a process of reconstruction is needed to bring in the right position each result extraction and to obtain multi-channel fields, as described in section 6.2.1.

2.5.3 Memory administration

The idea of using a spatio-temporal boundary condition between the two sides of a channel has been proposed by Erodos *et al.* [27].

The Erodos technique works by keeping in memory the solution at boundaries at each iteration. This technique is called *direct store*.

He [29] proposes to implement the phase displacement condition by decomposing the field at the side boundaries using the Fourier series, limited to order N:

$$\phi(x,r,\theta,t) = \sum_{k=-N}^{N} \hat{\phi}_k(x,r,\theta)e^{(ik\omega t)} \tag{2.5}$$

in order to store in memory only the coefficients of the series $\hat{\phi}_k$. This method, called *shape correction*, allows to reduce the memory required by the calculation. The elsA code uses this technique, and the number of the stored harmonics can be fixed by the user.

A third method is proposed by Giles [30, 31]. It is based on a spatio-temporal transformation of the initial equations, which allows to only impose a spatial periodicity at the side boundaries of the channel. The drawback of this method is that each cell of the grid follows a different time evolution, in other words an extraction corresponding to a certain iteration gives cell values that actually refer to different time instants depending on the cell the value belongs to. This makes the post-processing of the results quite complicated. Moreover this technique suffers of numerical stability problems. Therefore it is finally not widely used.

2.6 360° approach

This approach is the reference method. If the condition of a good temporal and spatial discretization is satisfied, all the interactions between the rows are captured. In this case no requirements of spatial or temporal periodicity are needed, neither on the geometry nor on the captured phenomena. In fact the whole machine is considered in the numerical domain. The limits among the various channel meshes are simply connections between adjacent blocks,

and the azimuthal boundary concept loses its relevance. All the interfaces between two rows are treated by using interpolations that ensure the fluxes conservation, as the sliding mesh technique.

The obvious drawback of this approach is the very high cost,

- in terms of memory, due to the need of consider every channel of every row in the numerical field;
- in terms of CPU time, due to the size of the domain but also to the transient state which typically needs from 1 to 5 periods to finish.

In the case of the 360° approach the number of periods which are needed to get a convergence state is lower than the case of chorochronic periodicity. Nonetheless, in this case, one period actually means a complete row revolution, while the unsteadiness period of a chorochronic calculation is simply the blade passing period. Therefore, finally, the convergence times can be similar, if the number of blades of each row is not too high.

Chapter 3

Mesh Generator: Autogrid

Contents

3.1 Introduction

The discretization of the geometry and its surrounding domain is one of the most important steps in the modeling of the reality. The local number and position of points may have some very important effects on the iterating process and simulation results. The space discretization, in fact, has to be performed with awareness about the physical phenomena which could develop in each particular zone of the domain. This kind of estimation may involve a number of grid points higher than what would be necessary, but it is only after a thorough post-processing of the first results, that the point distribution can be better adapted to the solution. Nonetheless high frequency dynamics could not be resolved if the number of points is not sufficient since the beginning. A method to analyze the influence of the grid size on the solution and to find the minimum number of points to obtain an accurate simulation, is applied in the chapter 5. In the present chapter the most important features of the software used for the mesh generation are presented, as well as the characteristics of the obtained grid.

3.2 CROR mesh topology

Autogrid is a semi-automatic software particularly dedicated to the mesh generation for turbomachinery simulations. Some useful features are available to quickly obtain a mesh adapted to the geometry of a rotating machine. In the present study only the structured mesh potentialities of the software have been exploited, because of the elsA limitation about unstructured mesh.

According to the time integration methods that are planned to be used, only a single channel needs to be considered in the numerical domain. The azimuthal dimensions of the channel are fixed by the number of blades of the two rotors. In fact a condition of periodicity, in space

or both time and space according to the method, can be established at the lateral boundaries. This point is thoroughly developed in the chapter 2.

3.2.1 Internal field

The first meshed region has been the internal part of the channel, that is the space around the blades, from the front to the rear farfield, extended to the blade tips, as shown in figure 3.1.

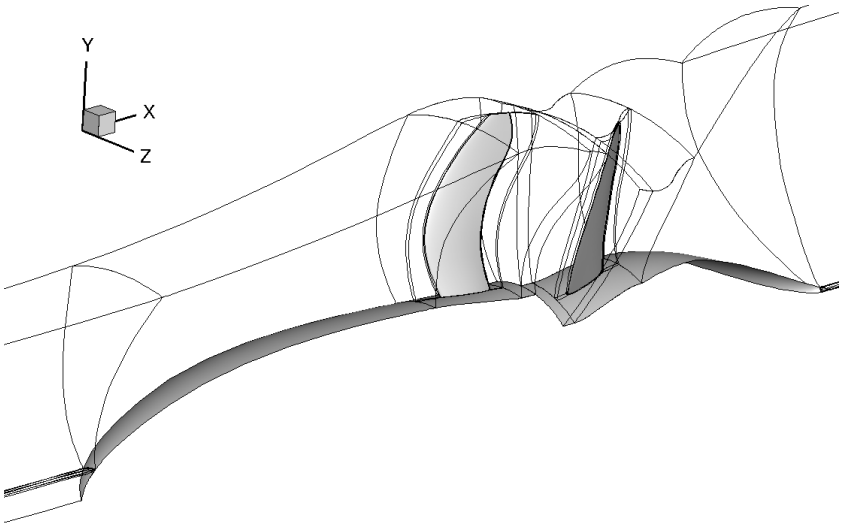

Figure 3.1: Internal channel topology

In particular the longitudinal field size has been fixed to 20 meters, with the propeller system placed in the center of this region. This allows to keep the limits of the numerical domain sufficiently far from the region of interest, considering that the hub is about 8 meters long and the chord of the blades about 0.5 meters.

In this part of the field, the most noteworthy zones are situated upstream and downstream of the spinner tips, around the blade airfoil and near the blade tips. These regions are described in the next sections.

Spinner tips

Two *butterfly* blocks have been used in the regions where very low values of radius occur, in order to keep a regular grid even where the classical quadrilateral scheme would not be effective. The peculiarity of this kind of blocks is, referring to figure 3.2 on the next page, the distribution of the iso-i and iso-j planes, and the form of the k-constant planes. In fact this shape allows to discretize an angular sector, including the region near the center of the circle, still keeping a good mesh quality.

Blade airfoil

The region around the blades has been discretized by a C block, as shown in figure 3.9a on page 26. Next to this one, four H blocks allow a good control of the distribution of points in order to carefully calculate the flow near the stagnation point and the wake leaving the trailing edge. The characteristics of the mesh near the blade walls are detailed in the figure

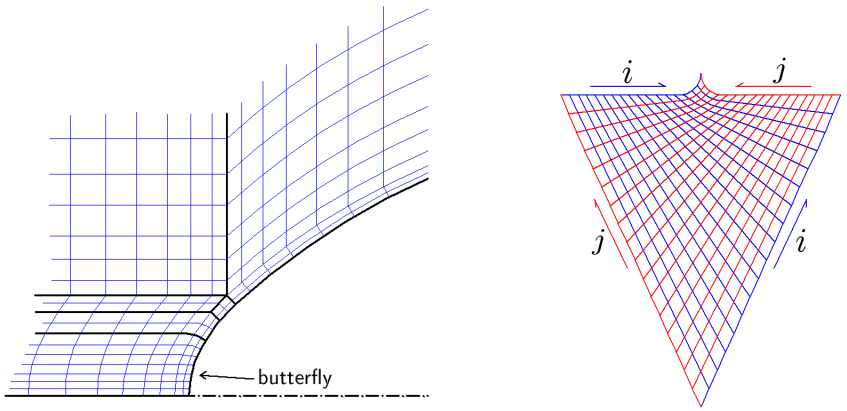

(a) Block topology to treat the upstream and downstream spinner tips

(b) Point distribution in the butterfly block

Figure 3.2: Spinner tip topology and butterfly mesh

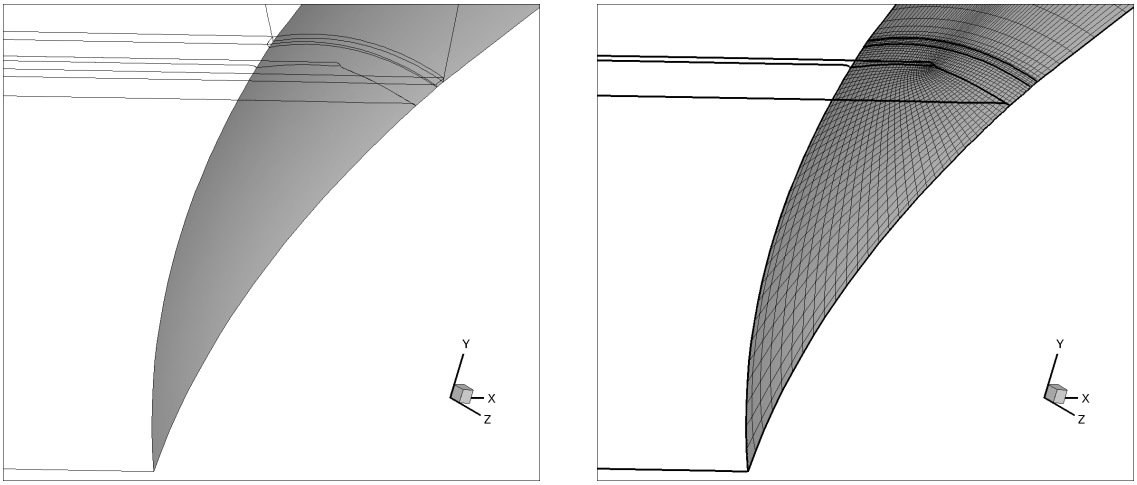

(a) Block topology to treat the spinner tips

(b) Wall mesh obtained by the butterfly block

Figure 3.3: Upstream spinner tip discretized by butterfly blocks

3.5, where the high mesh density used to capture the wake can be noticed. Nonetheless this refinement cannot continue in the H block after the upstream blade, because of the need to have an azimuthal constant points distribution at the interface between the two rotors. In fact, although this characteristic is not strictly required, it allows to perform a better interpolation between the two sides of the plane, needed to transmit the information from a channel portion to the other. On the other hand, in the downstream field of the second rotor the wake mesh effect can be maintained. Moreover, the topology blocks in this region are purposely shaped around the spinner to follow the wake convection (figure 3.1 on the preceding page).

Once the distribution on a radius-constant plane has been defined, the software will keep the same parameters for each span-wise section, adapting the shape of the channel and of the blocks to the corresponding blade airfoil. The following figures show the evolution in the span-wise direction of the mesh around the blades. Each image corresponds to a circumferential grid plan, identified by the j coordinate, oriented in the span-wise direction: $j = 1$ (near the blade root), $j = 25$ (about the center of the blade span) and $j = 50$ (near the blade tip).

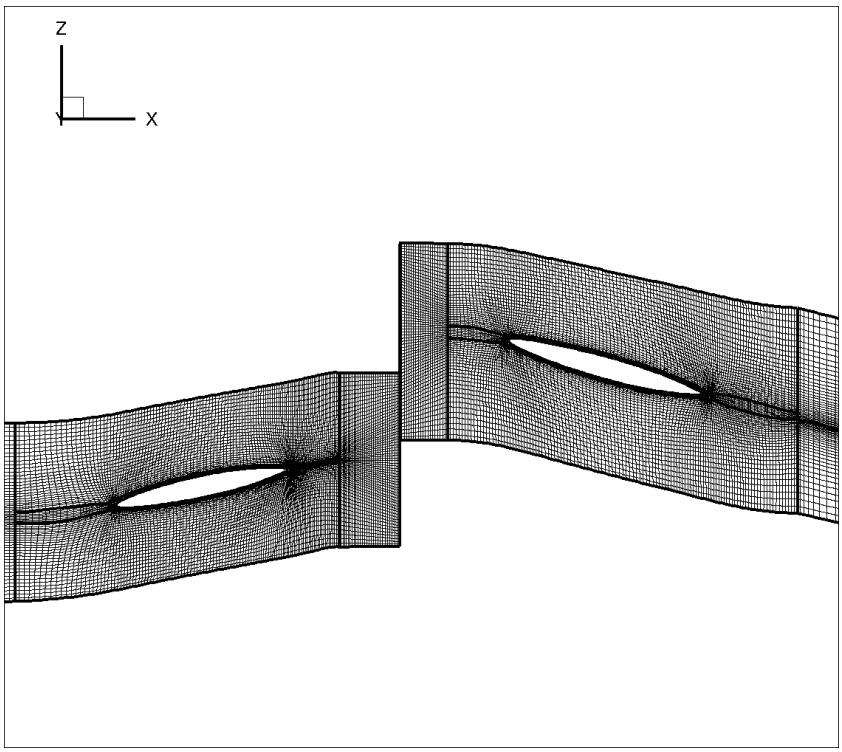

Figure 3.4: j=1, blade root mesh

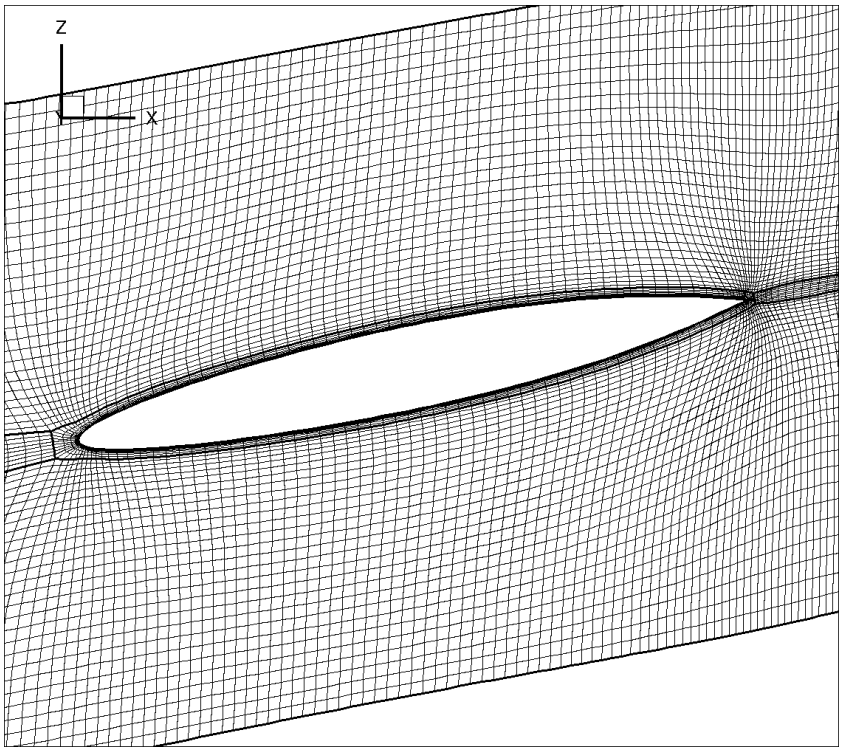

Figure 3.5: Mesh around the upstream rotor root airfoil

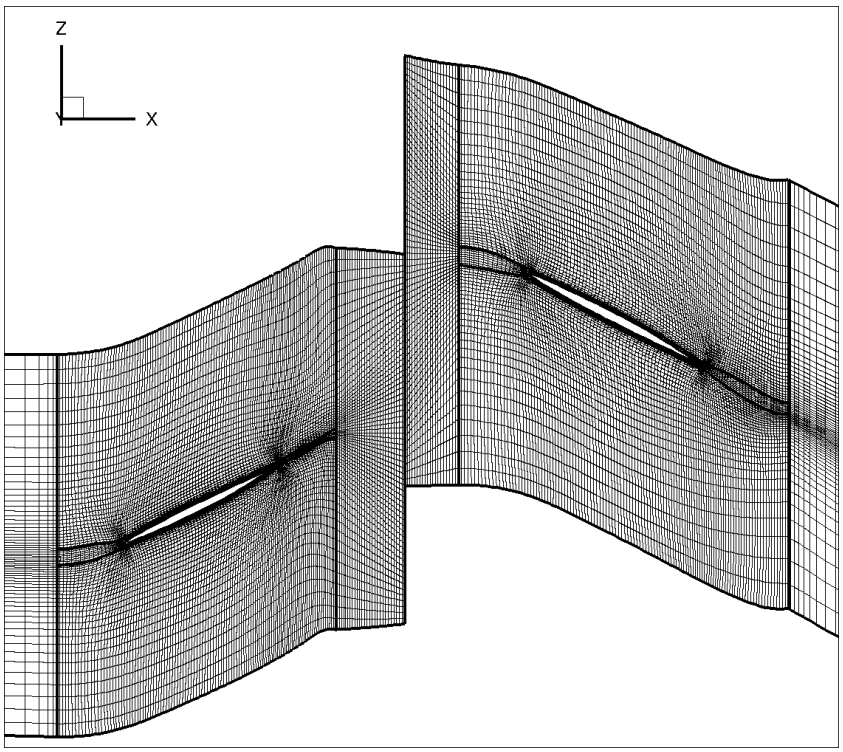

Figure 3.6: j=25, center of the blade span mesh

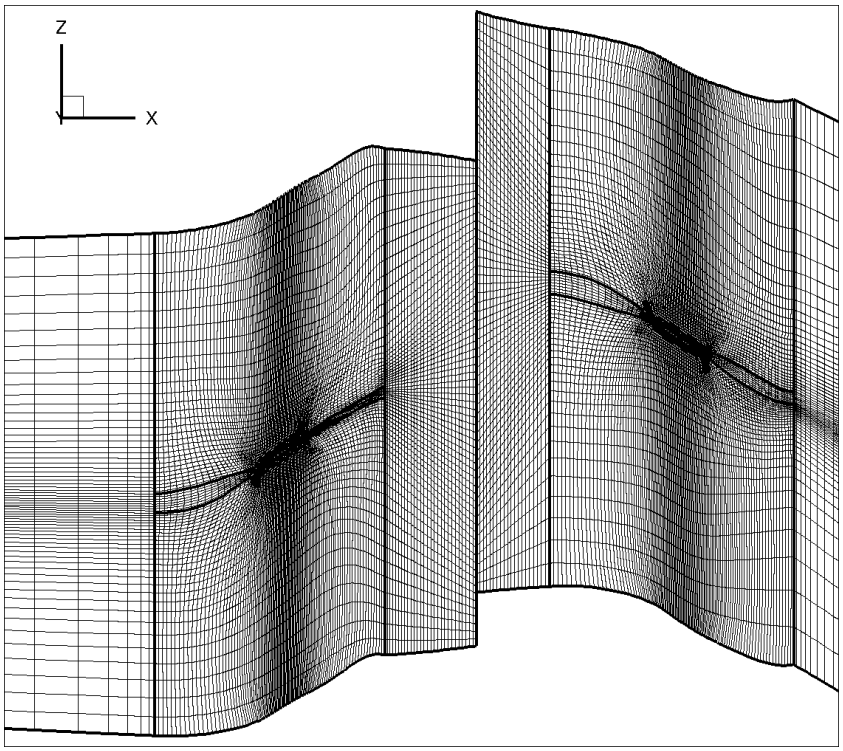

Figure 3.7: j=50, blade tip mesh

Blade tip

The blade tips are regions where high gradients of the physical quantities typically occur, therefore to dispose of a good quality mesh is fundamental. This means to have a high number of points but also some regularly shaped cells. In order to reach this goal, the C and H blocks around the each blade are extended over the blade span, as shown in figure 3.8, and at the place of the blade volume two other mesh blocks are placed. In particular the shape of the tip profile is reproduced using a O and a C blocks.

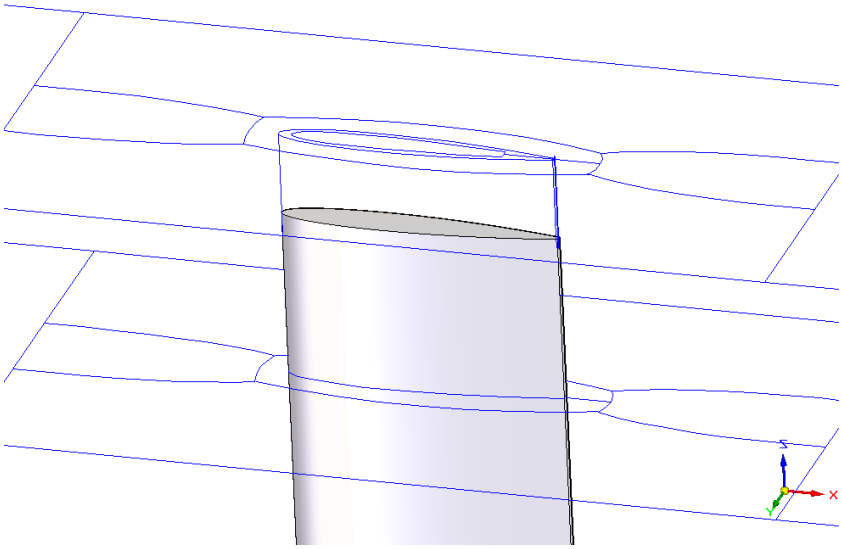

Figure 3.8: Scheme of the blade area topology

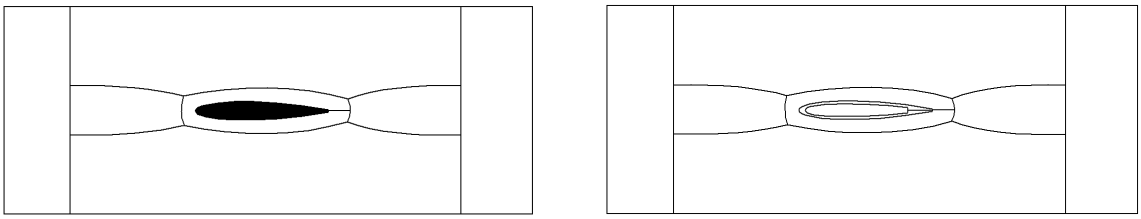

(a) Topology around the blade walls **(b)** Topology over the blade tips

Figure 3.9: Blade topology schemes

The figure 3.10 and 3.11 on the facing page show the grid obtained at the upper end of the internal channel, over the first rotor blade. It is worth to notice that the high level of automation in the generation of the mesh with Autogrid often involves some limitations in the control of the points distribution. This happens, most of all, in zones above the blade tips. In fact, in this areas, the imposed number of cells and the geometrical constraints, coming from the axial periodicity and the internal channel shape, involve a lower quality of the mesh in terms of high expansion ratio and low orthogonality.

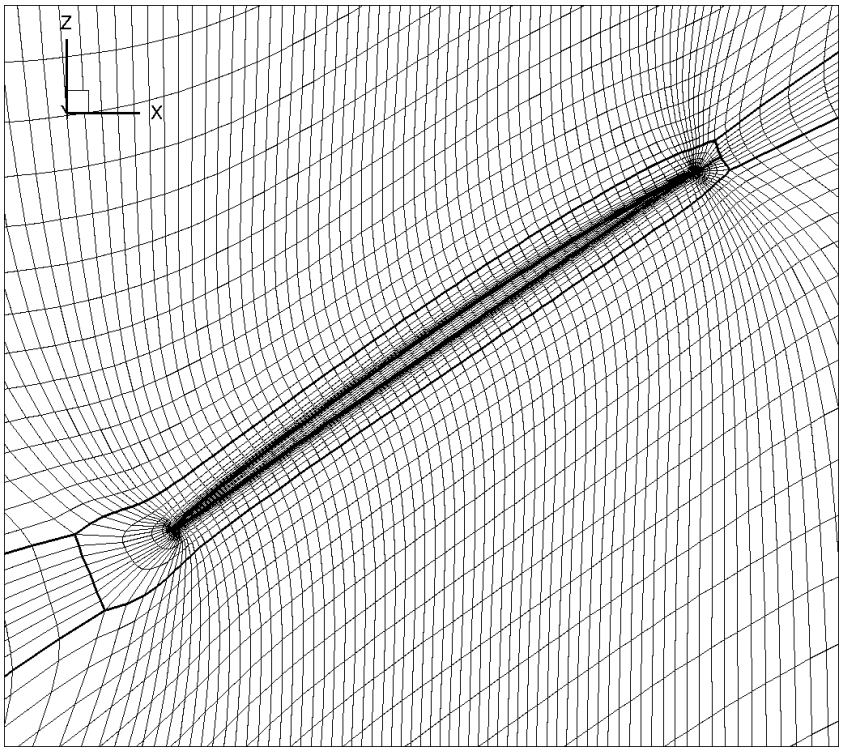

Figure 3.10: Mesh over the upstream rotor blade

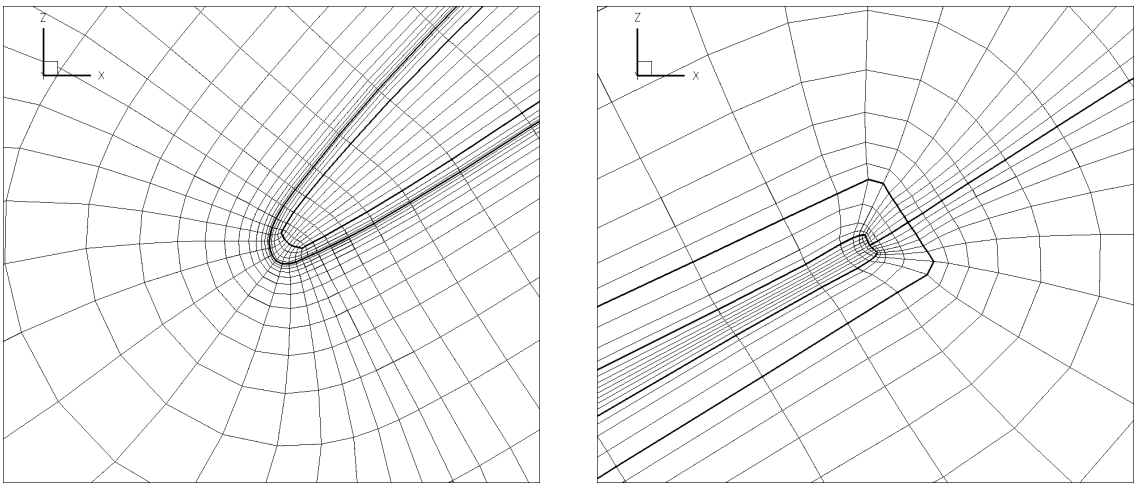

(a) Leading edge **(b)** Trailing edge

Figure 3.11: Mesh detail of the leading and trailing edge over the upstream rotor blade

3.2.2 External Field

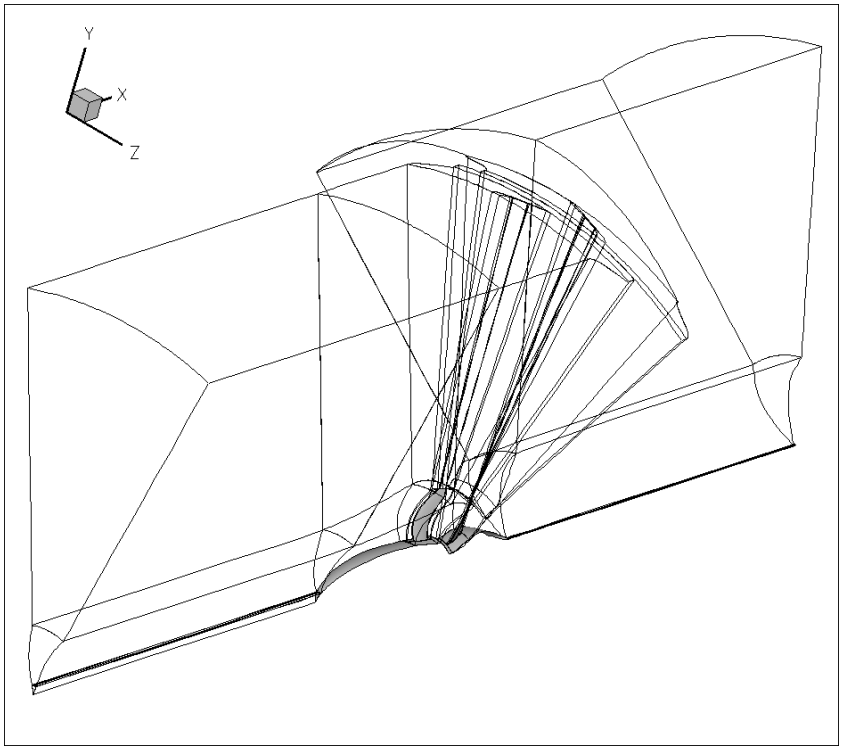

Figure 3.12: The whole numerical domain

The size of the external field has been fixed in order to keep the limits of the numerical domain sufficiently far from the blades zone. That is 10 meters from the rotation axis, with the maximum blade span equal to about 2 meters. In fact one of the purposes of the performed calculations is to evaluate the phenomena generated by the interactions of the two open rotors, which are affected by the absence of the casing. Once the boundaries of the external field are fixed, Autogrid allows to generate the mesh automatically. This tool is quite useful, nonetheless no modification can be made on the azimuthal and axial number of points. This finally means that the internal channel mesh is simply projected on the surface of the outer cylinder. Obviously the high radius of the far field zones works as a shape deformation factor in this process. Moreover the number of points in the radial direction cannot be too low, because of the azimuthal and axial cell density. Besides, the passage through the rotors interface, involves a strong variation of the relative velocity, amplified by the high radius, which may prevent the calculation from reaching a converged state. Therefore a good mesh quality should be kept on the whole interface surface. Nevertheless, in order to maintain an acceptable calculation time, a coarsening factor is applied, involving very high aspect ratios in the radial direction. Finally this may be one of the reasons that prevents the relative velocity formulation from being used, entailing the application of the absolute velocity formulation.

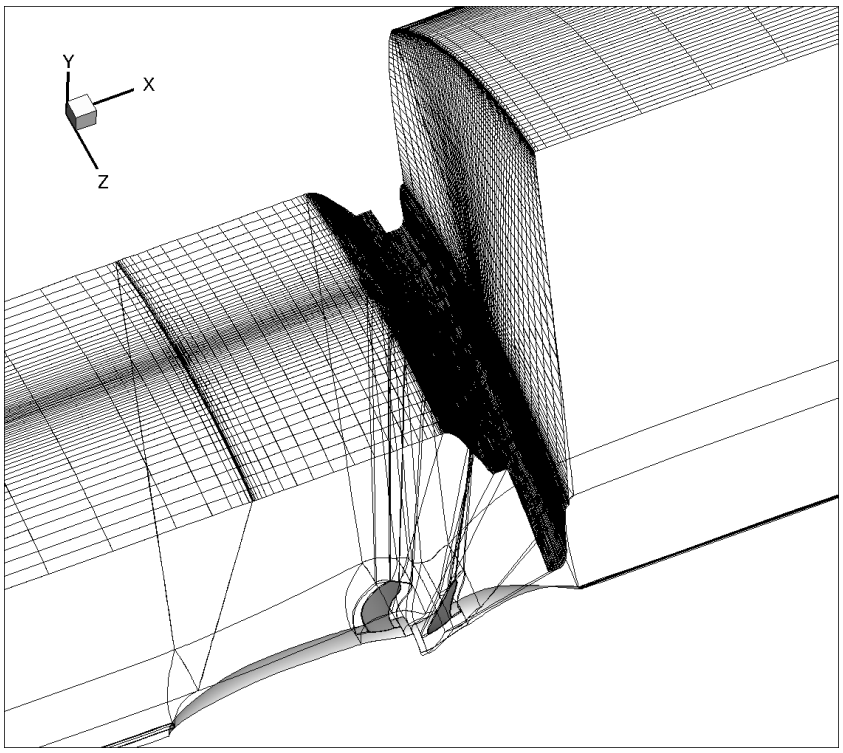

Figure 3.13: External boundary of the numerical field

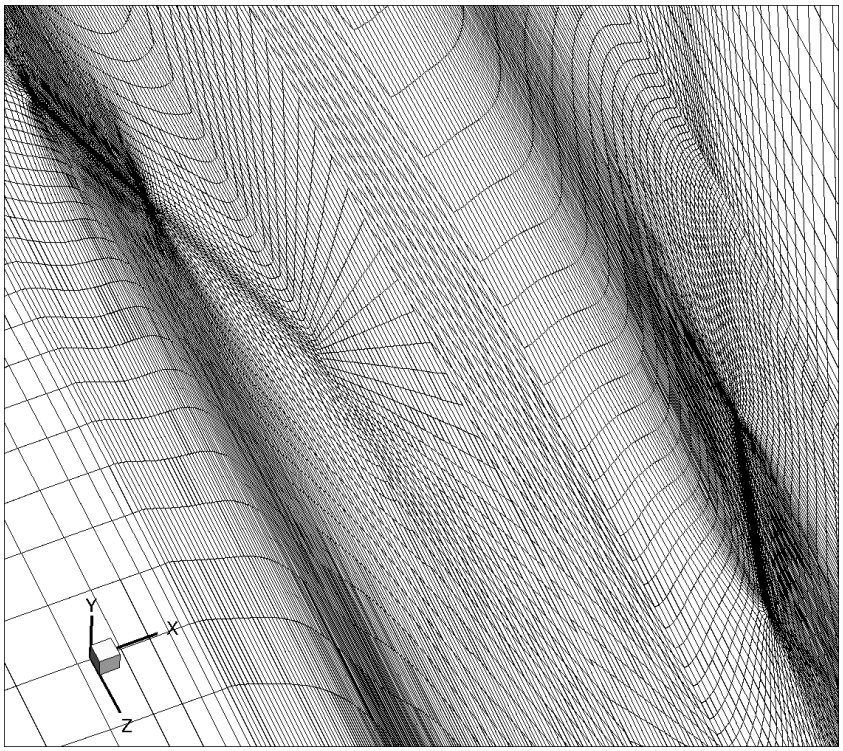

Figure 3.14: Detail of the interface zone on the outer surface

3.3 Mesh quality

The quality of the obtained grid is defined through some geometrical parameters, able to describe the the shape of the cells and their evolution in space:

Aspect ratio It is a measure of the ratio between the two dimensions of a cell on each plane (range 0-50000);

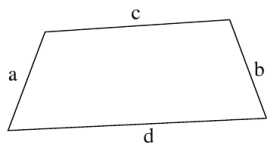

$$x = \frac{a+b}{2} \qquad y = \frac{c+d}{2}$$

$$\textit{Aspect Ratio} = \frac{max(x,y)}{min(x,y)}$$

Expansion ratio It is a measure of the size variation between two adjacent cells, in I, J and K direction (range: 1-100);

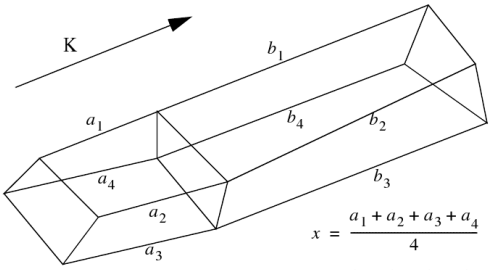

$$x = \frac{a_1+a_2+a_3+a_4}{4}$$

$$y = \frac{b_1+b_2+b_3+b_4}{4}$$

$$\textit{Expansion Ratio (K)} = \frac{max(x,y)}{min(x,y)}$$

Angular deviation It is a measure of the angular variation between two adjacent cells in I, J and K directions (range: 0-180 degrees);

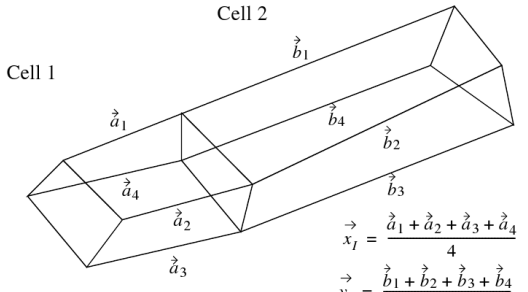

$$\vec{x}_I = \frac{\vec{a}_1+\vec{a}_2+\vec{a}_3+\vec{a}_4}{4}$$

$$\vec{y}_I = \frac{\vec{b}_1+\vec{b}_2+\vec{b}_3+\vec{b}_4}{4}$$

$$\textit{Angular deviation along I-direction} = \angle(\vec{x}_I, \vec{y}_I)$$

Orthogonality It is the minimum angle between the edges of the element (range: 0-90 degrees);

The mesh finally used for the calculations presented in the following of this report has the characteristics described in the table 3.1 on the next page, which refers to the figure 3.15. Subsequently two other meshes have been realized, in order to study the influence of the number of points on the solution and find the grid convergence condition. The Richardson extrapolation, used for this purpose, and its application is described in the chapter 5. In particular the number of points of the two coarse grids is respectively about a half and a quarter of the first mesh size. Actually, the coarsening has been performed keeping three levels of multi-grid which finally prevents the number of points previously fixed from being exactly obtained. The effects of the coarsening on quality of the two smaller meshes is shown in the tables 3.2 and 3.3.

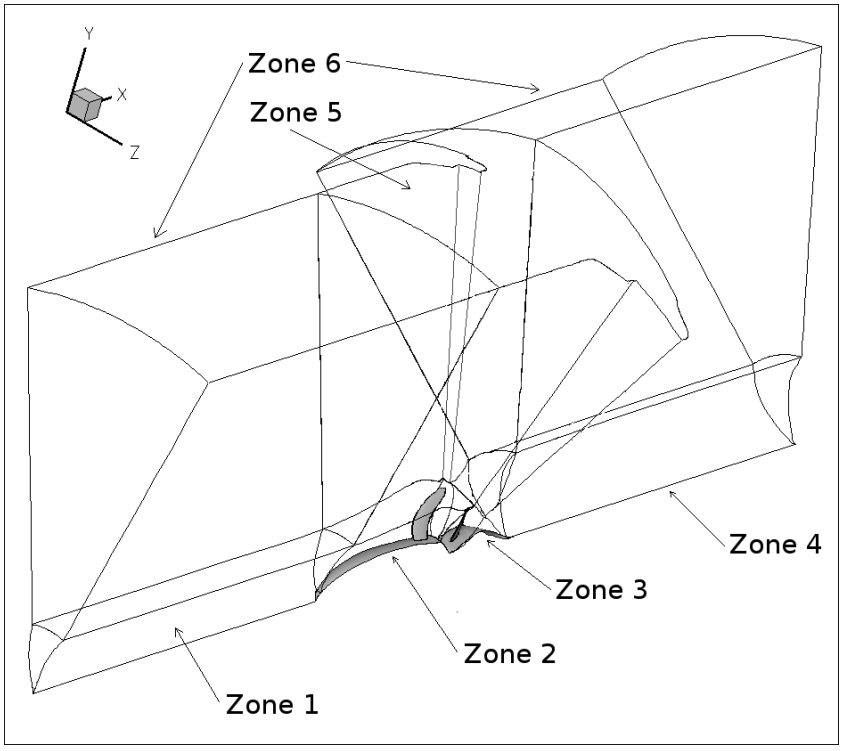

Figure 3.15: Scheme of the mesh zones, referred to the tables 3.1, 3.2, 3.3 on the following page

Domain parts	Points	Min Orthog.	Max Asp. Ratio	Max Exp. Ratio	Angle Dev.
Entire mesh	11804436	7.634	283589.1	5.068	36.9
Zone 1	353585	32.69	33933.25	2.159	19.886
Zone 2	3192405	21.992	20650.02	2.517	14.257
Zone 3	4094377	21.376	12414.32	2.969	36.9
Zone 4	476729	24.797	15409.92	1.903	21.048
Zone 5	3471390	7.934	283589.1	5.068	1.01
Zone 6	215950	76.306	37094.85	1.659	0.008

Table 3.1: Characteristics of the fine mesh: n points

Domain parts	Points	Min Orthog.	Max Asp. Ratio	Max Exp. Ratio	Angle Dev.
Entire mesh	5604072	90132	453730.8	5.097	36.828
Zone 1	164093	32.681	171858.5	2.056	20.653
Zone 2	1603157	27.547	29323.86	3.41	15.102
Zone 3	1874345	20.894	6185.032	4.802	36.828
Zone 4	186773	30.952	89774.04	1.958	17.28
Zone 5	1678838	9.132	453730.8	5.097	1.584
Zone 6	96866	69.393	89774.04	1.958	17.28

Table 3.2: Characteristics of the first coarse mesh: $n/2$ points

Domain parts	Points	Min Orthog.	Max Asp. Ratio	Max Exp. Ratio	Angle Dev.
Entire mesh	3025632	8.029	606328.5	4.35	36.436
Zone 1	90469	32.66	212142.8	2.523	21.176
Zone 2	904237	24.576	32403.13	3.597	28.676
Zone 3	989257	21.484	9273.49	3.436	36.436
Zone 4	90469	35.612	107628.5	2.577	20.598
Zone 5	902190	8.029	606328.5	4.35	8.385
Zone 6	49010	60.184	141345.9	2.902	7.028

Table 3.3: Characteristics of the second coarse mesh: $n/4$ points

Chapter 4

Solver: elsA

Contents

4.1 Introduction

The *elsA* project has been initially launched by ONERA (Office National d'Etudes et Recherches Aérospatiales) in 1997, to become in 2001, a collaboration with CERFACS (Centre Européen de Recherche et de Formation Avancée en Calcul Scientifique). The first operational version was delivered to industry partners in September 1998.

The *elsA* (standing for "ensemble logiciel de simulation en Aérodynamique") software is a multi-application CFD simulation platform dealing with internal and external aerodynamics from the low subsonic to the high supersonic flow regime. The compressible 3-D Reynolds averaged Navier-Stokes equations for arbitrary moving bodies are solved by a cell centered *finite-volume method* with various discretization schemes on multi-block structured meshes.

In the present chapter the equation system that is solved to perform the simulations is presented. The main assumptions are also treated to properly set the theoretical frame the calculations are based on. Moreover the numerical methods that have been used are briefly described, as well as some computational techniques applied to improve the calculation efficiency. A more detailed explanation of the implemented mathematical method can be found in the theoretical manual of *elsA* [19].

4.2 The Derivation of Conservation Laws

4.2.1 Integral and differential forms

To see how conservation laws arise from physical principles, we begin by deriving the equation for the conservation of mass in a one-dimensional gas dynamics problem. As during the whole study, we adopt a macroscopic description of the dynamic and thermodynamic behavior of the considered fluid, in general a gas. This supposes that all the scale length characteristics of the flow are large with respect to the mean free path of the molecules constitutive of the gas. Moreover, we admit:

- that the gas consists of only one species (atomic or molecular) or possibly of several species, but in this last case we are interested only in the mixture and suppose that these species are chemically inert and that the thermodynamic state of gas is at equilibrium and may described using only one temperature;
- that the density of the fluid is sufficiently low so that the effects of gravity may be neglected (massless fluid).

These are actually the main assumptions *elsA* code is based on.

To obtain the equation of mass conservation the classical case of a flow in a tube is analyzed. Moreover, in order to have only one space dimension from which the flow is dependent we assume that the properties of the gas, such as density and velocity, are assumed to be constant across each cross section. Let x represent the distance along the tube and $\rho(x,t)$ be the density of the gas at point x and time t. This density is defined in such a way that the total mass of gas in any given section from x_1 to x_2, say, is given by the integral of the density

$$\text{mass in } [x_1, x_2] \text{ at the time } t = \int_{x_1}^{x_2} \rho(x,t)\,\mathrm{d}x. \tag{4.1}$$

If we assume that the walls of the tube are impermeable and that mass is neither created nor destroyed, then the mass in this one section can change only because of gas flowing across the endpoints x_1 or x_2.

Now let $v(x,t)$ be the velocity of the gas at the point x time t. Then the rate of flow, or **flux** of gas past this point is given by

$$\text{mass flux at } (x,t) = \rho(x,t)v(x,t). \tag{4.2}$$

By our comments above, the rate of change of mass in $[x_1, x_2]$ is given by the difference in fluxes at x_1 and x_2

$$\frac{\mathrm{d}}{\mathrm{d}t}\int_{x_1}^{x_2}\rho(x,t)\,\mathrm{d}x = \rho(x_1,t)v(x_1,t) - \rho(x_2,t)v(x_2,t). \tag{4.3}$$

This is one **integral form** of the conservation law. Another form is obtained by integrating this in time from t_1 to t_2, giving an expression for the mass in $[x_1, x_2]$ at time $t_2 > t_1$ in terms of the mass at time t_1 and the total (integrated) flux at each boundary during this time period

$$\int_{x_1}^{x_2}\rho(x,t_2)\,\mathrm{d}x = \int_{x_1}^{x_2}\rho(x,t_1)\,\mathrm{d}x + \int_{t_1}^{t_2}\rho(x_1,t)v(x_1,t)\,\mathrm{d}t - \int_{t_1}^{t_2}\rho(x_2,t)v(x_2,t)\,\mathrm{d}t \tag{4.4}$$

To derive the **differential form** of the conservation law, we must introduce an important assumption: $\rho(x,t)$ and $v(x,t)$ are differentiable functions. Thence, using

$$\rho(x,t_2) - \rho(x,t_1) = \int_{t_1}^{t_2}\frac{\partial}{\partial t}\rho(x,t)\,\mathrm{d}t \tag{4.5}$$

and

$$\rho(x_2,t)v(x_2,t) - \rho(x_1,t)v(x_1,t) = \int_{x_1}^{x_2}\frac{\partial}{\partial x}\big(\rho(x,t)v(x,t)\big)\,\mathrm{d}x \tag{4.6}$$

in (4.4) it gives

$$\int_{t_1}^{t_2}\int_{x_1}^{x_2}\left\{\frac{\partial}{\partial t}\rho(x,t) + \frac{\partial}{\partial x}\big(\rho(x,t)v(x,t)\big)\right\}\mathrm{d}x\,\mathrm{d}t = 0. \tag{4.7}$$

Since this must hold for any section $[x_1, x_2]$ and over any time interval $[t_1, t_2]$, we conclude that in fact the integrand in (4.7) must be identically zero, that means

$$\rho_t + (\rho v)_x = 0 \qquad \text{conservation of mass} \tag{4.8}$$

which is the desired **differential form** of the conservation law for the conservation of mass, where the subscripts indicate the relative partial derivative.

Typically the equation (4.8) must be solved in conjunction with equations for the conservation of momentum and energy, which can be obtained with some similar processes. Moreover these last equations involve some other quantities: the pressure p, the viscous shear stress τ and the heat flux q. Therefore in order to solve the system a model of the fluid is needed. The necessary relations that allow to close the problem are treated in the next section. The three equations for the conservation of mass, momentum and energy form the **Navier-Stokes System**. Based on the continuum assumption, it can be written as

$$\boxed{\frac{\partial W}{\partial t} + \frac{\partial}{\partial x}(f - f_v) + \frac{\partial}{\partial y}(g - g_v) + \frac{\partial}{\partial z}(h - h_v) = 0} \tag{4.9}$$

where

$$W = \begin{pmatrix} \rho \\ \rho u \\ \rho v \\ \rho w \\ \rho E \end{pmatrix} \quad \text{is the vector of the conservative variables,} \tag{4.10}$$

$$f = \begin{pmatrix} \rho u \\ \rho u^2 + p \\ \rho uv \\ \rho uw \\ \rho u(\rho E + p) \end{pmatrix}, \; g = \begin{pmatrix} \rho u \\ \rho vu \\ \rho v^2 + p \\ \rho vw \\ \rho v(\rho E + p) \end{pmatrix}, \; h = \begin{pmatrix} \rho w \\ \rho wu \\ \rho wv \\ \rho w^2 + p \\ \rho w(\rho E + p) \end{pmatrix} \quad \text{are the convective fluxes,} \tag{4.11}$$

$$f_v = \begin{pmatrix} 0 \\ \tau_{xx} \\ \tau_{xy} \\ \tau_{xz} \\ (\tau\vec{U})_x - q_x \end{pmatrix}, \; g_v = \begin{pmatrix} 0 \\ \tau_{yx} \\ \tau_{yy} \\ \tau_{yz} \\ (\tau\vec{U})_y - q_y \end{pmatrix}, \; h_v = \begin{pmatrix} 0 \\ \tau_{zx} \\ \tau_{zy} \\ \tau_{zz} \\ (\tau\vec{U})_z - q_z \end{pmatrix} \quad \text{are the viscous fluxes.} \tag{4.12}$$

introducing the total energy per unit mass E and the velocity vector $\vec{U} = (u, v, w)^T$. Thence the terms of viscous dissipation are

$$\begin{aligned} (\tau\vec{U})_x &= \tau_{xx}u + \tau_{xy}v + \tau_{xz}w \\ (\tau\vec{U})_y &= \tau_{yx}u + \tau_{yy}v + \tau_{yz}w \\ (\tau\vec{U})_z &= \tau_{zx}u + \tau_{zy}v + \tau_{zz}w \end{aligned} \tag{4.13}$$

4.2.2 Closure of the problem

As mentioned above, some further information are necessary to close the problem. In particular, by knowing some fluid characteristics, this can be done specifying the scalar p, the tensor τ and the vector q as functions of the conservatives variables ρ, $\rho\vec{U}$ and ρE.

Thermodynamic characteristics

A complete description of the thermodynamics state of the gas must be included in the Navier Stokes system. In order to describe the relations that allow to obtain the expressions $p = p(\rho, \vec{U}, E)$ and $q = q(\rho, \vec{U}, E)$ the discussion proposed by Callen [5] and Galgani and Scotti [6] is followed. Therefore the properties of a thermodynamics system are defined focusing on the central role played by his fundamental thermodynamic relation. This relation is the

starting theoretical point to introduce the intensive thermodynamics variables and to obtain the equations of state of the system. The purpose of this approach is to show how a complete description of the thermodynamics of the gas is finally included in the system (4.9), even if only a single equation of state is actually visible.

For a mono-component simple fluid [5] in thermodynamic equilibrium, all the thermodynamic properties of the system are defined by a *fundamental relation* which specifies an extensive quantity of the system, the entropy S in terms of the extensive variables (internal) energy E_i, volume V and mass M:

$$S = S(E_i, V, M) \tag{4.14}$$

This equation represents the **fundamental thermodynamic relation** in the **entropic representation**. Thanks to the property of the temperature to be always positive, this relation is monotone with respect to the internal energy, thence we can now invert the equation considering the internal energy as unknown, obtaining the **energetic representation** [7].

$$E_i = E_i(S, V, M) \tag{4.15}$$

The *equations of state* are obtained by taking the partial derivatives of the fundamental relation and by assuming these functions as definition of the intensive variables.

$$\mathrm{d}E_i = \left.\frac{\partial E_i}{\partial S}\right|_{V,M} \mathrm{d}S + \left.\frac{\partial E_i}{\partial V}\right|_{S,M} \mathrm{d}V + \left.\frac{\partial E_i}{\partial M}\right|_{S,V} \mathrm{d}M \tag{4.16}$$

$$T \doteq \left.\frac{\partial E_i}{\partial S}\right|_{V,M} \qquad P \doteq -\left.\frac{\partial E_i}{\partial V}\right|_{S,M} \qquad \gamma \doteq \left.\frac{\partial E_i}{\partial M}\right|_{S,V} \tag{4.17}$$

Moreover the enthalpy and the Helmholtz and Gibbs (free) energies can also be obtained from the fundamental relation by using the Legendre transformation.

$$F = E_i - ST \qquad \rightarrow \qquad \text{Helmholtz Free Energy} \tag{4.18}$$

$$G = E_i - ST + PV \qquad \rightarrow \qquad \text{Gibbs Free Energy} \tag{4.19}$$

$$H = E_i + PV \qquad \rightarrow \qquad \text{Enthalpy} \tag{4.20}$$

From which the *specific heat capacities* can now be obtained by a further derivation

$$C_p \doteq \frac{T}{M}\left.\frac{\partial S}{\partial T}\right|_P = \frac{1}{M}\left.\frac{\partial H}{\partial T}\right|_P \tag{4.21}$$

$$C_v \doteq \frac{T}{M}\left.\frac{\partial S}{\partial T}\right|_V = \frac{1}{M}\left.\frac{\partial M}{\partial T}\right|_V \tag{4.22}$$

Pressure Expression In the case of a *Polytropic Ideal Gas* the fundamental relation in the energetic representation, in terms of specific values (per unit mass), is

$$e = (s, v) = e_0 \exp(\delta(s - s_0)/R) \left(\frac{v_0}{v}\right)^{\delta} \qquad \text{with} \qquad \delta = \gamma - 1 \tag{4.23}$$

where e, s, v are the internal energy, entropy and the volume per unit mass, e_0, s_0, v_0 are the specific internal energy, entropy and volume of a reference state 0, $R = 287.058\, J/(kgK)$ is the ideal gas constant and $\gamma = 1.4$ is the specific heat ratio.

Therefore the intensive variables temperature and pressure are specified by the equations of state

$$\begin{cases} T \doteq \left.\dfrac{\partial e}{\partial s}\right|_v = \dfrac{\delta e}{R} \\ P \doteq -\left.\dfrac{\partial e}{\partial v}\right|_s = \dfrac{\delta e}{v} \end{cases} \tag{4.24}$$

From which the classic equation of state is easily deducted:

$$Pv = RT \tag{4.25}$$

The system (4.24) still represents a complete thermodynamic description of the gas, but to obtain the state equation we have obviously lost some information. This confirms the thermodynamic principle that two equations of state are necessary to completely specify the thermodynamic properties of a fluid, at least in the case of a simple (mono-component) fluid system, see Callen [5].

In order to find the relation to specify the pressure in terms of conservative variables, we can simply use the second equation of the system (4.24), aware that some information about entropy variations have been lost.

$$E = e + \frac{1}{2}U^2 = \frac{p}{(\gamma - 1)\rho} + \frac{1}{2}U^2 \tag{4.26}$$

$$\Rightarrow \qquad \boxed{P = P(\rho, U, E) = \left(E - \frac{1}{2}U^2\right)(\gamma - 1)\rho} \tag{4.27}$$

In this connection, it is worth reminding that a second equation of state, although not explicitly used in the solution of the Euler equations, plays actually a role in selecting the physically relevant unique solution within the infinite set of weak solutions of the nonlinear hyperbolic problem through the intermediate of the *entropy condition*.

Heat Flux Expression The conduction heat flux vector is specified by the Fourier's law.

$$\boxed{q_x = -\alpha \frac{\partial T}{\partial x}, \qquad q_y = -\alpha \frac{\partial T}{\partial y}, \qquad q_z = -\alpha \frac{\partial T}{\partial z}} \tag{4.28}$$

where

$$\alpha = \frac{\mu C_p}{Pr} \tag{4.29}$$

with $Pr = 0.72$ for the air, and C_p is the specific heat capacity at constant pressure, obtained by the fundamental relation in the energetic representation:

$$C_p = \left.\frac{\partial h}{\partial T}\right|_P = R\frac{\gamma}{\gamma - 1} \tag{4.30}$$

Fluid Mechanical Behavior

In order to specify the shear stress tensor $\tau = \tau(\rho, \vec{U}, E)$, the mechanical behavior of the fluid has to be known. For a Newtonian fluid, like the air, the stress versus strain rate curve is linear and passes through the origin. The constant of proportionality is the viscosity. Therefore the tensor elements are

$$\boxed{\begin{array}{ll} \tau_{xx} = 2\mu\frac{\partial u}{\partial x} + \lambda\Big(\frac{\partial u}{\partial x} + \frac{\partial v}{\partial y} + \frac{\partial w}{\partial z}\Big), & \tau_{xy} = \tau_{yx} = \mu\Big(\frac{\partial v}{\partial x} + \frac{\partial u}{\partial y}\Big) \\ \tau_{yy} = 2\mu\frac{\partial v}{\partial y} + \lambda\Big(\frac{\partial u}{\partial x} + \frac{\partial v}{\partial y} + \frac{\partial w}{\partial z}\Big), & \tau_{xz} = \tau_{zx} = \mu\Big(\frac{\partial w}{\partial x} + \frac{\partial u}{\partial z}\Big) \\ \tau_{zz} = 2\mu\frac{\partial w}{\partial z} + \lambda\Big(\frac{\partial u}{\partial x} + \frac{\partial v}{\partial y} + \frac{\partial w}{\partial z}\Big), & \tau_{yw} = \tau_{wy} = \mu\Big(\frac{\partial v}{\partial z} + \frac{\partial w}{\partial y}\Big) \end{array}} \tag{4.31}$$

with

$$\mu = 1.78938\,10^{-5}\,Kg/(m\,s)$$

$$\lambda = \beta - \frac{2}{3}\mu$$

where β is the *Volume Viscosity*, that is near zero for a mono-atomic gas and μ is the *Dynamic Viscosity*, whose dependency from the temperature is taken into account by the Sutherland's law.

4.3 Averaged Navier Stokes Equations

4.3.1 Statistical Treatment

Turbulent flows are modeled by non-linear relations. This involves a wide range of spatial and temporal scales associated to the different phenomena that occur in the flow. In particular the

smallest scale turbulent dynamics play a fundamental role in the energy conservation. In fact, according to the Kolmogorov theory, the turbulent dissipation occurs just in these structures [9]. Therefore it is really important to model, in some way, this kind of phenomena. Nevertheless to capture the smallest scales a very fine time and space discretization is needed, which is absolutely not compatible with the memory and CPU time limitations that are normally imposed by the employed hardware.

From the identification of these different scales the RANS (Reynolds Averaged Navier-Stokes) and U-RANS (Unsteady RANS) methods are derived. The main idea is that the space and time discretization have to be fine enough to simulate the *mean motion*, while some specific *turbulence models* are used to take into account the fluctuation with respect to the mean motion.

Let $\overline{\phi}$ be the mean field and ϕ' the fluctuation field, which together form the complete field $\phi(x,t)$. In particular if $\overline{\phi}$ is a steady mean flow we can base the statical discussion on the values taken by the variable ϕ during some N different observations of the field: $\phi_k(x,t)$. Therefore, in the particular case of a steady flow, the mean value is defined by

$$\overline{\phi}(x) = \lim_{N\to\infty} \frac{1}{N} \sum_{k=1}^{N} \phi_k(x,t) \tag{4.32}$$

In the case of a periodic mean flow, a time step should be properly identified to exclude the turbulent fluctuation but capture the time dependency of the mean flow, in fact a phase average has to be performed. This technique is based on the assumption that the signal is formed by three components: a steady mean, a periodic component and fluctuations. In this case the time step needs to be larger than the turbulent dynamics, but small enough to allow a good reconstruction of the periodic component, which represents the time dependency of the mean motion.

Subsequently the complete field is defined by

$$\phi = \overline{\phi} + \phi', \qquad \text{with} \qquad \overline{\phi'} = 0 \tag{4.33}$$

This decomposition was proposed by Reynolds in 1883 [11]. Nonetheless for compressible flows it is useful to introduce a density weighted mean. This technique is also proposed by Reynolds, and extended to compressible flows by Favre [12].

$$\phi = \widetilde{\phi} + \phi'', \qquad \text{with} \qquad \widetilde{\phi''} = 0 \tag{4.34}$$

where

$$\widetilde{\phi} = \frac{\overline{\rho\phi}}{\overline{\rho}} \tag{4.35}$$

and the fluctuation field must respect the conditions

$$\begin{cases} \overline{\rho\phi''} = 0 \\ \overline{\phi''} \neq 0 \end{cases} \tag{4.36}$$

4.3.2 Mean Flow Equations

Both average techniques are used to obtain the Navier Stokes system in the form solved by *elsA* for the mean field. In particular the density weighted mean allows to treat the thermal and cinematic variables.

$$\begin{aligned}
&\rho = \overline{\rho} + \rho', && \overline{\rho'} = 0 \\
&P = \overline{P} + P', && \overline{P'} = 0 \\
&u_i = \widetilde{u_i} + u_i'', && \overline{\rho u_i''} = 0, \qquad i = 1,2,3 \\
&T = \widetilde{T} + T'', && \overline{\rho T''} = 0 \\
&E = \widetilde{E} + E'', && \overline{\rho E''} = 0
\end{aligned} \tag{4.37}$$

Therefore, the averaged form of the equation (4.9) is

$$\boxed{\frac{\partial \overline{W}}{\partial t} + \frac{\partial}{\partial x}(\overline{f} - \overline{f_v}) + \frac{\partial}{\partial y}(\overline{g} - \overline{g_v}) + \frac{\partial}{\partial z}(\overline{h} - \overline{h_v}) = 0} \tag{4.38}$$

where the unknowns and the convective flux vectors maintain the same structure:

$$\overline{W} = \begin{pmatrix} \overline{\rho} \\ \overline{\rho}\widetilde{u} \\ \overline{\rho}\widetilde{v} \\ \overline{\rho}\widetilde{w} \\ \overline{\rho}\widetilde{E} \end{pmatrix}, \quad \overline{f} = \begin{pmatrix} \overline{\rho}\widetilde{u} \\ \overline{\rho}\widetilde{u}^2 + \overline{p} \\ \overline{\rho}\widetilde{u}\widetilde{v} \\ \overline{\rho}\widetilde{u}\widetilde{w} \\ \overline{\rho}\widetilde{u}(\overline{\rho}\widetilde{E} + \overline{p}) \end{pmatrix}, \quad \overline{g} = \begin{pmatrix} \overline{\rho}\widetilde{u} \\ \overline{\rho}\widetilde{v}\widetilde{u} \\ \overline{\rho}\widetilde{v}^2 + \overline{p} \\ \overline{\rho}\widetilde{v}\widetilde{w} \\ \overline{\rho}\widetilde{v}(\overline{\rho}\widetilde{E} + \overline{p}) \end{pmatrix}, \quad \overline{h} = \begin{pmatrix} \overline{\rho}\widetilde{w} \\ \overline{\rho}\widetilde{w}\widetilde{u} \\ \overline{\rho}\widetilde{w}\widetilde{v} \\ \overline{\rho}\widetilde{w}^2 + \overline{p} \\ \overline{\rho}\widetilde{w}(\overline{\rho}\widetilde{E} + \overline{p}) \end{pmatrix} \tag{4.39}$$

While the viscous fluxes become

$$f_v = \begin{pmatrix} 0 \\ \overline{\tau_{xx}} - \overline{\rho}\widetilde{u''u''} \\ \overline{\tau_{xy}} - \overline{\rho}\widetilde{u''v''} \\ \overline{\tau_{xz}} - \overline{\rho}\widetilde{u''w''} \\ (\overline{\tau}\widetilde{U})_x - \overline{q_x} - \overline{\rho E'' u''} - \overline{P u''} + \overline{\tau_{xx} u''} + \overline{\tau_{xy} u''} + \overline{\tau_{xz} u''} \end{pmatrix}$$

$$g_v = \begin{pmatrix} 0 \\ \overline{\tau_{yx}} - \overline{\rho}\widetilde{v''u''} \\ \overline{\tau_{yy}} - \overline{\rho}\widetilde{v''v''} \\ \overline{\tau_{yz}} - \overline{\rho}\widetilde{v''w''} \\ (\overline{\tau}\widetilde{U})_y - \overline{q_y} - \overline{\rho E'' v''} - \overline{P v''} + \overline{\tau_{yx} v''} + \overline{\tau_{yy} v''} + \overline{\tau_{yz} v''} \end{pmatrix} \tag{4.40}$$

$$h_v = \begin{pmatrix} 0 \\ \overline{\tau_{zx}} - \overline{\rho}\widetilde{w''u''} \\ \overline{\tau_{zy}} - \overline{\rho}\widetilde{w''v''} \\ \overline{\tau_{zz}} - \overline{\rho}\widetilde{w''w''} \\ (\overline{\tau}\widetilde{U})_z - \overline{q_z} - \overline{\rho E'' w''} - \overline{P w''} + \overline{\tau_{zx} w''} + \overline{\tau_{zy} w''} + \overline{\tau_{zz} w''} \end{pmatrix}$$

in which, for a mono-atomic fluid, the components of the averaged stress tensor $\overline{\tau}$ are defined by

$$\overline{\tau_{ij}} = \overline{\mu}\left(\frac{\partial \widetilde{u}_i}{\partial x_j} + \frac{\partial \widetilde{u}_j}{\partial x_i} - \frac{2}{3}\delta_{ij}\left(\frac{\partial \widetilde{u}_i}{\partial x_i} + \frac{\partial \widetilde{u}_j}{\partial x_j} + \frac{\partial \widetilde{u}_k}{\partial x_k}\right)\right) \tag{4.41}$$

where δ_{ij} is the Kronecker Delta, which takes the value 1 if $i = j$, and 0 otherwise.

The most important difference between the system (4.38) and the system (4.9) is the presence of the fluctuation terms. This comes from the inherent non-linear nature of the equations, which involves that it is not possible to study only the mean flow because it is coupled with the turbulence fluctuations. This unknown terms are called *Reynolds Stresses*: $\widetilde{u_i'' u_j''}$, and form a symmetric tensor whose trace is actually the double of the *Turbulent Kinetic Energy*: $k = \frac{1}{2}\sum_i \widetilde{u_i'' u_i''}$

Taking into account the energy equation, the polytropic ideal gas model can be applied to obtain

$$\begin{aligned} \overline{\rho E'' u_i''} &= c_v \overline{\rho T'' u_i''} + \overline{\rho u_i'' u_j''}\widetilde{u}_i + \frac{1}{2}\overline{\rho u_j'' u_j'' u_i''} \\ \overline{P u_i''} &= (\gamma - 1) c_v \overline{\rho T'' u_i''} \end{aligned} \tag{4.42}$$

Therefore the total energy component of the viscous flux become

$$\overline{f_{i\,5}^v} = \widetilde{u}_j \overline{\tau_{ij}} - \overline{q_i} - c_p \overline{\rho T'' u_i''} - \overline{\rho u_i'' u_j''}\widetilde{u}_i + \frac{1}{2}\overline{\rho u_j'' u_j'' u_i''} + \overline{\tau_{ij} u_j''} - \overline{P' u_i''} \tag{4.43}$$

where the terms $\overline{\tau_{ij} u_j''}$ and $-\overline{P' u_i''}$ can be neglected within a boundary layer and for Mach number lower than 5, according to the Morkovin's hypothesis [16]. In fact he observed that in this case the turbulence maintains an incompressible behavior.

In conclusion the average process involves a loss of information about turbulent dynamics, which affects also the mean flow solution. Nonetheless this process provides a new equation system, where some new variables are present:

- the Reynolds stress $\widetilde{u_i'' u_j''}$
- the turbulent heat flux $c_p \overline{\rho T'' u_i''}$
- the third order term $\frac{1}{2}\overline{\rho u_j'' u_j'' u_i''}$ which will be neglected.

This rises the need of some specific techniques to close the problem, which can also model some of the lost information.

4.3.3 Turbulence models

According to the development presented in section (4.3) the purpose of the turbulence models is to close the RANS equation system. In particular the quantities that need to be modeled are the **Reynolds stress tensor** $\widetilde{u_i'' u_j''}$ and the **turbulent heat flux** $c_p \overline{\rho T'' u_i''}$.

Spalart-Allmaras and $k-\omega$ models have been applied to perform the simulations of the present study, and both are based on the *Boussinesq Hypothesis*. Even before that Reynolds brought to light the connection between turbulent stresses and velocity fluctuations, Boussinesq proposed to use a *turbulent isotropic viscosity* $\mu^{(t)}$ (also referred to as *eddy viscosity*). It is a scalar quantity able to play the role of the molecular viscosity μ in representing the dependency between the strain rate and the stress tensors. In this way the turbulent stresses will be specified as functions of the mean flow. Therefore, in analogy with the equation (4.41), the Reynolds stress tensor can be specified by the (4.44).

To obtain this expression a fundamental role is played also by the kinetic energy of turbulence $k = \frac{1}{2}\sum_i \widetilde{u_i''u_i''}$, that is a half of the trace of the Reynolds stress tensor. In fact this tensor is directly taken into account simply as $(-\frac{2}{3}\overline{\rho}k)I$, becoming a second quantity that can be modeled to finally consider the effects of the Reynolds stress tensor $\widetilde{u_i''u_j''}$ and the turbulent heat flux $c_p\overline{\rho T''u_i''}$.

Thence by modeling the two quantities, turbulent viscosity $\mu^{(t)}$ and turbulent kinetic energy k, the following expressions can be written:

$$\tau_{ij}^{(t)} = -\frac{2}{3}\delta_{ij}\left(\mu^{(t)}\left(\frac{\partial\widetilde{u}_i}{\partial x_i}+\frac{\partial\widetilde{u}_j}{\partial x_j}+\frac{\partial\widetilde{u}_k}{\partial x_k}\right)+\overline{\rho}k\right)+\mu^{(t)}\left(\frac{\partial\widetilde{u}_i}{\partial x_j}+\frac{\partial\widetilde{u}_j}{\partial x_i}\right) \tag{4.44}$$

$$q_i^{(t)} = -\frac{c_p\mu^{(t)}}{Pr^{(t)}}\frac{\partial\widetilde{T}}{\partial x_i} \tag{4.45}$$

Turbulence models play a key role when performing RANS simulations of turbulent flows. The prediction of physical flow phenomena such as boundary layer separation, wall friction or shock-boundary layer interactions strongly depends on the choice of the turbulence model. Most of first-order models rely on the local equilibrium idea to directly specify the turbulent viscosity in terms of known quantities of the mean flow. Among these, the algebraic models are robust and cheap, nonetheless their underlying physical assumptions limit the complexity of flows that can be adequately simulated. Two-equations models are independent of an algebraic length scale and take naturally into account history effects through transport equations, and are therefore considered to be more general. A large number of this kind of models have been proposed in the literature and they actually show reasonable results for a large variety of flows. Nonetheless they need some corrections in the case of complex turbulent flows because they do not naturally account for streamline curvature and rotation, and they cannot describe the anisotropy of turbulence. Some modifications are also needed to predict adverse pressure gradient flows. To overcome some of these drawbacks two-equations models have been developed. Menter proposed the Shear Stress Transport (SST) correction for the $k-\omega$ model, which has been applied in the present work. However, stiff source terms and complex boundary and free stream conditions restrict their general applicability. One-equation models seem to be a good compromise between the algebraic and two-equations models. In particular the Spalart-Allmaras model, which solves a transport equation for the turbulent viscosity, became quite popular because of its reasonable results for a wide range of flow problems and its numerical properties.

Reynolds stress models, which do not rely on the eddy viscosity hypothesis, have a high potential to accurately predict complex three dimensional flows, where anisotropic non-linear effects are important. Nonetheless the large additional number of equations involves a high

computational cost. Moreover they include terms that are very difficult to model (more than the case of two-equations models). Finally these reasons do not yet permit their wide application.

The methods applied in the present study are based on transport equations, which are specified in the form

$$\frac{\mathrm{d}}{\mathrm{d}t}\int_{\Omega_i}\vec{W}^{(t)}\mathrm{d}\Omega+\oint_{S_i}\vec{F}_c\cdot\mathrm{d}\vec{s}-\oint_{S_i}\vec{F}_v\cdot\mathrm{d}\vec{s}=\int_{\Omega_i}Q\mathrm{d}\Omega \tag{4.46}$$

Introducing the vector of the turbulence variable $\vec{W}^{(t)}$. Therefore in this section the flux $\vec{F}_c$ and $\vec{F}_v$ will refer to the turbulence variables. In particular, if the transported quantities are $e_1 \dots e_n$, the terms of the (4.46) are:

- the vector of the turbulent variables $e_1 \dots e_n$:

$$\vec{W}_{e_1 \dots e_n} = [e_1 \dots e_n]^T \tag{4.47}$$

- the convective flux:

$$\oint_{S_i}\vec{F}_c\cdot\mathrm{d}\vec{s}=\oint_{S_i}\begin{bmatrix}e_1\\ \vdots\\ e_n\end{bmatrix}\vec{U}\cdot\mathrm{d}\vec{s} \tag{4.48}$$

- the diffusive flux:

$$\oint_{S_i}\vec{F}_v\cdot\mathrm{d}\vec{s}=-\oint_{S_i}\begin{bmatrix}(\mu+\frac{\mu^{(t)}}{\sigma_{e_1}})\vec{\nabla}e_1\\ \vdots\\ (\mu+\frac{\mu^{(t)}}{\sigma_{e_n}})\vec{\nabla}e_n\end{bmatrix}\cdot\mathrm{d}\vec{s} \tag{4.49}$$

  where $\sigma_{e_1} \dots \sigma_{e_n}$ are generally constant parameters, except in some models of the layer type, as Menter, where they are field functions.

While the source term has a specific expression which depends on the model considered.

$k-\omega$ with SST Menter modification

The first turbulence model used in the present study is the two-equations $k-\omega$ Wilcox model with the BSL (Baseline) Menter modification and the SST correction.

$k-\omega$ Wilcox Model In $k-\omega$ models the transported quantities are the kinetic energy of turbulence k and the specific rate of dissipation $\omega = \epsilon/(\beta^* k)$ [13]. Where $\beta^* = 0.09$ is a constant and ϵ is the isotropic rate of dissipation, which is an unknown in $k-\epsilon$ models like that which is used by the BSL modification, as shown in the following. Therefore in the transport equations (4.46) one finds:

$$\vec{W}_{(k\omega)} = [\rho k, \rho\omega]^T \qquad \text{with} \qquad \begin{cases} k: \text{ kinetic energy of turbulence} \\ \omega: \text{ specific rate of dissipation} \end{cases} \tag{4.50}$$

and the source term

$$\int_{\Omega_i} \vec{Q}_{(k\omega)} \mathrm{d}\Omega = \int_{\Omega_i} \begin{bmatrix} \tau^{(t)} \vec{\nabla}\vec{U} - \beta^* \rho K \omega \\ \frac{\gamma}{\nu^{(t)}} \tau^{(t)} \vec{\nabla}\vec{U} - \beta\rho\omega^2 \end{bmatrix} \mathrm{d}\Omega \tag{4.51}$$

Finally the eddy viscosity is defined as

$$\mu^{(t)} = \frac{\rho k}{\omega} \tag{4.52}$$

and the constants of the model are as follows:

$$\beta^* = 0.09 \qquad \sigma^* = 0.5 \qquad \sigma_{e_1} = \frac{1}{\sigma^*} \qquad \gamma = \frac{\beta}{\beta^*} - \sigma\frac{k^2}{\sqrt{\beta^*}}$$

$$\beta = 0.075 \qquad \sigma = 0.5 \qquad \sigma_{e_2} = \frac{1}{\sigma} \qquad k = 0.41$$

Baseline Menter model The main problem with the Wilcox $k-\omega$ model is its sensitivity to the ω value at the edge of the boundary layers and wakes. To avoid this problem, Menter developed the BSL (Baseline) model in the hope to preserve the good behavior of the Wilcox model in the internal area of boundary layers and to obtain an outer edge condition insensitive to the ω_∞ value. For that, he replaced the Wilcox model in the outer region of the boundary layers by a $k-\epsilon$ model of Launder-Sharma written in terms of $k-\omega$ variables [14]. This requires the introduction of a blending function F_1 between the models. This function is a sensor whose purpose is to separate the internal region of the boundary-layers, where the Wilcox model applies, from the external region (beyond $y/\delta \simeq 0.7$) where Launder-Sharma is used. The Wilcox model is also replaced by $k-\epsilon$ in the wakes. Therefore the source term of the model is written :

$$\int_{\Omega_i} \vec{Q}_{(k\omega)} \mathrm{d}\Omega = \int_{\Omega_i} \begin{bmatrix} \tau^{(t)} \vec{\nabla}\vec{U} - \beta^* \rho K \omega \\ \frac{\gamma}{\nu^{(t)}} \tau^{(t)} \vec{\nabla}\vec{U} - \beta\rho\omega^2 + 2\frac{\rho\sigma_\omega}{\omega} \vec{\nabla}k \cdot \vec{\nabla}\omega \end{bmatrix} \mathrm{d}\Omega \tag{4.53}$$

The constants are obtained by averaging the constants of each model, using the blending function F_1

$$C_{ste} = F_1 C_{ste1} + (1 - F_1) C_{ste2} \tag{4.54}$$

By making $F_1 = 1$, one finds the constants (subscripted "1") of the original Wilcox model. $F_1 = 0$ makes it possible to obtain the $k-\epsilon$ Launder-Sharma model, in a $k-\omega$ formulation, after a change of variables. The constants of this model are the following :

$$\begin{array}{llll} \sigma_1^* = 0.5 & \sigma_1 = 0.5 & \beta_1 = 0.075 & \sigma_{\omega 1} = 0 \\ \sigma_2^* = 1.0 & \sigma_2 = 0.856 & \beta_2 = 0.0828 & \sigma_{\omega 2} = 0.856 \\ \beta^* = 0.09 & k = 0.41 & \gamma = \dfrac{\beta_i}{\beta^*} - \sigma_i \dfrac{k^2}{\sqrt{\beta^*}}\,; & i = 1, 2 \end{array}$$

In particular the blending function F_1 is defined by

$$\begin{aligned} F_1 &= \tanh \zeta^4 \\ \zeta &= \min\left[\max\left(\frac{\sqrt{k}}{0.09\omega y}\,;\,\frac{500\nu}{\omega y^2}\right) \quad ; \quad \frac{4\rho\sigma_{\omega 2} k}{D_{k\omega} y^2}\right] \\ D_{k\omega} &= \max\left(\frac{\rho\sigma_{\omega 2}}{\omega}\vec{\nabla}k \cdot \vec{\nabla}\omega \quad ; \quad 10^{-20}\right) \end{aligned} \tag{4.55}$$

As it is noted, the function F_1 requires the calculation of the distance to the wall. It nevertheless is written in a purely local form to be easily coded without using topological information.

SST Correction of the Menter model The SST correction of Menter relies on the observation that for the models with 2 transport equations using the eddy viscosity concept, the ratio of the shear stress $\tau^{(t)}$ to the value of ρk is equal to the quantity $a_1\sqrt{P_k/D_k}$ (ratio of production over dissipation of k, with $a_1 \simeq 0.31$), whereas in experiments one measures rather $\tau^{(t)}/\rho k \simeq a_1$ in a large part of the boundary layer.
In the case of flows in the presence of positive gradients of pressure, the ratio P_k/D_k can be definitely higher than 1 which leads, with the 2 equation models, to over-estimate the shear stress and thus, indirectly, to underestimate the effect of the positive pressure gradients. To cure this inconsistency Menter then proposes to limit the eddy viscosity coefficient by using the function

$$\begin{aligned} \mu^{(t)} &= \frac{\rho k}{\max\left(\omega\,,\,\mathrm{rot}(\vec{U})F_2/a_1\right)} \qquad \text{where} \qquad a_1 = \sqrt{\beta^*} \\ F_2 &= \tanh \iota^2 \qquad \text{with} \qquad \iota = \max\left(\frac{2\sqrt{k}}{0.09\omega y}\,,\,\frac{500\nu}{y^2\omega}\right) \end{aligned} \tag{4.56}$$

The SST correction of the Menter model can, in theory, correct any model of the $k-\epsilon$ type which has trouble to predict separations sufficiently early, since its effect is to reduce the $\mu^{(t)}$ value. This correction is also coded in *elsA* for the Wilcox model.

Spalart-Allmaras

The Spalart-Allmaras model ([15]) uses only one transport equation for the *kinematic viscosity transform* $\widetilde{\nu}$ which, far from the walls, merges with $\nu^{(t)} = \mu^{(t)}/\rho$. The equation for $\widetilde{\nu}$ results from a step by step construction by addition of terms intended for taking into account more and more physical phenomena. On the basis of a "convection = production + diffusion" form for free shear flows, the Spalart-Allmaras model adds the terms necessary to obtain a logarithmic zone

in the velocity profiles. It ends by terms intended to trigger the laminar-turbulent transition, its position being supposed known a priori. These last terms are described at the end of this part.

Therefore the Spalart-Allmaras transport equation is composed by the following terms, according to the (4.46) form:

- the vector of the turbulent variable:

$$\vec{W}_{(\widetilde{\nu})} = \rho\widetilde{\nu} \tag{4.57}$$

- the convective flux:

$$\oint_{S_i} \vec{F}_{c_{(\widetilde{\nu})}} \cdot \mathrm{d}\vec{s} = \oint_{S_i} \rho\widetilde{\nu}\vec{U} \cdot \mathrm{d}\vec{s} \tag{4.58}$$

- the diffusive flux:

$$\oint_{S_i} \vec{F}_{v_{(\widetilde{\nu})}} \cdot \mathrm{d}\vec{s} = -\oint_{S_i} \frac{1}{\sigma_{\widetilde{\nu}}}(\mu + \rho\widetilde{\nu})\vec{\nabla}\widetilde{\nu} \cdot \mathrm{d}\vec{s} \tag{4.59}$$

- the source term:

$$\begin{aligned} &\int_{\Omega_i} \vec{Q}_{(\widetilde{\nu})} \mathrm{d}\Omega = \\ &\qquad \int_{\Omega_i} \left(C_{b1}(1 - f_{t2})\widetilde{S}\rho\widetilde{\nu} + \frac{C_{b2}}{\sigma}\vec{\nabla}(\rho\widetilde{\nu}) \cdot \vec{\nabla}\widetilde{\nu} - C_{\omega 1} f_\omega - \frac{C_{b1}}{k^2} f_{t2} \rho \frac{\widetilde{\nu}^2}{\eta^2} \right) \mathrm{d}\Omega \end{aligned} \tag{4.60}$$

with:

$$\left\{ \begin{array}{c} \widetilde{S} = \overline{\omega} + \dfrac{\widetilde{\nu}}{k^2\eta^2} f_{v2} \quad ; \quad f_{v2} = 1 - \dfrac{\chi}{1 + \chi f_{v1}} \quad ; \quad \chi = \dfrac{\rho\widetilde{\nu}}{\mu} \\ f_\omega = g\left(\dfrac{1 + C_{W3}^6}{g^6 + C_{W3}^6} \right)^{1/6} \quad ; \quad g = r + C_{\omega 2}(r^6 - r) \quad ; \quad r = \dfrac{\widetilde{\nu}}{\widetilde{S}k^2\eta^2} \\ f_{t2} = C_{T3} \exp(-C_{t4}\chi^2) \end{array} \right. \tag{4.61}$$

In which the constants take the following values:

$C_{b1} = 0.1355$	$\sigma = 2/3$	$C_{W3} = 2$	$C_{T3} = 1.2$
$C_{b2} = 0.622$	$k = 0.41$	$C_{v1} = 7.1$	$C_{t4} = 0.5$
$C_{\omega 1} = C_{b1}/k^2 + (1 + C_b 2)/\sigma$	$C_{\omega 2} = 0.3$		

Finally the eddy viscosity is evaluated by the following relations:

$$\mu^{(t)} = \rho\widetilde{\nu} f_{v1} \quad ; \quad f_{v1} = \frac{\chi^3}{\chi^3 + C_{v1}^3} \quad ; \quad \chi = \frac{\rho\widetilde{\nu}}{\mu} \tag{4.62}$$

Additional term related to transition initiation The Spalart-Allmaras model admits $\widetilde{\nu} = 0$ as solution, even in the presence of longitudinal velocity gradients in the boundary layer. This solution is nevertheless unstable. To initiate the growth of the $\mu^{(t)}$ field, the solution must be disturbed. In the case of imposed transition, or for a very turbulent calculation, $\mu^{(t)}$ proportional to μ can be imposed after some iterations of calculation. But if a transition criterion is used this is not possible, thence Spalart introduced into its model an additional source term which is activated only in the vicinity of a user-defined transition point. This term is equal to $f_{T1}\Delta\vec{U}$ with

$$\begin{aligned} f_{T1} &= c_{T1} g_t \exp\left[-c_{t2}\frac{\omega_t^2}{\Delta U^2}(d^2 = g_t^2 d_t^2)\right] \\ \Delta U &= |U| - |U_t| \\ g_t &= \min(0\,,\,1\,,\,\frac{\Delta U}{\omega_t \Delta x_t}) \\ c_{T1} &= 1 \qquad c_{t2} = 2 \end{aligned} \tag{4.63}$$

introducing:

U_t : modulus of velocity at the transition point;
ω_t : modulus of rotational velocity at the point of transition;
d : cell distance from the wall;
d_t : cell distance from the wall, at the point of transition;
Δx_t : length of the cell of calculation at the transition point.

4.4 Finite Volume Discretization

This section will summarize some basic numerical concepts and issues. Several methods are available for the discretization of the conservation laws of fluid mechanics: finite differences (FDM), finite elements (FEM), and finite volumes (FVM). The approach implemented in *elsA* is the FVM which is by far the most general and the most widely applied. The reason behind the appeal to the FVM lies in its generality, its conceptual simplicity and its ease of implementation for arbitrary grids, structured as well as unstructured (even if, for instance, *elsA* can treat only the first type). Moreover the FVM has some remarkable properties which are important to remember, when developing or applying an existing CFD code. The FVM is based on *cell-averaged values*. This distinguishes the FVM from the finite differences and finite elements methods, where the main numerical quantities are the *local function values* at the mesh points.

Once a grid has been generated, the FVM consists in associating a local finite volume, also called *control volume*, to each mesh point and applying the integral conservation law to this local volume.

An essential advantage of the FVM is connected to the very important concept of *conservative discretization*. Is is fundamental to maintain the global conservation of the basic flow quantities, mass, momentum and energy, at the discrete level and this puts conditions on the way the discretization process of the equations is performed. Moreover the application of the integral form of the conservation relations ensure the capability of solving the hyperbolic Euler system, modeling shock waves as discontinuities.

The integral conservation laws, as the (4.3), are applied to each control volume Ω_i, associated to the mesh point i, defining hereby the equation for the unknowns W_i attached to the same vertex or cell

$$\frac{\partial}{\partial t}\int_{\Omega_i} W \mathrm{d}\Omega + \oint_{S_i} \vec{F}\cdot \mathrm{d}\vec{s} = \int_{\Omega_i} Q \mathrm{d}\Omega \tag{4.64}$$

where $\vec{F}$ is the flux of the scalar variable W through S_i, which is the whole external surface of the volume Ω_i, Q is a source term and $\mathrm{d}\vec{s} = \vec{n}\mathrm{d}s$ writing $\vec{n}$ the local normal versor of the infinitesimal surface $\mathrm{d}s$. The advantage of this method, especially in absence of source terms, is that the fluxes are calculated only on two dimensional surfaces instead of in the three dimensional space.

The equation (4.64) is then replaced by its discrete form, where the volume integrals are expressed as averaged values over the cell and the surface integral is replaced by a sum over all the bounding faces f of the considered volume.

$$\frac{\partial}{\partial t}(W_i\Omega_i) + \sum_{Faces} (\vec{F}\cdot\Delta\vec{s})_f = Q_i\Delta\Omega_i \tag{4.65}$$

where $\Delta\vec{s}$ specifies the multiplication between the local versor perpendicular to the face f and its surface. A general and important interpretation of any numerical, conservative scheme is obtained directly from the integral conservation laws. If the equation (4.64) is integrated from $t = n\Delta t$ to $(n+1)\Delta t$ for a control volume Ω_i associated to a node or a cell i, we obtain

$$\int_{\Omega_i} W \mathrm{d}\Omega\Big|^{n+1} = \int_{\Omega_i} W \mathrm{d}\Omega\Big|^{n} - \sum_{Faces}\int_n^{n+1} (\vec{F}\cdot\Delta\vec{S})_f \mathrm{d}t + \int_n^{n+1}\mathrm{d}t\int_{\Omega_i} Q\mathrm{d}\Omega \tag{4.66}$$

Subsequently the *cell and time-averaged* source $\overline{Q}_i^*$ and the *numerical flux* $\overline{F}^*$ over each side can be defined by introducing the *cell-averaged* conservative variable $\overline{W}_i^n$ and source $\overline{Q}_i^n$ at the time $n\Delta t$:

$$\overline{W}_i^n \doteq \frac{1}{\Omega_i}\int_{\Omega_i} W\mathrm{d}\Omega_i\Big|^n \qquad\qquad \overline{Q}_i \doteq \frac{1}{\Omega_i}\int_{\Omega_i} Q\mathrm{d}\Omega_i \tag{4.67}$$

$$\vec{F}^*\cdot\Delta\vec{S} \doteq \frac{1}{\Delta t}\int_n^{n+1}\vec{F}\cdot\Delta\vec{S}\mathrm{d}t \qquad\qquad \overline{Q}_i^* \doteq \frac{1}{\Delta t}\int_n^{n+1}\overline{Q}_i\mathrm{d}t \tag{4.68}$$

Therefore the conservative discretization takes the form

$$\overline{W}_i^{n+1}\Omega_i = \overline{W}_i^n\Omega_i - \Delta t\sum_{Faces}\vec{F}^*\cdot\Delta\vec{S} + \Delta t\overline{Q}_i^*\Omega_i \tag{4.69}$$

This is an exact relation for the time evolution of the space-averaged conservative variable $\overline{W}_i^n$ over the cell i. The numerical flux $\vec{F}^*$ completely identifies a scheme by the way it approximates

the time-averaged physical flux along each cell face. The absence of a time index on the balance of fluxes and on the source term is meant to indicate that one can choose between n for an *explicit scheme*, or $n+1$ for an *implicit scheme*.

The above formulation of a numerical scheme can be generalized if one considers that the space discretization is completely defined by its numerical flux, leaving open the choice of the time integration. A general numerical scheme can then be defined as a system of ordinary differential equations in time by

$$\frac{\mathrm{d}}{\mathrm{d}t}\overline{W}_i\Omega_i = -\sum_{Faces}\vec{F}^*\cdot\Delta\vec{S} + \overline{Q}_i^*\Omega_i \equiv -R_i \tag{4.70}$$

The right hand side defines the *residual* representing the balance of fluxes over the cell. This balance, in absence of source terms, must tend to zero at convergence for a steady state problem.

4.4.1 Convective fluxes

In order to derive the discretized flux form, the decomposition of the fluxes in convection and viscous terms, as shown above, is used. Thence the term $\oint_{S_i}\vec{F}\cdot\mathrm{d}\vec{s}$ of the equation (4.64) can be considered as

$$\oint_{S_i}\vec{F}\cdot\mathrm{d}\vec{s} \equiv \oint_{S_i}\vec{F}_c\cdot\mathrm{d}\vec{s} - \oint_{S_i}\vec{F}_v\cdot\mathrm{d}\vec{s} \tag{4.71}$$

With a structured mesh several methods have been developed to evaluate the convective flux. In the present study the centered *Jameson Scheme* and the upwind *Roe Scheme* have been used. A central scheme typically allows to obtain a higher precision than an upwind scheme, but in some configuration the first one can be not robust enough and the second can provide better results. In this section both schemes will be briefly described considering, for reasons of clarity, an incompressible flow.

The viscous fluxes modeling can be dealt with separately, therefore it will be described at the end of this section.

Central Discretization

The non-linear convective terms of the Navier Stokes equations $\vec{H} = \left(\vec{U}\vec{\nabla}\right)\cdot\vec{U}$ can be written in different forms by using the equation for the conservation of mass, which for an incompressible flow is $\vec{\nabla}\cdot\vec{U} = 0$. In particular the i-component of this term can be expressed as

$$H_i = \sum_l H_{il} \qquad \text{with} \qquad l = i,j,k \qquad \text{and} \tag{4.72}$$

- divergence form,

$$H_{il} = \frac{\partial u_i u_l}{\partial x_l} \tag{4.73}$$

- convective form,

$$H_{il} = u_l \frac{\partial u_i}{\partial x_l} \tag{4.74}$$

- skew symmetric form,

$$H_{il} = \frac{1}{2}\left(\frac{\partial u_i u_l}{\partial x_l} + u_l \frac{\partial u_i}{\partial x_l}\right) \tag{4.75}$$

Although these forms are strictly equivalent in the continuous Navier Stokes equation system, they involve different effects on the discretization error, as shown by Kravchenko and Moin [17]. These effects have to be taken into account in the choice of the discretization technique, in fact different methods provide different forms for the non-linear convective term [10].

Let us consider the cell i, whose interfaces with the near cells $i-1$ and $i+1$ are respectively $S_{i-1/2}$ and $S_{i+1/2}$. In this frame the numerical fluxes through the interfaces are $\vec{F}^*_{i-1/2}$ and $\vec{F}^*_{i+1/2}$. These fluxes depends on the values taken by the unknown variable at the both sides pf the interface. In particular with a central scheme, they can be calculated in two ways:

- as the flux of the average between the values of the unknown in the two cells, as proposed by Jameson *et al.* [23]

$$\vec{F}^*_{i+1/2} = \vec{F}^*\left(\frac{1}{2}(\vec{W}_i + \vec{W}_{i+1})\right) \tag{4.76}$$

- as the average of the fluxes obtained by the unknown in the two cells

$$\vec{F}^*_{i+1/2} = \frac{1}{2}\left(\vec{F}^*(\vec{W}_i) + \vec{F}^*(\vec{W}_{i+1})\right) \tag{4.77}$$

The difference between the two methods can be evaluated by using the one-dimension hyperbolic equation

$$\frac{\partial u}{\partial t} + \frac{\partial f(u)}{\partial x} = 0 \tag{4.78}$$

where the flux is $f(u) = u^2$. The finite volume method allows to derive the semi-discrete equation

$$V_i \frac{\partial u}{\partial t} + F^*_{i+1/2} - F^*_{i-1/2} = 0 \tag{4.79}$$

where V_i is the volume of the considered cell.

The evaluation of the fluxes with the method (4.76) provides

$$\frac{\partial u}{\partial t} + \frac{1}{\Delta x}\left[\left(\frac{u_{i+1} - u_i}{2}\right)^2 - \left(\frac{u_i - u_{i-1}}{2}\right)^2\right] = \frac{\partial u}{\partial t} + \frac{1}{2}\left(\frac{u^2_{i+1} - u^2_{i-1}}{2\Delta x} + 2u_i \frac{u_{i-1} - u_{i+1}}{2\Delta x}\right) = 0$$

(4.80)

which corresponds to the following second-order finite volume approximation for the flux derivative $\frac{\partial f(u)}{\partial x} = \frac{\partial u^2}{\partial x}$:

$$\frac{1}{2}\left(\frac{u_{i+1}^2 - u_{i-1}^2}{2\Delta x} + 2u_i\frac{u_{i+1} - u_{i-1}}{2\Delta x}\right) = \frac{\partial u^2}{\partial x} + \frac{1}{6}\frac{\partial^3 u^2}{\partial x^3}\Delta x^2 - \frac{1}{2}\frac{\partial u}{\partial x}\frac{\partial^2 u}{\partial x^2}\Delta x^2 + O(\Delta x^4) \quad (4.81)$$

In the same way, by the method (4.77)

$$\frac{\partial u}{\partial t} + \frac{u_{i+1}^2 - u_{i-1}^2}{2\Delta x} = 0 \quad (4.82)$$

is obtained, and its discretization error is

$$\frac{u_{i+1}^2 - u_{i-1}^2}{2\Delta x} = \frac{\partial u^2}{\partial x} + \frac{1}{6}\frac{\partial^3 u^2}{\partial x^3}\Delta x^2 + O(\Delta x^4) \quad (4.83)$$

Therefore the evaluation of the numerical fluxes by the equation (4.76) provides the approximation of the non-linear terms in the skew-symmetric form, while using the equation (4.77) the divergence form is obtained. The difference between the two approximation is the second order term $-\frac{1}{2}\frac{\partial u}{\partial x}\frac{\partial^2 u}{\partial x^2}\Delta x^2$ which involves an effect of diffusion or anti-diffusion, depending on the sign of $\frac{\partial u}{\partial x}$.

Kravchenko and Moin [17] showed that the skew-symmetric form entails a lower aliasing error, while the divergence form approximation is less dissipative.

Jameson's artificial viscosity The central schemes that are implemented in *elsA* are joined by the Jameson's model for the artificial viscosity [23]. This method adds to the central scheme some terms of the second and fourth order, to stabilize the method near discontinuities and high gradient regions. Thus, introducing F^J to refer to the center numerical flux with Jameson artificial viscosity, it can be written as

$$\vec{F}_{i+1/2}^{J} = \vec{F}_{i+1/2}^{*} - \mathrm{d}_{i+1/2} \quad (4.84)$$

Where the dissipation flux is defined by

$$\mathrm{d}_{i+1/2} = \epsilon_{i+1/2}^{(2)}(\vec{W}_{i+1} - \vec{W}_i) - \epsilon_{i+1/2}^{(4)}(\vec{W}_{i+2} - 3\vec{W}_{i+1} + 3\vec{W}_i - \vec{W}_{i-1}) \quad (4.85)$$

The coefficients $\epsilon_{i+1/2}^{(2)}$ and $\epsilon_{i+1/2}^{(4)}$ are used locally adapt the dissipation flux. The dependence from the local solution is given by the *scale factor* $r_{i+1/2}$, which is defined as the average of the spectral radius of the Jacobian matrix associated to the solution in the cells i and $i+1$.

$$\begin{aligned} \epsilon_{i+1/2}^{(2)} &= k^{(2)} r_{i+1/2}\nu_{i+1/2} \\ \epsilon_{i+1/2}^{(4)} &= max(0, k^{(4)} r_{i+1/2} - \epsilon_{i+1/2}^{(2)}) \end{aligned} \qquad \text{with} \qquad r_{i+1/2} = \frac{1}{2}\Big(\lambda(A)_i^I + \lambda(A)_{i+1}^I\Big) \quad (4.86)$$

where $\lambda(A)_i^I$ is the spectral radius of the Jacobian matrix $A = \frac{\partial\left(\vec{F}^*(\vec{W}_i)\cdot\overline{s}\right)}{\partial\vec{W}}$ calculated at the cell center with the averaged surface vector $\overline{s} = \frac{1}{2}(s_{i+1/2} + s_{i-1/2})$ in the I direction, for example. The sensor $\nu_{i+1/2}$ controls the dissipation near discontinuities, like shock waves. It can be obtained by the normalized second order pressure derivative

$$\mu_i = \left|\frac{p_{i+1} - 2p_i + p_{i-1}}{p_{i+1} + 2p_i + p_{i-1}}\right| \qquad \text{from which} \qquad \nu_{i+1/2} = max(\mu_i, \mu_{i+1}) \tag{4.87}$$

Therefore the pressure term in the definition of ϵ_2 is a second order term, except near high pressure gradient regions, where it become a first order. Near shock waves, for example, the term ϵ_2 is dominant. Nonetheless ϵ_2 do not prevent oscillations to occur where the gradient are not high enough to activate the second order viscosity. These fluctuations can reach about 1% for density variations and they can, in some cases, prevent the convergence to a steady state. To solve this problem the fourth order term is included, but limited near discontinuities by the increase of the second order term. In fact its effect are a low dissipation in the whole domain that can nonetheless reactivate some fluctuations where the gradients are very high.

For transonic steady flows some typical values of k^2 are between 0.5 and 1.0, while k^4 can vary from 0.01 to 0.03. For subsonic flows the second order artificial viscosity can be fixed to zero. In the case of incompressible flows the definition of ϵ_2 and ϵ_4 needs to be modified to adapt the dissipation fluxes to the convection fluxes.

Roe flux

A classical scheme involves the exact solution of the Riemann problem for each cell interface and for each time instant. These calculations, performed on the whole domain, are actually very expensive and the results are then averaged on each cell, losing most of the precise information obtained by the exact solution of the problem. The purpose of the Roe approximation is to use a simplified method to calculate the interface fluxes, obtaining approximate values whose average can be compared with an exact solutions average. In particular Roe proposes to linearize the Riemann problem, still maintaining some important numerical properties. Thence the classical hyperbolic problem

$$\frac{\partial\vec{W}}{\partial t} + \frac{\partial\vec{f}(\vec{W})}{\partial x} = 0 \tag{4.88}$$

where we can define the Jacobian matrix

$$A(\vec{W}) = \frac{\partial\vec{f}(\vec{W})}{\partial\vec{W}} \qquad \text{to obtain} \qquad \frac{\partial\vec{W}}{\partial t} + A(\vec{W})\frac{\partial\vec{W}}{\partial x} = 0 \tag{4.89}$$

becomes

$$\frac{\partial\vec{W}}{\partial t} + A^*(\vec{W}_L, \vec{W}_R)\frac{\partial\vec{W}}{\partial x} = 0 \tag{4.90}$$

where $\vec{W}_L, \vec{W}_R$ are the left and right solution of the Riemann problem at the considered interface.

In particular the linearized Jacobian matrix $A^*(\vec{W}_L, \vec{W}_R)$ is calculated by imposing the fundamental properties:

1. $A^*(\vec{W}_L, \vec{W}_R)\,(\vec{W}_R - \vec{W}_L) = f(\vec{W}_R) - f(\vec{W}_L)$
   to obtain a *conservative method* that exactly solves the Riemann problem if a *single discontinuity* occurs between the left and right states;

2. $A^*(\vec{W}_L, \vec{W}_R)$ has linear independent real positive eigenvalues
   to still have a hyperbolic problem which can be solved;

3. $A^*(\vec{W}_L, \vec{W}_R) \longrightarrow A(\vec{W})$ if $(\vec{W}_L, \vec{W}_R) \longrightarrow \vec{W}$
   to exactly solve continuous fluxes.

The linear matrix A^* can now be calculated as function of an intermediate state $\vec{W}^*$ between $\vec{W}_L$ and $\vec{W}_R$. In particular $A^*(\vec{W}_L, \vec{W}_R) = A(\vec{W}^*(\vec{W}_L, \vec{W}_R))$. The variables of $\vec{W}^*$ are defined, thanks to the properties shown above, with a ρ weighted average, known as *Roe Average*: $< \cdot >_{\sqrt{\rho}}$

$$\begin{aligned}
\rho^* &= <\rho^*>_{\sqrt{\rho}} = \sqrt{\rho_R \rho_L} \\
u_l^* &= <u_l^*>_{\sqrt{\rho}} = \frac{(\sqrt{\rho}u_l)_R + (\sqrt{\rho}u_l)_L}{\sqrt{\rho_R} + \sqrt{\rho_L}} \\
H^* &= <H^*>_{\sqrt{\rho}} = \frac{(\sqrt{\rho}H)_R + (\sqrt{\rho}H)_L}{\sqrt{\rho_R} + \sqrt{\rho_L}}
\end{aligned} \tag{4.91}$$

Therefore the Roe flux at the interface $i + 1/2$ is defined by

$$\vec{F}_{i+1/2} = \frac{1}{2} A\Big(\vec{W}^*\big(\vec{W}_i, \vec{W}_{i+1}\big)\Big)\big(\vec{W}_i - \vec{W}_{i+1}\big) \tag{4.92}$$

Extension to higher orders The upwind spatial discretization described above allows to have a stable numerical scheme, which is able to capture discontinuities without fluctuations. Nonetheless the original formulation of the Roe scheme has order 1 in space, therefore an extension to a higher order is fundamental. The Van Leers's MUSCL (Monotone Upwind Schemes for Conservation Laws) method allows to extend to the second order an upwind scheme keeping the TVD (Total Variation Diminishing) property.

Numerical properties To avoid fluctuations near discontinuities an effective property is the *monotonicity condition*. If u_i^n is a scalar quantity and $\mathcal{H}$ is the numerical method, as

$$u_i^{n+1} = \mathcal{H}\big(\dots, u_{i-1}^n, u_i^n, u_{i+1}^n, \dots\big) \tag{4.93}$$

$\mathcal{H}$ is monotone if

$$\frac{\partial \mathcal{H}}{\partial u_{i+j}^n} > 0 \qquad \forall j \tag{4.94}$$

But, according to the Godunov theorem: *Linear numerical schemes for solving partial differential equations (PDEs), having the property of not generating new extrema (monotone scheme), can be at most first-order accurate.* Therefore the need of a less restrictive condition rises. The MP (Monotonicity Preserving) property can thus become a good reference condition to evaluate the behavior of a scheme in high gradient zones. In fact it imposes that:

1. no generation of new local extrema;

2. no increase of a local maximum or decrease of a local minimum.

This property can be imposed mathematically by using the Total Variation Diminishing (TVD) condition:

$$TV\left(u^{n+1}\right) \leq TV\left(u^{n}\right) \qquad \text{with} \qquad TV(u) = \sum_{i} \left| u_{i+1} - u_i \right| \tag{4.95}$$

Second order extension The evaluation of the flux in an upwind scheme at the interface $i+1/2$ needs the knowledge of the two states $u^L_{i+1/2}$ and $u^R_{i+1/2}$ at both sides of the interface. The first order method uses the states calculated on the cells i and $i+1$ as $u^L_{i+1/2} \equiv u_i$ and $u^R_{i+1/2} \equiv u_{i+1}$. The extension to the second order by the MUSCL approach is based on the use of extrapolated boundary condition to calculate the interface flux, by considering a linear evolution of the variables u_i and u_{i+1} in the cells i and $i+1$.

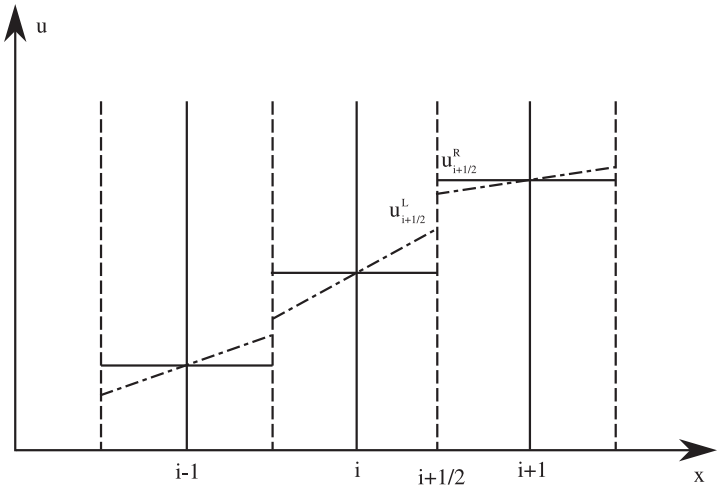

Figure 4.1: MUSCL approach to the boundary conditions of the Riemann problem at interfaces

In particular the slope of the solution in each cell is calculated with respect to the local gradient of the solution in the field, as shown in the relation (4.98). This method provide a second order solution in space, but it involves fluctuation in high gradient zones in fact new extrema occur. Therefore, to keep the TVD condition some slope limiters are necessary.

Thence in our cases, the boundary values of the Riemann problem that is established at each interface are obtained by

$$\vec{W}^L_{i+1/2} = \vec{W}_i + \frac{1}{2}\sigma_i \tag{4.96}$$

$$\vec{W}^R_{i+1/2} = \vec{W}_{i+1} - \frac{1}{2}\sigma_{i+1} \tag{4.97}$$

where W is the conservative variable vector and σ_i is the slope of the linear evolution of W in i^{th} cell. In particular for the present study the *minmod limiter* has been applied. Therefore the slope is calculated by

$$\sigma_i = \phi_{minmod}\big(W_i - W_{i-1}, W_{i+1} - W_i\big) \tag{4.98}$$

Moreover, according to [7] and [8], the slope limiter can be seen as a flux limiter of a *high resolution method*, which rules the combination of a first order upwind scheme and a second order scheme, depending on the local gradient of the solution:

$$\vec{F}^{HR}_{i+1/2} = \vec{F}^L_{i+1/2} + \phi_{i+1/2}\big[\vec{F}^H_{i+1/2} - \vec{F}^L_{i+1/2}\big] \tag{4.99}$$

where the high resolution flux $\vec{F}^{HR}$ is formed by a low order component $\vec{F}^L$ and a high order component $\vec{F}^H$, whose importance is ruled by the limiter ϕ.

The limiter can thus be written as

$$\phi_{minmod}(\theta) = \max\big(0, \min(1, \theta)\big) \qquad \text{with} \qquad \theta_{i+\frac{1}{2}} = \frac{\vec{W}_i - \vec{W}_{i-1}}{\vec{W}_{i+1} - \vec{W}_i} \tag{4.100}$$

and can be represented in the Harten TVD diagram. In the figure 4.2 on the next page the gray region bounds the zone in which the limiter behavior respects the TVD condition and allows a second order scheme if no high gradients occur, while the bold line is the minmod limiter behavior.

Third order extension A more general expression of the right and left state of the Riemann problem at the i^{th} interface is given by Chakravarthy [22]:

$$\vec{W}^L_{i+1/2} = \vec{W}_i + \left(\frac{1+\Psi}{4}\overline{\Delta}_{i+1/2} + \frac{1-\Psi}{4}\overline{\overline{\Delta}}_{i-1/2}\right) \tag{4.101}$$

$$\vec{W}^R_{i+1/2} = \vec{W}_{i+1} - \left(\frac{1-\Psi}{4}\overline{\overline{\Delta}}_{i+3/2} + \frac{1+\Psi}{4}\overline{\Delta}_{i+1/2}\right) \tag{4.102}$$

where Ψ is the "precision factor" and for the first equation, introducing $\Delta\vec{W}_{i+1/2} = \vec{W}_{i+1} - \vec{W}_i$, the limiters are specified by

$$\overline{\Delta}_{i+1/2} = \phi\big(\Delta W_{i+1/2}\,,\, \omega\Delta W_{i-1/2}\big) \tag{4.103}$$

$$\overline{\overline{\Delta}}_{i-1/2} = \phi\big(\Delta W_{i-1/2}\,,\, \omega\Delta W_{i+1/2}\big) \tag{4.104}$$

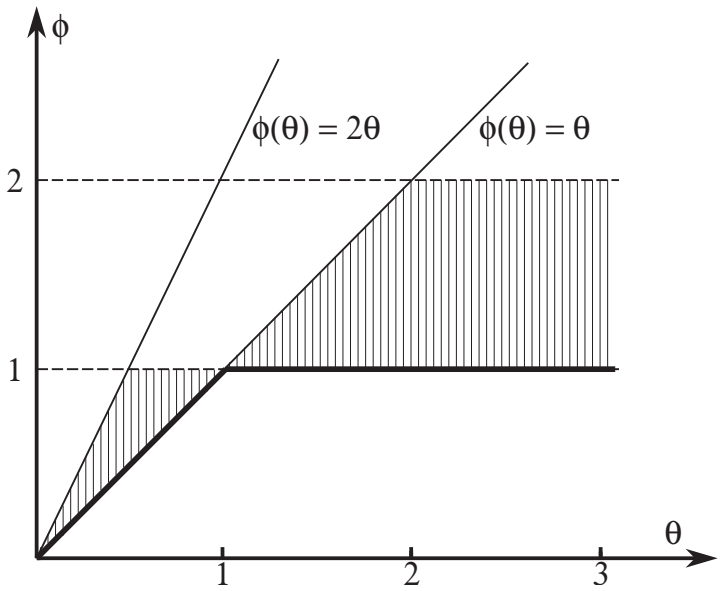

Figure 4.2: Region on which the limiter function $\phi(\theta)$ must lie in order to give second order TVD methods

in which ϕ is the slope limiter function and ω is the "compression factor".

Thence this scheme has three degree of freedom: Ψ, ϕ, ω. Different combinations of their values can provide various schemes, for example with $\Psi = -1$ and $\omega = 1$ the second order extension shown above is obtained. In particular $\Psi = 1/3$ provides a third order upwind scheme. The version implemented in *elsA* of this scheme does not use any limiter, which can explain the remarkable differences that often occur between the second and the third order extension.

Finally the compression factor can control the numerical dissipation, taking different values in the range

$$1 \leq \omega \geq \frac{3-\Psi}{1-\Psi} \tag{4.105}$$

where a low ω value means a high dissipation. But in *elsA* it is fixed to 1.

4.4.2 Viscous Fluxes

Viscous fluxes are calculated separately from convection fluxes treated above, using a second order central scheme. The details of this method are not treated in the present work, therefore for further information the *elsA* theoretical manual may be a help [19]. In order to calculate the viscous fluxes the gradient of velocity, temperature and turbulence field have to be known. They are obtained at the center of each cell applying the flux-divergence theorem (or theorem of Green-Ostrogradsky) to a shifted control volume. For example for the scalar quantity ϕ the following relation is verified:

$$\left(\vec{\nabla}\phi\right)_S = \frac{1}{V_S}\int_{V_S} \vec{\nabla}\phi \mathrm{d}V = \frac{1}{V_S}\int_{\partial S} \phi\vec{n}\mathrm{d}S \tag{4.106}$$

where V_S is the shifted control volume, ∂S is its boundary and $\left(\vec{\nabla}\phi\right)_S$ is gradient of ϕ evaluated at the center of V_S as the averaged of its real value inside the volume.

4.5 Time integration methods

After the space discretization an ordinary differential equation in the form (4.70) is obtained:

$$\frac{\mathrm{d}W}{\mathrm{d}t} = -\frac{1}{\Omega}R \tag{4.107}$$

where R is the modeled residual, which contains the contributions of the convective flux, the diffusive flux and the source term. Therefore the time integration is not coupled with the space discretization, which guarantees that a steady solution will not be affected by any time integration method or by a time step value [20].

4.5.1 Explicit Time Integration

Explicit time integration is applied rather to *fast unsteady* problems, involving "high frequency" phenomena and not allowing the use of large time steps. For *slow unsteady* problems, in fact, the numerical cost of the temporal cycle is strongly reduced by the use of implicit methods of integration in time, increasing the numerical field of stability of the schemes and thus allowing the use of large time steps.

Runge-Kutta Scheme

The basic idea of the Runge-Kutta time integration method is the evaluation of the solution in several intermediate instants between n and $n+1$ [19]. In this way the numerical time step is further divided to have a higher precision order and a better stability. A formulation of the method with m steps to advance the numerical solution from the time step $t^n = n\Delta t$ to the time step $t^{n+1} = t^n + \Delta t$ is

$$\begin{aligned}
&W^0 = W^n \\
&W^{(1)} = W^{(0)} - \alpha_1 \frac{\Delta t}{\Omega} R(W^{(0)}) \\
&\vdots \\
&W^{(k)} = W^{(0)} - \alpha_k \frac{\Delta t}{\Omega} R(W^{(k-1)}) \\
&\vdots \\
&W^{(n+1)} = W^{(m)}
\end{aligned} \tag{4.108}$$

Hirsch has proved that this scheme has order k when applied to the classic linear hyperbolic equation $\partial u/\partial t + a\partial u/\partial x = 0$ [20]. But it falls to order 2 in the case of a non-linear equation.

During the present study some simulations used the *Backward Euler Scheme*, which is the one-step application of the Runge-Kutta Scheme. This allowed to strongly reduce the time of calculation but with a lower precision order with respect to an implicit method. The comparison

between the two approach is presented in chapter 5. Moreover it is worth to remind that for an approximation in space of the type "simple centered" of the convective flux, i.e. obtained by arithmetic mean of the flux densities taken at the center of the two cells adjacent to the considered face, the retrograde Euler scheme is *unconditionally unstable*. Several Runge-Kutta steps ($m > 1$)are thus necessary. For an "upstream" approximation of the convective flux, the Backward Euler Scheme is *stable* under certain linear stability conditions on the time step Δt. Nonetheless these considerations are strictly verified for schemes without artificial viscosity and where no real viscous phenomena are taken into account. In fact the presence of viscosity, both artificial and real, adds a stabilizing effect to the scheme. That is the reason that allowed some of the simulations presented in the following chapters to be performed.

4.5.2 Implicit Time Integration

The step Δt^n can be specified by using the relation (4.70) discretized with respect to time considering a linear evolution of the unknown W between t^n and $t^n + 1$

$$\Omega \frac{\Delta W^n}{\Delta t} = -(R^{n+1} - R^n) \tag{4.109}$$

where $\Delta W^n = W^{n+1} - W^n$. This can finally be combined with the previous step relation, applying some coefficients that allow to assign different weights to the various terms, according to [21]

$$(1+\xi)\frac{\Omega \Delta W^n}{\Delta t^n} - \xi \frac{\Omega \Delta W^{n-1}}{\Delta t^{n-1}} = -\Big(\theta R^{n+1} + (1 - \theta + \phi)R^n - \phi R^{n-1}\Big) \tag{4.110}$$

In particular the coefficients define a family of explicit schemes($\theta = 0$) or implicit schemes ($\theta \neq 0$).

The equation (4.110) can be solved by using some *Linear Multi-Step* methods. In these techniques the temporal variation of a quantity is reconstructed starting from a linear combination of the values taken by this quantity in different time instants. The methods implemented in *elsA* use the two instant $n - 1$ and n to calculate an initial solution at $n + 1$, then an iterative method is applied keeping frozen the physical time. Therefore two cycles are actually executed. The "external" one is the physical time progress, for which each step is the time step previously fixed, while the "internal" cycle is a steady iteration process needed to properly solve the equation (4.110).

This principle is clearly understandable thinking about a simple signal, where one variable depends on time, for example $W = W(t)$. In this case the first iteration of the (4.110) solution provides the initial value $\widetilde{W}^{n+1}$ for the variable at the time t^{n+1}, using the known points $W^n(t^n)$ and $W^{n-1}(t^{n-1})$. Subsequently the steady iteration process provides W^{n+1} with a fixed precision.

Principally two methods are available to applied this technique: *Gear Approach* and *Dual Time Stepping*. While they are exactly similar when iterative processes are converged, there is no guarantee that their behavior are comparable when the iterative process is severely curtailed, or that their computational costs are similar.

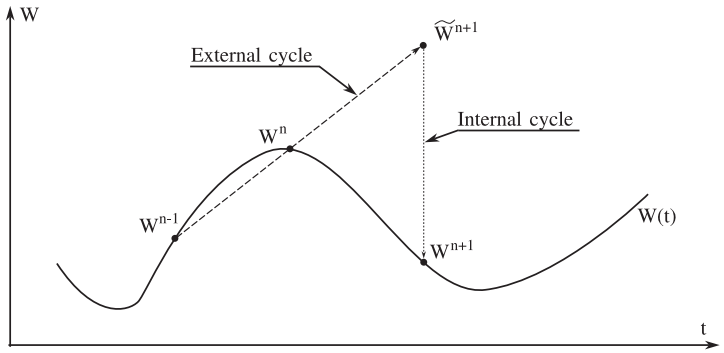

Figure 4.3: Time integration principle of second-order DTS and Gear approaches

Gear Approach

The Gear Approach, or Newton Approach, is based on a Newton iterative method to reset to zero the "unsteady" residual that occurs at each step of the time increase. In fact the system

$$\mathcal{L}(W^{n+1}) = (1+\xi)\frac{\Delta W^n}{\Delta t^n}\Omega - \xi\frac{\Delta W^{n-1}}{\Delta t^{n-1}}\Omega + \theta R^{n+1} + (1-\theta+\phi)R^n - \phi R^{n-1} = 0 \quad (4.111)$$

with $\Delta W^n = W^{n+1} - W^n$ and $\Delta W^{n-1} = W^n - W^{n-1}$, have to be solved at each time step. Thence the algorithm performed by the Gear Method in the internal iterative process is

$$\left.\frac{\partial \mathcal{L}(W^{n+1})}{\partial W^{n+1}}\right|^{\nu}(W^{n+1,\nu+1} - W^{n+1,\nu}) = -\mathcal{L}(W^{n+1,\nu}) \quad \Rightarrow \quad W^{n+1,\nu+1} = W^{n+1,\nu} - \frac{\mathcal{L}(W^{n+1,\nu})}{\left.\frac{\partial \mathcal{L}(W^{n+1})}{\partial W^{n+1}}\right|^{\nu}}$$

$$\Rightarrow \qquad W^{n+1,\nu+1} = W^{n+1,\nu} - \mathcal{L}(W^{n+1,\nu})\left((1+\xi)\frac{\Omega}{\Delta t^n}I + \theta\left.\frac{\partial R}{\partial W}\right|^{n+1,\nu}\right)^{-1} \quad (4.112)$$

where ν represents a generic iteration.

In particular, the gear method that is implemented in elsA uses the parameters shown in the following table:

θ	1
ξ	0.5
ϕ	0

Dual Time Stepping

The Dual Time Stepping (DTS) method is based on an internal time step $\Delta\tau$, used to reach a steady state of the unknown W^{n+1} for each physical time instant t^{n+1}. Therefore the convergence condition is a constant value of W^{n+1} in the considered volume Ω, with respect to the "Dual Time" τ. This condition can be found by applying an iterative system solver to

$$\Omega \frac{\mathrm{d}W^{n+1}}{\mathrm{d}\tau} + \mathcal{L}(W^{n+1}) = 0 \tag{4.113}$$

Still with

$$\mathcal{L}(W^{n+1}) = (1+\xi)\frac{\Delta W^n}{\Delta t^n}\Omega - \xi\frac{\Delta W^{n-1}}{\Delta t^{n-1}}\Omega + \theta R^{n+1} + (1-\theta+\phi)R^n - \phi R^{n-1} \tag{4.114}$$

The evolution of the unsteady residual with respect to the internal time can be linearized from the iteration ν to the following $\nu+1$, which corresponds to the time increase $\Delta\tau$

$$\mathcal{L}(W^{n+1,\nu+1}) = \mathcal{L}(W^{n+1,\nu}) + \frac{\partial \mathcal{L}}{\partial \tau}\Big|^{\nu} \Delta\tau + O(\Delta\tau) \tag{4.115}$$

where the residual derivative can be written as

$$\frac{\partial \mathcal{L}}{\partial \tau}\Big|^{\nu} \Delta\tau = \frac{\partial \mathcal{L}}{\partial W}\Big|^{\nu} \frac{\partial W}{\partial \tau}\Delta\tau \simeq \frac{\partial \mathcal{L}}{\partial W}\Big|^{\nu} \Delta W \tag{4.116}$$

Therefore the algorithm of the internal solution is

$$\left(\frac{\Omega}{\Delta\tau} I + \frac{\partial \mathcal{L}(W^{n+1})}{\partial W^{n+1}}\Big|^{\nu}\right)(W^{n+1,\nu+1} - W^{n+1,\nu}) = -\mathcal{L}(W^{n+1,\nu})$$

$$\Rightarrow \qquad W^{n+1,\nu+1} = W^{n+1,\nu} - \mathcal{L}(W^{n+1,\nu})\left(\frac{\Omega}{\Delta\tau} I + (1+\xi)\frac{\Omega}{\Delta t^n} I + \theta \frac{\partial R}{\partial W}\Big|^{n+1,\nu}\right)^{-1} \tag{4.117}$$

The relation shows that the DTS methods is strictly equivalent to the gear approach if $\Delta\tau \to 0$. Otherwise the internal time step calculated by imposing a CFL factor will determine the differences between the two approaches, which are shown in the chapter 5.

4.6 Multi-grid acceleration method

Traditional iterative methods work by approaching the solution to the converged state at each iteration. The reduction of the error during this process is actually related to some mesh characteristics. In particular, by defining the frequency of the error components with respect to the grid step dimensions, it can be observed that high frequencies are deadened much more quickly than low frequencies. Based on this consideration, the idea of the multi-grid technique is to progressively reduce the mesh size, which means increasing the cell dimensions, in order to smooth the error components that have a low frequency on the fine grid but become high frequencies on the coarse grid. Therefore each multi-grid iteration is composed of some different grid steps, which make the iteration more expensive with respect to a simple-grid iteration, but also much more effective.

Therefore the multi-grid technique performed a correction of the solution on the fine grid by using the values obtained on various levels of coarse grids, as shown in figure 4.4 on the following page.

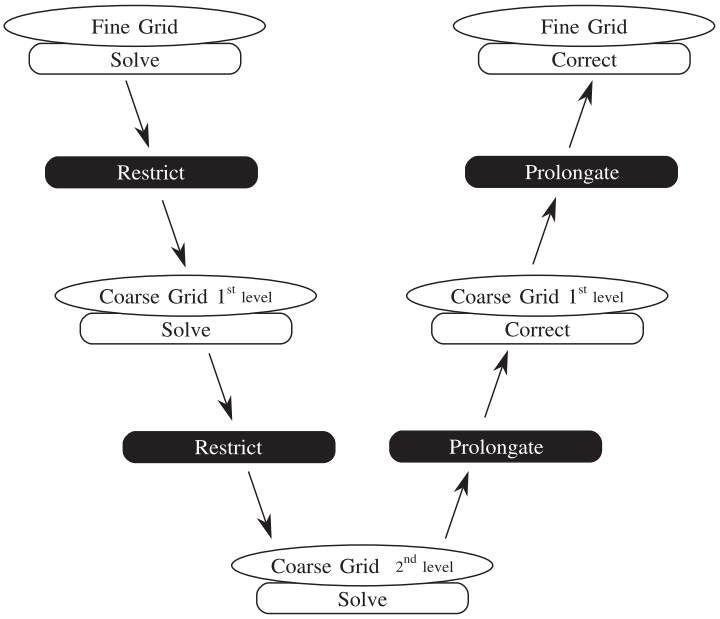

Figure 4.4: 3-steps V-cycle of the multi-grid technique

The correction strategy applied in the steady simulations described in the present report is the *V-cycle* on three levels. The triple-grid cycle is initialized by a solution calculated by one or more iterations on the finest grid. This solution and the residual are then restricted and transferred to the next level of coarsening grid to initialize a second step of calculation during which one or more iterations are carried out. These stages form the phase called downward. The ascending phase starts with the calculation of the correction on the coarsest grid, i.e. of the difference between the new solution and the initial solution on this grid. This correction is subsequently prolonged on the previous-level grid (the solution of the coarse grid is not transferred on the fine grid). Finally the solution previously calculated on the fine level is corrected.

The effects of the triple-grid V-cycle applied during the present study are shown in the chapter 5.

4.7 CROR splitting algorithm

Since the conception step of elsA, the code has been thought to run in parallel mode. This means to allocate the topological blocks of the grid to different processors, which can perform the calculation at the same time working on a portion of the domain. This allows a very important reduction of the calculation time, even if the information exchange among the processors slows each single-processor computation. Therefore in a parallel configuration, each calculation unit is loaded with a number of cells, that determines the time needed by the processor to perform an iteration. This means that the more loaded unit will be the slowest and the others have to wait for it. In order to limit this effect a good load balance among the units has to be achieved by splitting the blocks and allocating them to obtain an effective configuration. ElsA disposes of an adapted splitting and balancing tool that is able to realize this operation.

One of the major problems risen with the elsA version that has been used, was the limit

imposed by the presence of the rows interaction plane to the parallel computation. In fact the particular operations performed on the information transmitted between the two side of the interaction plane (see chapter 2), was not coded to work if the blocks were allocated to different processors. This involves the need to have the topological blocks next to the interaction plane associated to the same calculation unit, preventing the elsA splitting algorithm to be directly applied.

To solve this problem a new balancing algorithm has been coded in order to satisfy the requirements imposed by the CROR configuration that has been studied. The operations performed by the new code are showed in the figure 4.5.

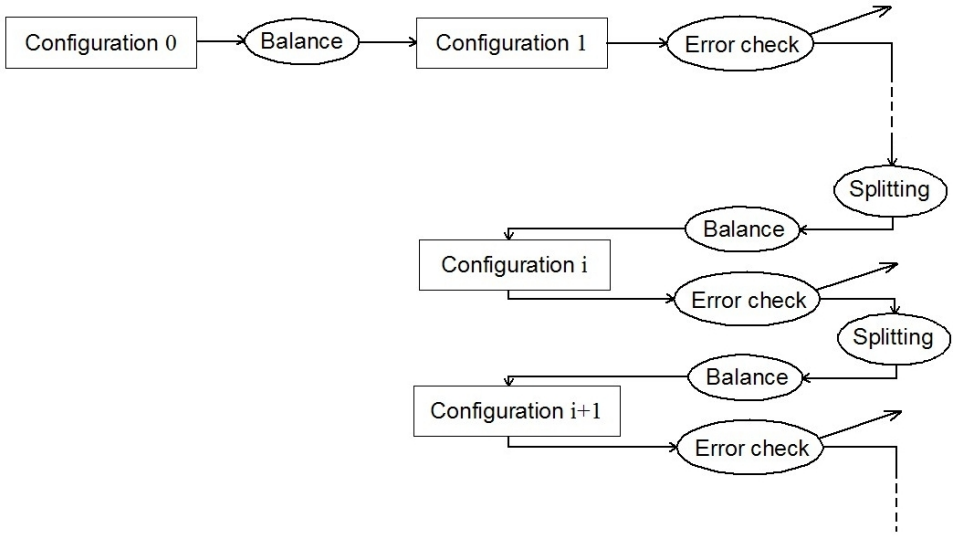

Figure 4.5: Splitting and balancing algorithm

At every iteration the ten biggest blocks are divided in a point and a direction chosen to maintain at least three multi-grid levels. After the splitting the balancing process is performed, during which the blocks next to the interaction plane are considered as a single block, in order to keep them on the same processor. Subsequently the balance error is calculated by comparing the maximum obtained load with the optimum one, which corresponds to the total number of cells divided by the number of processors. If this is less than an imposed error limit the algorithm will stop.

4.7.1 Balancing process

The balancing process is composed by two steps, during which the the blocks next to the interaction plane are considered as a single block. The first performs an initial distribution of the blocks among the calculation units, while the second will modify this distribution reaching the best balance.

Step 1 First of all a list of the blocks is realized by ordering them in relation to their dimension. Subsequently one block is allocated to each processor, starting from the biggest block. When this operation is finished it is performed a second time by scrolling the processors in the

inverse order. This is repeated until all the blocks are allocated. In this way a quite equilibrated configuration is reached(see figure 4.6).

Step 2 A second step is necessary to reach the best configuration possible with the available blocks. The dimension of the smallest block allocated in the most loaded processor is compared with the load difference between this processor and the less loaded one. If the dimension of the block is lower than the load difference, the block is allocated to the less loaded processor (see figure 4.6).

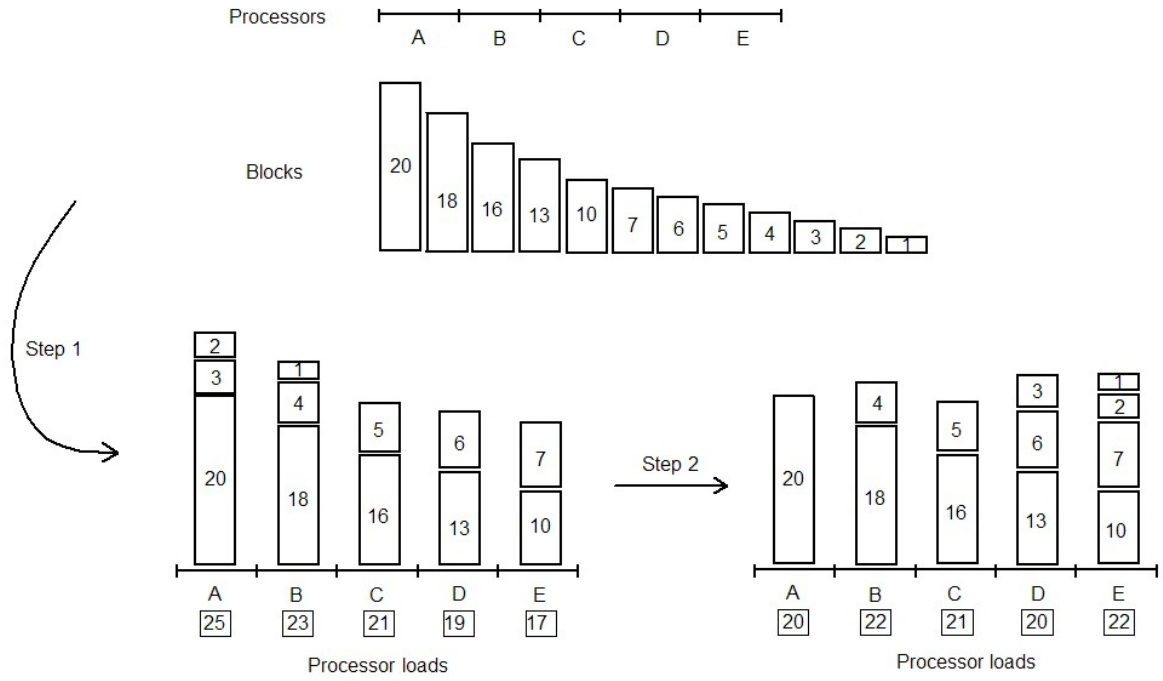

Figure 4.6: Example of the balancing process steps

Chapter 5

Verification of the solutions

Contents

5.1 Introduction

In the present chapter the numerical errors involved by the solution of the equations are evaluated. The quality of the simulation results, with respect to the Navier Stokes solution, depends on several factors, which typically have also a strong influence on the computational cost. Therefore the purpose of this chapter is to define a relation between the result accuracy and the required calculation time, in order to provide a practical help in the realization of future CROR analysis.

First of all, the evolution of the solution during the calculation needs to be monitored in order to be able to stop the process when no more quality variations are expected. Thence, the first section will describe the technique that has been developed to accomplish this operation. Subsequently, the time and space discretization, as well as the numerical methods and turbulence models, play a key role in the solution of the equations. Thus, section 5.3 is dedicated

to the presentation of the techniques that have been used to evaluate the errors involved by the discretization, and to compare the numerical schemes and turbulence models that have been applied. The results of these analysis are then presented in the last three sections, always in relation to the computational cost that each method involves. For this last issue the converged conditions are identified for the time and space discretization, and a technique of solution convergence acceleration is described and evaluated for a steady calculation.

5.2 Convergence Criteria

The monitoring of the iterative process evolution is a fundamental element of the calculation. In fact it allows to control the correct progression of the solution and to set the point after which the results can be considered no longer dependent from further iterations. Therefore a good method to quickly evaluate the quality of the results without the need of stopping the process and performing time expensive post-processing operations is needed.

5.2.1 Residual calculation

As shown in the chapter 4, taking into consideration the Navier Stokes equation system the following terms can be identified:

- $\vec{W}(M,t)$: the vector of the conservative unknowns, defined in any point M of the flow, for any time instant $t > 0$;
- $\vec{CF}$: the density of the convective flux;
- $\vec{Fd}$: the density of the diffusive flux;
- $\vec{Q}$: the source term;

They allow to express the conservation laws for the i^{th} cell, of volume Ω_i and surface Σ_i composed by the 6 sides $\Sigma_{i,j}$, in the form

$$\frac{\mathrm{d}}{\mathrm{d}t}\int_{\Omega_i}\vec{W}\mathrm{d}\Omega + \oint_{\Sigma_i}\left(\vec{CF}+\vec{Fd}\right)\cdot\vec{n}\mathrm{d}\Sigma = \int_{\Omega_i}\vec{Q}\mathrm{d}\Omega \tag{5.1}$$

After the discretization in space by a method of finite volumes, these conservation laws are written in the semi-discrete form, as the equation (4.70):

$$\frac{\mathrm{d}}{\mathrm{d}t}\left(\Omega_i\overline{\vec{W}}_i\right) + \sum_{j=1}^{6}\left(\overline{\vec{F}}\right)_{\Sigma_{i,j}}\cdot\Delta\vec{S}_j - \Omega_i\overline{\vec{Q}}_i = 0 \tag{5.2}$$

with

$$\overline{\vec{W}}_i = \frac{1}{\Omega_i}\int_{\Omega_i}\vec{W}\mathrm{d}\Omega \tag{5.3}$$

and the other averaged quantities defined in the same way. The relation (5.2) can also be expressed as

$$\frac{\mathrm{d}}{\mathrm{d}t}\left(\Omega_i\overline{\vec{W}}_i\right) + \overline{\vec{R}}_i = 0 \tag{5.4}$$

where $\overline{\vec{R}}_i$ indicates the residual:

$$\overline{\vec{R}}_i = \sum_{j=1}^{6} \left(\overline{\vec{F}}\right)_{\Sigma_{i,j}} \cdot \Delta\vec{S}_j - \Omega_i \overline{\vec{Q}}_i \tag{5.5}$$

Therefore, in the case of a steady flow, the converged solution is obtained when, for t sufficiently large, one has:

$$\left| \frac{\mathrm{d}}{\mathrm{d}t}\left(\Omega_i \overline{\vec{W}}_i\right) \right| = \left| \overline{\vec{R}}_i \right| < \epsilon \tag{5.6}$$

Finally the residual is written as

$$\overline{\vec{R}}_i = -\frac{\Delta\left(\Omega_i \overline{\vec{W}}_i\right)}{\Delta t} \tag{5.7}$$

In practice the residual in norm L^2, for the l^{th} component W^l of the conservative variables vector, is calculated on the following way, without taking account of possible variations of volume:

$$Res_{exp}^{(n+1)}\left(W^l\right) = \left[\frac{1}{N} \sum_{k=1}^{N} \left(\frac{W_k^{l,n+1} - W_k^{l,n}}{\Delta t} \right)^2 \right]^{\frac{1}{2}} \tag{5.8}$$

where Δt represents the local time step fixed by the definition of the CFL parameter and N the number of volumes of control, i.e. the number of grid cells.

5.2.2 Mixing plane approach monitoring

In the case of the steady mixing plane approach, the convergence condition is obtained when the variations of the solution of the equation at each iteration are sufficiently low. This allows to base the control of the result evolution on the residual calculation at each iteration.

Moreover, the solution progressing from the initial imposed condition can be evaluated by observing the orders of magnitude lost by the residuals. In the present study the convergence has been considered established if the following criteria were satisfied:

- loss of at least 3 order of magnitude of the residuals starting the calculation from a uniform flow condition imposed everywhere in the field;
- stabilized trend of the residuals for at least 1000 iterations.

The following graphs show the trend of the residuals during a mixing plane calculation performed by using the Jameson numerical scheme associated with the k-ω turbulence model and applying a 2 levels multi-grid acceleration (only 1 coarse grid). The seven images correspond to the five conservative variables of the averaged Navier Stokes system plus the two unknowns of the turbulence model.

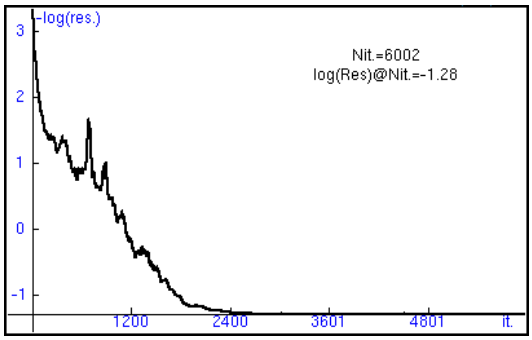

(a) Residual of ρ

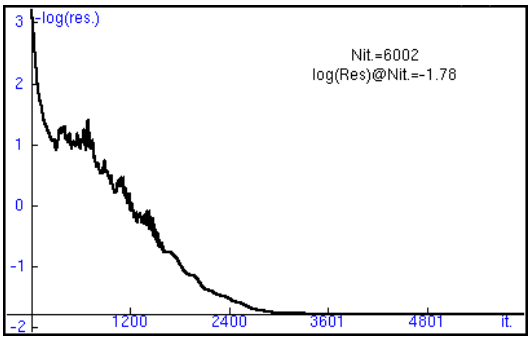

(b) Residual of ρu

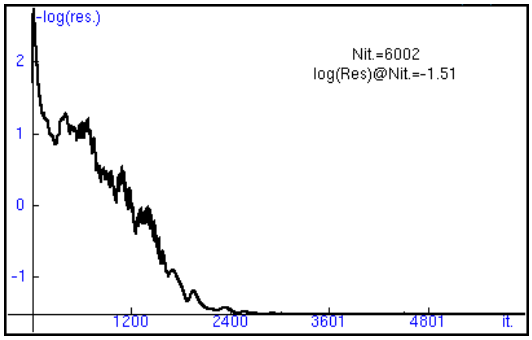

(c) Residual of ρv

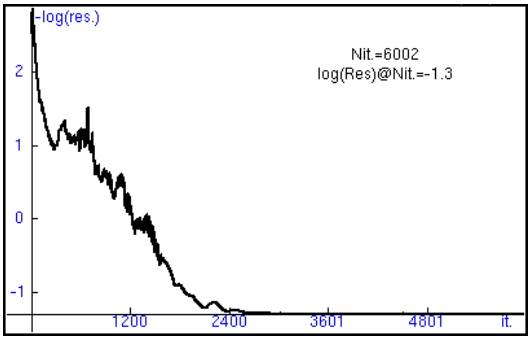

(d) Residual of ρw

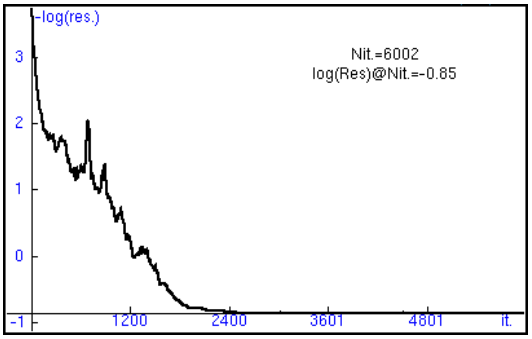

(e) Residual of ρe

Figure 5.1: Conservative variables residuals

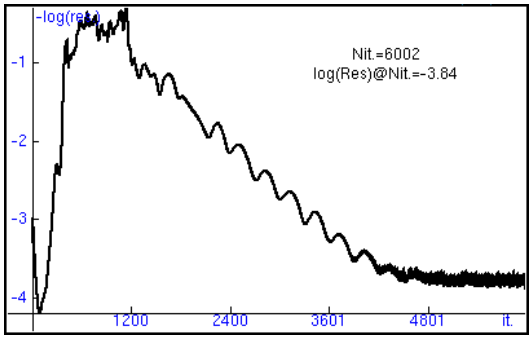

(a) Residual of ρk

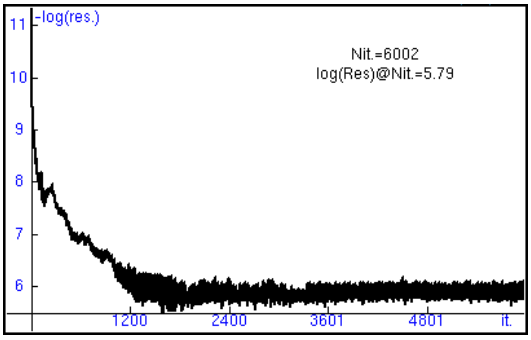

(b) Residual of $\rho\omega$

Figure 5.2: Turbulent variables residuals

5.2.3 Chorochronic approach monitoring

For an unsteady calculation the evaluation of the convergence becomes a little more complicated. In fact the equation solutions always present some variation between an iteration and the following one. This is due to the evolution of the physical time that involves a variation in the geometry of the numerical field. In fact a periodic trend can be appreciated in the residual graph, as shown by figure 5.4 on page 71.

As one can observe from the equation (5.8), the drawn residual values are a sort of average of the cell residuals over the whole domain. Thence a kind of spatial filter is actually applied to the solution variation that has to be monitored. In particular, for an unsteady calculation the convergence criterion is focused to the periodicity of the results evolution, therefore its characteristics are very important. In order to avoid the filtering effect of the residuals, some total pressure and total temperature probes have been placed in the field. This allows to capture the values of these physical quantities at every iteration. The probes are constituted by cells from which periodic extractions are performed. In particular each probe is formed by a strip of cells, as shown in figure 5.3, whose values are spatially averaged to obtain a single value which represents a sample of the physical quantity evolution that occurs in the probe region. Subsequently a Fourier analysis allows to assess the characteristics of this time-dependent signals to finally set up some convergence criteria.

In the case presented in this report, the changing of the geometry is modeled by time-dependent boundary conditions, as described in chapter 2. This means different interactions between the two portions of the domain, associated to a blade of each rotor. The period of the relative motion depends on the revolution speed and blade number of each row. Therefore the unsteadiness of each rotor sub-domain has a specific frequency, as can be noticed in figure 5.5.

The position of the probes has been chosen in order to capture the disturbances due to the relative motion between the rows and also the interaction between the wakes of each rotor blades. Moreover, their shape is determined to extend the probes on the whole span dimension of the region of interest.

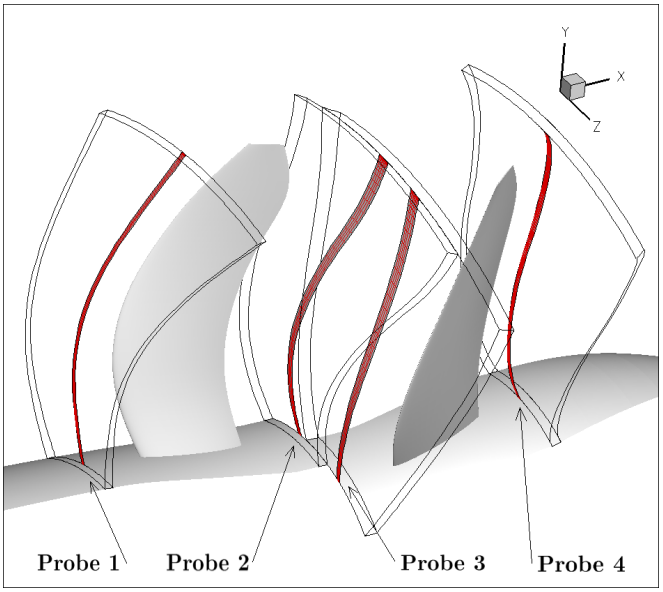

Figure 5.3: Grid cells used as probes, with the topology blocks they are part of

The calculation figures 5.4 to 5.6 are referred to, has been performed by applying the second-order Roe numerical scheme, associated to the $k-\omega$ turbulence model and a time step based on $Nq0 = 150$, which means 1650 iterations for each front row period and 1350 for each rear row period[1].

Referring to the figures 5.3 and 5.5:

Probe 1 It detects a signal composed by weak fluctuations characterized by a period of $|\Omega_1 - \Omega_2|2\pi/Z_2$, which corresponds to 1650 iterations. This is due to the influence of the potential field of the downstream rotor on the flow around the upstream row blades.

Probe 2 It is still placed in the upstream channel, on the interaction plane just out of the wake of the front row, from which it captures only the potential field as a constant signal. It also detects as a periodic signal the potential effects of the rear rotor, with a period of $|\Omega_1 - \Omega_2|2\pi/Z_2$.

Probe 3 It is placed on the same plane as the second probe, but it belongs to the downstream channel domain. It captures the potential field of the rear row as a constant value, but also the potential and the wake effects of the front rotor, with the period $|\Omega_1 - \Omega_2|2\pi/Z_1$, corresponding to 1350 iterations.

Probe 4 It is placed inside the wake of the rear rotor, which explains the loss of energy with respect to the values detected by the other probes. Nonetheless the effects of the front row are still visible as a $|\Omega_1 - \Omega_2|2\pi/Z_1$ period wave, which is not as clean as the signal of the probe 3 because of the two wakes interaction. Therefore, the signal of the probe 4 is the slowest in satisfying the convergence criteria, since it is composed by a higher number of harmonics (fig. 5.5).

The Fourier analysis performed on the detected signals allow to evaluate the following characteristics, shown in figure 5.6:

- the average value of the signal;
- the signal energy calculated on 3.5 periods and the difference between every calculation step;
- the power spectral density of the signal considering an arbitrary number of harmonics.

By using these information the converged state is considered established if the variation of the signal energy between two consecutive 3.5 periods steps is less then 10^{-2}, while the power spectral density shows a stabilized trend composed by horizontal strips.

Figure 5.4 shows the residual associated to the first conservative variable, the density. As one can notice from this figure, the loss of order of magnitude is much less then in the case of a mixing plane calculation (figure 5.1a on page 68). That is due to the initial condition of the chorochronic calculation, that is actually a converged mixing plane solution, thence the

[1] The number of iterations corresponding to a blade passing period is calculated by dividing it by the time step:

$$\frac{|\Omega_1 - \Omega_2|2\pi}{Z_2} \quad \frac{Z_2 Z_1 Nq0}{|\Omega_1 - \Omega_2|2\pi} = Z_1\, Nq0 \quad \text{for the front row period} \tag{5.9}$$

where $Z_1 = 11$, $Z_2 = 9$ and, in this calculations, $Nq0 = 150$

averaged variation of physical quantities is lower than in the steady case which start from a constant field.

Moreover, by comparing figure 5.4 and 5.6b, one can observe that the information given by the residual during the calculation is not sufficient to evaluate the evolution of the solution. In fact a periodic trend seems to be established in the residual trend much before the satisfaction of the criterion on the signal energy variation.

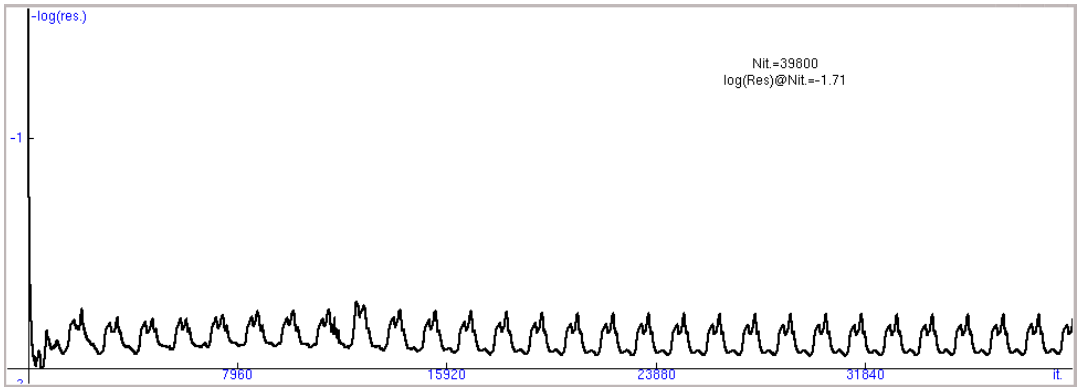

Figure 5.4: Density residual for a chorochronic calculation

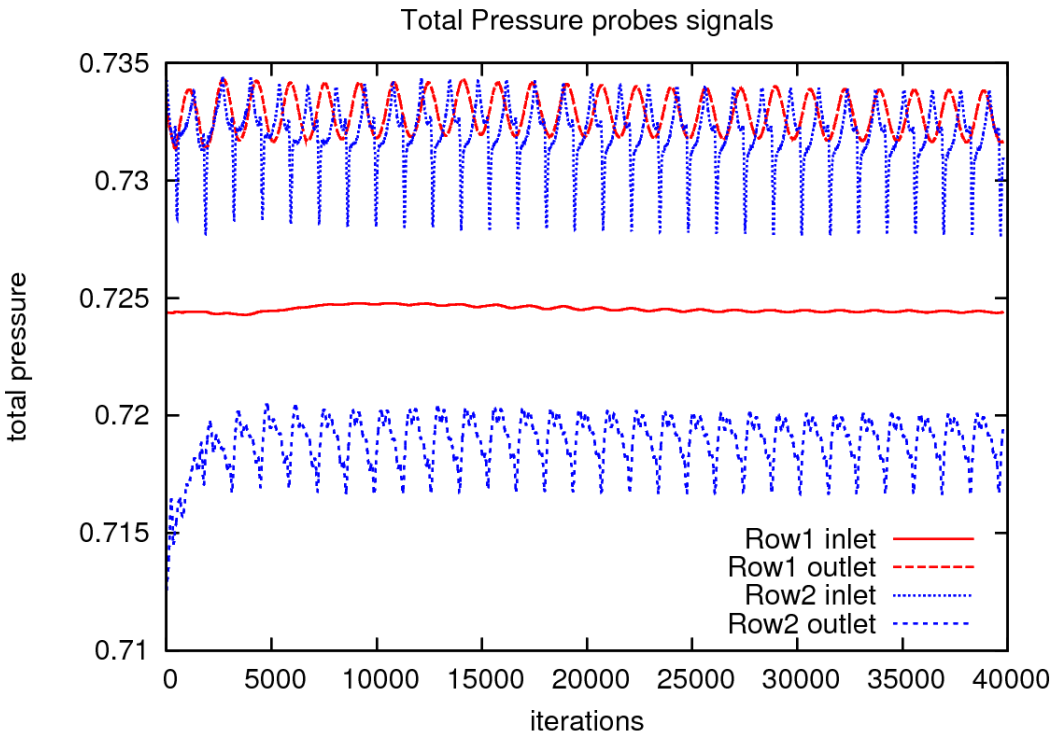

Figure 5.5: Total pressure detected by the four probes during the calculation

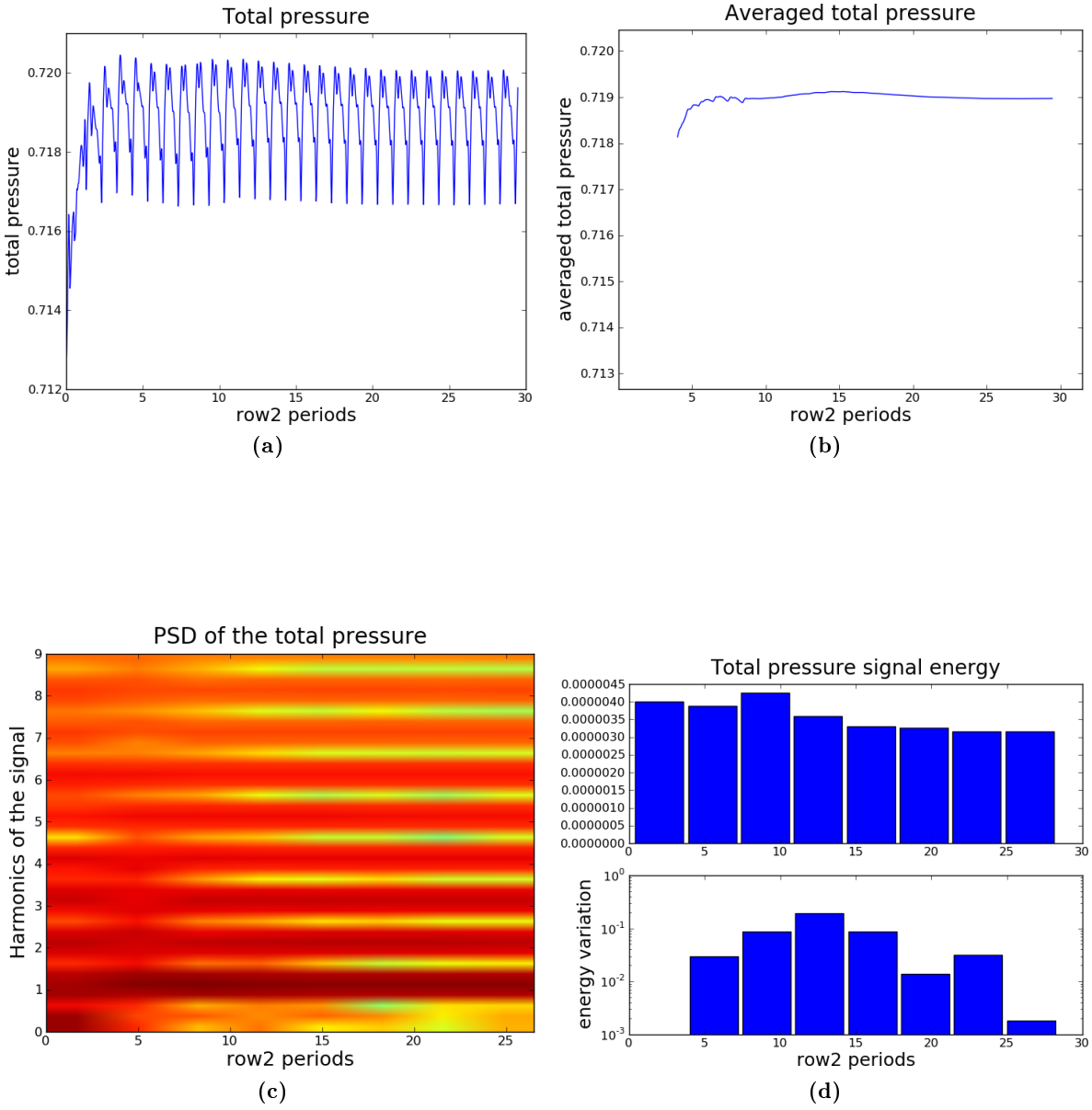

Figure 5.6: Total pressure signals detected by the probe 4: rear row outlet

5.3 Analysis techniques

5.3.1 Performance calculation method

In this section a method for the thrust calculation of the propellers system is presented. The most important limit of this technique is come to light for the calculation of the torque, as explained at the end of this section. Therefore it has not been possible to obtain the efficiency of the studied configuration. Anyway the integral method that has been applied provides a global quantity, the thrust, useful to analyze the different numerical schemes, turbulence models and spatial discretization characteristics.

Principle of the technique

The calculation of the flow energy increase through the rotors has been based on an integral approach. The whole system has been included in the control volume shown in figure 5.7, by defining two surfaces normal to the main flow direction x. Subsequently the flow of the axial component of momentum has been calculated by integration over each plane. This allows to impose the equilibrium of the control volume. In fact the net flow of momentum through the volume will be equivalent to the resultant of the external forces applied on the volume boundaries. In particular this force is composed by the pressure acting on the upper and x-normal planes, and a component applied by the blades and the spinner walls. Moreover it has been verified that the upper boundaries of the volumes are sufficiently far from the propellers to be parallel to the local flow direction. Therefore there is no mass flow through them, and the pressure on these surfaces cannot have any effect on the longitudinal and azimuthal equilibrium.

The limits of the volume need to be set taking into consideration the whole zone of influence of the propellers. According to the *Disk Actuator Theory*, the effect of the propeller is already present in a wide upstream region. This makes fundamental the position of the front surface, in fact its momentum flow will be subtracted from the momentum that leaves the control volume, to obtain the net flow. Therefore the upstream surface must be placed where the undisturbed conditions occur, otherwise a fraction of the energy added to the fluid by the propeller would not be considered.

The downstream surface position is based on different considerations, in fact, in the case of a single propeller it could be placed immediately after the disk, being able to capture the entire flow of axial momentum. Nevertheless, in the case of two contra-rotating propellers a more complicated phenomenon has to be considered. The purpose of the second rotor is to add to the flow an azimuthal component of momentum opposite to the component due to the first rotor. Nonetheless the effect of a blade on the fluid is local. In other words a certain space is needed for the downwash due to every blades, working as a wing, to form an uniform wake. This is fundamental in the present application because it means that immediately after the two propellers opposite azimuthal components of momentum are still balancing themselves, increasing the axial momentum component, which gives thrust.

$$\int_{S_2} \Big(\rho(A,x_2)u_i^2(A,x_2)\Big)\mathrm{d}A - \int_{S_1} \Big(\rho(A,x_1)u_i^2(A,x_1)\Big)\mathrm{d}A + F_i = 0 \tag{5.10}$$

Where: F_i is the i^{th} component of the resultant force applied to the control volume surfaces,

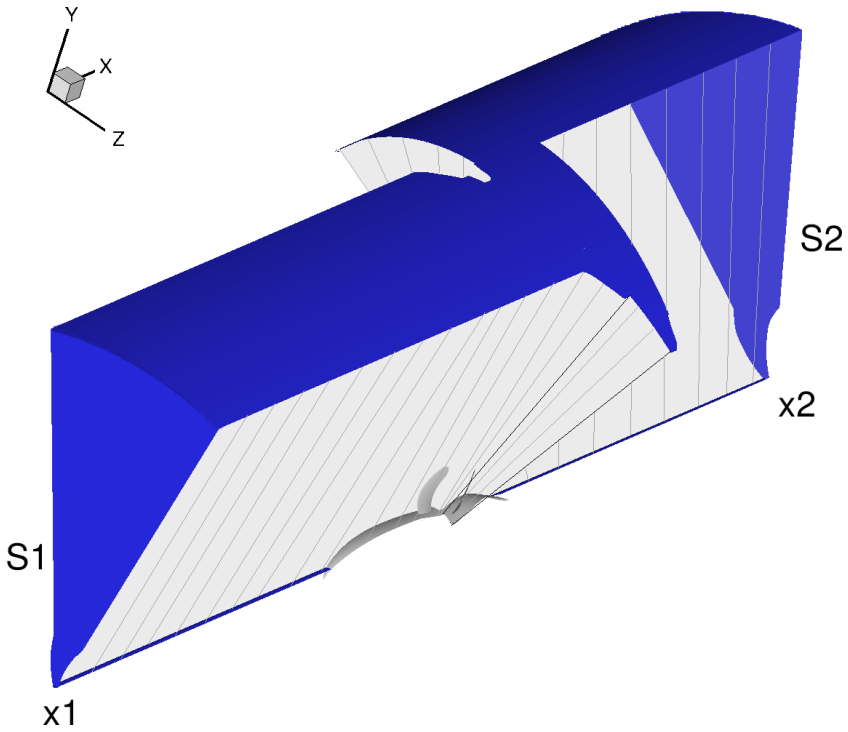

Figure 5.7: The control volume for the calculation of performances

A is an infinitesimal element of surface, S_1 and S_2 are the surfaces at constant x_1 and x_2, and u_i is the i^{th} component of the velocity vector.

Thrust calculation

The calculation of the thrust T is performed by considering the flow of the x-component of momentum through the volume and the pressure on its sides. This is actually the balance of dynalpy, as shown by the following equation. In fact the applied force F_i, in the x direction, is composed by the resultant of the pressures on S_1 and S_2, and a force contrary to the thrust applied by the blades to the air flow.

According to the figure 5.7, let T be the force applied by the fluid on the blades, and u the x-component of the velocity. Therefore

$$\begin{aligned} \Rightarrow \qquad T = &\int_0^{r_{max}} \int_0^{2\pi} \Big(P(\theta, r, x_2) + \rho(\theta, r, x_2) u^2(\theta, r, x_2)\Big) \mathrm{d}\theta \mathrm{d}r \\ &- \int_0^{r_{max}} \int_0^{2\pi} \Big(P(\theta, r, x_1) + \rho(\theta, r, x_1) u^2(\theta, r, x_1)\Big) \mathrm{d}\theta \mathrm{d}r \end{aligned} \tag{5.11}$$

Mixing plane In the case of the mixing plane calculation the lateral boundaries of the channel are connected by a simple condition of spatial periodicity. Therefore the flow of dynalpy through the two surfaces can be multiplied by the number of blades of the front row, for S_1, and the rear row for S_2. Subsequently the net net flow of dynalpy through the 360° control volume is obtained by the two surfaces flow difference.

Chorochronic Chorochronic calculations provide unsteady results, that involve a process of reconstruction of the 360° flow field a little more complicated than the mixing plane geometrical duplication. In fact the flows around two consecutive blades of the same rotor correspond to different time instants, as explained in details in section 6.2.1. In other words, to compose the complete field around the machine, the results extracted at several iterations must be used. Therefore it is no longer possible to base the thrust calculation on a single channel flow but the difference from the inlet and the outlet fluxes through each rotor must be calculated after the reconstruction of the entire machine. In this way the instant thrust will be correctly obtained.

Actually, even after the chorochronic reconstruction, the unsteadiness of the results makes the integral thrust not constant in time. In particular these fluctuations have, as period, the chorochronic period δt. In fact, if one considers the flow around a blade, he will find the same flow around the next blade only after the chorochronic period. This two instants will provide the same integral thrust value, but between them it can be different. Anyway the frequency of this fluctuation is quite high, and the variation in the thrust are supposed to be negligible.

However this concept shows that a local thrust can be identified with respect to the azimuthal position around the machine. This field of force has different values for each angular position and it is not constant in time. This consideration may be important in studies focused on aeroelasticity phenomena, because they show how the ratio between the number of blades of the two rotors and the blade passing frequency can have influences on the frequency of some aerodynamic strains. Moreover the thrust calculation strategy applied to the chorochronic analysis performed during the present study finds its explanation from these remarks. In fact the periodicity of the thrust variation allows to calculate an 360°-averaged value of the dynalpy flux for each x-normal surface, and then to applicate the equation 5.10 on page 73 to obtain the integral thrust.

Finally the thrust results of chorochronic simulations show that the angular fluctuation can be neglected. In fact, performing the comparison of the dynalpy flow through S_2 for different time instant, no remarkable variations occur. This is likely due to the position of S_2, that it is quite far from the propellers allowing the local effects of the blades to be mixed out, generating a flow nearly uniform in the tangential direction.

Torque

The equation 5.11 on the preceding page can also be used to calculate the torque absorbed by an isolated row. In fact if the transported quantity through the control volume is the tangential component of the momentum, the resultant of the external forces acting on the flow is the torque absorbed by the row.

Nevertheless, the presence of a second contra-rotating propeller prevent this method from being applied in a CROR configuration. In fact, its purpose is to reduce the tangential amount of momentum converting this one to a longitudinal motion. Thence the integral calculation would capture a very low flux of tangential momentum through the downstream surface. Even the region between the two propellers is actually affected from the effects of the second rotor, preventing the possibility of analyzing the two rows separately. For these reasons the torque has not be calculated for the configuration analyzed on the present work, but the solution that should be adopted in the future development is the integration of pressure and viscous strain on the blade walls.

5.3.2 Richardson extrapolation

The Richardson extrapolation is one of the most effective techniques to evaluate the error due to the numerical discretization [36]. It can be applied both to the space and the time discretization but in the present section we will consider, as an example, only the effects of the mesh, being aware that a similar discussion can be made for the time step. The goal of the analysis is to have a curve that shows the effect of the grid dimension on a quantity value, where an asymptotic trend should occur. Therefore the problem in this evaluation is to know a reference solution to calculate the error involved by a certain coarse level of the mesh.

The Richardson extrapolation method is based on the hypothesis that the space discretization error δ_g can be specified by using a series, which involves the cell dimensions and the precision order of the numerical scheme that is applied:

$$\delta_g = \phi_{math} - \phi_{num-g} = \sum_{i=1}^{n} \alpha_i h^{p_i} \tag{5.12}$$

introducing:

ϕ_{math} : the value of the quantity ϕ in the exact continuous solution of the equations
ϕ_{num-g} : the value of the quantity ϕ in the solution obtained on the considered grid g
n : the number of terms used in the series;
α_i : a function of the mesh and the quantity considered to evaluate the error;
h : a measure of the cell dimension;
p_i : the truncation error of the i^{th} term

In particular the terms α_i and p_i are different combinations of the derivatives of the quantity ϕ with respect to h.

Therefore the *asymptotic state* is the range of cell dimensions h in which the dominant term of the series is the term with the lowest order. Which means that the error is only due to the precision order of the numerical scheme, and there is no other sources of error that come from a too coarse spatial discretization. Thence, for a solution calculated on a grid in the asymptotic range, the error can be written as

$$\delta_g = \alpha h^{p_{obs}} \tag{5.13}$$

Where p_{obs} is the observed order of the scheme, which means the effective precision order that corresponds to the considered mesh and quantity. In this frame the exact solution ϕ_{math}, the observed order p_{obs} and the coefficient α are the 3 unknowns of the problem of evaluation of δ_g. Therefore by calculating the numerical solution on three mesh with different cell dimensions, the solution of the system allows to estimate the value of the error due to the spatial discretization. It is worth to focus on the hypothesis that p_{obs} and α are considered as constant for the three meshes, which means that all the grids are in asymptotic range, that can be a quite restrictive condition.

If the cell dimensions of the three grids are h_1, h_2, h_3 from the finest to the coarsest, and introducing:

ϕ_k : the solution on the k^{th} grid

$$\begin{aligned} r_{21} &= \frac{h_2}{h_1} \qquad & r_{32} &= \frac{h_3}{h_2} \\ \varepsilon_{21} &= \phi_2 - \phi_1 \qquad & \varepsilon_{32} &= \phi_3 - \phi_2 \end{aligned} \tag{5.14}$$

the system can written as:

$$p_{obs} = \left| \frac{\ln |\varepsilon_{32}/\varepsilon_{21}|}{\ln(r_{21})} + q(p) \right| \tag{5.15}$$

$$\phi_{RE} = \frac{(r_{21}^{p_{obs}} \phi_1 - \phi_2)}{r_{21}^{p_{obs}} - 1} \tag{5.16}$$

$$\delta_{g-RE_1} = \left| \frac{\phi_{RE} - \phi_1}{\phi_{RE}} \right| \tag{5.17}$$

$$\text{with : } q(p_{obs}) = \ln\left(\frac{r_{21}^{p_{obs}} - s}{r_{32}^{p_{obs}} - s} \right) \qquad \text{and} \qquad s = 1 \cdot \text{sign}\left(\frac{\varepsilon_{32}}{\varepsilon_{21}} \right) \tag{5.18}$$

where ϕ_{RE} is the extrapolated solution and δ_{g-RE_1} is the extrapolated error of the finest mesh. At the same way the other error can be calculated:

$$\begin{aligned} \delta_{g-RE_2} &= \left| \frac{\phi_{RE} - \phi_2}{\phi_{RE}} \right| \\ \delta_{g-RE_3} &= \left| \frac{\phi_{RE} - \phi_3}{\phi_{RE}} \right| \end{aligned} \tag{5.19}$$

to finally obtain the needed curve.

5.4 Time discretization

5.4.1 Time step calculation

The time step is the increase of physical time between an iteration and the following one. This actually determine the sampling frequency used to reconstruct the periodic signal generated by the flow unsteadiness. In other words if the time step is too long, for instance, some important physical information will be lost. Therefore the definition of the time step is strictly connected to the physics of the phenomena we want to simulate.

The definition of the principal unsteadiness allows to identify the period of the signal we need to reconstruct using the samples obtained by the result of each iteration. Being the purpose of the chorochronic simulation the analysis of the rotor-rotor deterministic interactions, the unsteadiness periods T_1 and T_2 can be obtained by the blade passing frequency of the two rotors:

$$T_1 = \frac{2\,\pi}{Z_2\,|\Omega_1 - \Omega_2|} \tag{5.20}$$

$$T_2 = \frac{2\,\pi}{Z_1\,|\Omega_1 - \Omega_2|} \tag{5.21}$$

where Z_1 and Z_2 are the number of blades of the two rotors and $|\Omega_1 - \Omega_2|$ is the relative velocity of revolution between the rows.[2]

Subsequently the sampling period can be obtain as a fraction of T_1 and T_2. First of all we divide the period of each row by its number of blades, obtaining a common expression for the two rotors. This is useful because it means that the two passage periods will be sampled by two whole numbers of iterations. Finally a further reduction factor is needed to obtain a time step sufficiently low: $Nq0$.

$$\Delta T = \frac{2\,\pi}{Z_1\,Z_2\,|\Omega_1 - \Omega_2|\,Nq0} \tag{5.22}$$

In particular the factor $Nq0$ will be the parameter that allows to set the time step to different values, keeping the property of being representative for the two rows. The convenience of using this factor will be clear in section 6.2.1, where it will be very practical during the operation of chorochronic assembly.

5.4.2 Time step convergence

Once the choice about the time integration method is accomplished, the most important parameter to properly simulate the flow evolution in time is the time step. This is the increase of the physical time between an iteration and the following one. Which means that, with a long time step, the simulation of a blade passage period, for instance, will be faster than the case with a shorter time step. Nevertheless the temporal discretization needs to be sufficiently fine to properly capture the main flow unsteadiness. Therefore an evaluation of the global effect of the time step on the final solution has been performed. In particular three time step have been tested. According to the time step expression (5.23), presented in the section 5.4.1, the parameter used to set up the time step is $Nq0$.

$$\Delta T = \frac{2\,\pi}{Z_1\,Z_2\,|\Omega_1 - \Omega_2)|\,Nq0} \tag{5.23}$$

The values typically taken by $Nq0$ in turbomachine simulations are around 10, but in the configuration analyzed in the present work, the number of blades of the two rows are particularly low. This characteristic involves lower blade passing frequencies, thence even a lower $Nq0$ value can be sufficient. Actually a strong dependence of the flow from this parameter has been brought to light for such a low values, therefore the convergence analysis has been performed using $Nq0 = 150, 87, 50$.

Subsequently the Richardson extrapolation has been used to identify an extrapolated exact solution which allowed to calculate the error of the three test cases. The physical quantity the analysis is based on, is the time averaged total pressure captured by the fourth probe (placed after the rear rotor) during the iterative calculation process (see fig. 5.3 on page 69 and 5.6b on page 72). The choice has been forced by the long time needed to compute the thrust performance in a chorochronic simulation.

The Richardson technique, based on the quantities described in table 5.1, finally provides an observed order of $P_{obs} = 0.57$ which involves an extrapolated $P_{tot_{extr}} = 0.747$.

[2]The *blade passing frequency* is the frequency by which the blade of a row sees the blades of the other row passing.

time step number	Nq0	time step	P_{tot}	relative error %
ΔT_0	150	7.9488 e-04	0.7180	3.85
ΔT_1	87	1.3705 e-03	0.7075	5.26
ΔT_2	50	2.3846 e-03	0.6931	7.19

Table 5.1: Results of the tested time steps

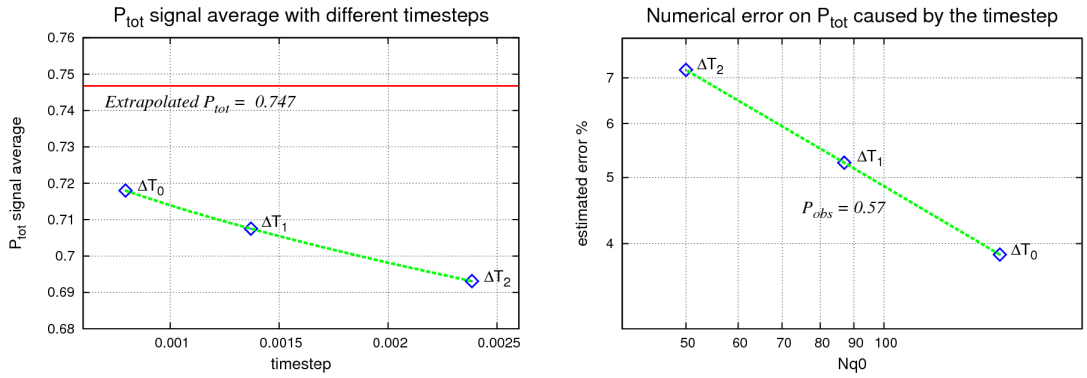

(a) Calculated and extrapolated total pressure **(b)** Temporal discretization Error

Figure 5.8: Time step convergence

In conclusion a particular need of small time steps has been discovered. This means that, in comparison with the internal flow of a classical turbomachine, an open rotor presents some dynamics that are characterized by a frequency much higher than the BPF (blade passing frequency). For instance the blade tip vortices are composed by fast turbulence structures that can generate high frequency components. Thence the need of capturing their evolution and the interactions among them and the downstream rotor can involve the use of a time step quite small. Moreover they are probably stronger than the turbulence structures generated by the blades tip gaps in a turbine or a compressor, and this can explain the peculiarity of the open rotor configuration.

5.4.3 Choice of the time integration method

Three time integration methods have been tested in order to identify the most efficient in terms of time of calculation and quality of the results. The compared techniques are the first order *Backward Euler scheme* and the second order *Dual Time Stepping* and *Gear approach*.

Initially, during the set up phase of the chorochronic calculations, a second order method has been applied to avoid eventual problems due to a low precision in the temporal reconstruction. Then, in a following phase, the first order scheme has been tested to verify the possibility of obtaining some good results with a lower cost in terms of CPU time. All the calculations used to compare these methods have been performed with a very low time step ($Nq0 = 150$, see section 5.4.1).

Second order approaches

Between the two second order techniques, the Gear internal algorithm immediately shows to be much more effective. The comparison can be based on the number of internal iterations that

each methods needs to bring the residuals to the imposed value $5 \cdot 10^{-03}$. In fact, as explained in the section 4.5.2, the internal cycle is a steady iterative process that is performed at every external iteration, that means after every increase of the physical time.

After an initial transitory, the Gear internal cycle reaches the imposed lower limit of $5 \cdot 10^{-03}$ with about 3 iterations, while the DTS approach needs around 30 iterations to get to the same values. This is the cause of the huge difference between the calculation speeds of the two methods, which still presents a factor of about 10 as shown by table 5.2. In fact the calculation speed is measured considering the external cycle that corresponds to the physical time progress.

	Calculation speed $[it/hour]$
Gear	345
DTS	35

Table 5.2: Results of the comparison between Gear and DTS time integration schemes

From these considerations the second order time integration method that has been used in every calculation is the Gear approach. Therefore no comparison have been done about the results obtained by the two methods, because of the high computational cost of a complete DTS calculation.

Comparison between *Gear* approach and *Backward Euler* scheme

A further acceleration of the calculation can be obtained by reducing the order of the time integration method. Thence the Backward Euler scheme has been tested. In fact it correspond to the one-step application of the Runge Kutta scheme, not involving an internal cycle as the Gear and DTS approaches. Besides the Backward Euler is an explicit method, for which the CFL condition may become very important to ensure the stability of the numerical scheme. In particular, as discussed in the section 4.5.1, the method use to calculate the convective fluxes becomes instable if the CFL if higher than 1. Nevertheless, in the present application, the viscosity introduced by the viscous fluxes and the turbulence model has stabilized the global scheme, allowing the use of CFL higher than 1.

For the comparison of the results, the thrust obtained by using the two techniques is taken as global quantity able to represent the precision of the simulation. Therefore, assuming the Gear approach more accurate, the Backward Euler involves an error of about 0.877% and a calculation speed about 2.2 times higher than the second order scheme, as shown by table 5.3:

	Calculation speed $[it/hour]$	Calculation time $[hours]$	Thrust
Gear	345	150	6571.2
Backward Euler	820	60	6513.4

Table 5.3: Results of the comparison between Gear and Backward Euler time integration schemes

Moreover no remarkable difference occurs in the number of periods needed by the two approaches to reach a converged state. Thence, in conclusion, the Backward Euler scheme seems to be a very effective possibility for the present applications. Actually in this analysis

the effect of the time step has not be taken into account, and this may be an important factor for the evaluation of the time integration performance. In fact a second order scheme is able to properly reconstruct the unsteady flow even using a time step quite high, while, on the other hand, the Backward Euler is limited by the stability considerations discussed above. Therefore more accurate conclusions can be drawn on a comparison performed after setting the two method to their converged time step, which ensure the minimum calculation time. In the next section this particular condition will be found for the Gear approach.

5.5 Space discretization

5.5.1 Spatial discretization at the walls: y^+

The first verification about the quality of the equations solution process is the control of the spatial discretization near the walls. This can be evaluated by the y^+ coordinate. In fact this is a dimensionless measurement that allows to describe the structure of the boundary layer, as shown in the figure 5.11. Therefore the accuracy of the boundary layer discretization can be evaluated by the limits of the cells near the wall, expressed with the y^+ coordinate. Tipically the boundary layer effects are considered properly simulated if the y^+ coordinate takes values lower than 1. Figures 5.9 and 5.10 show that this criterion is not satisfied everywhere. Nonetheless the mesh is sufficiently fine in the rear part of the blade walls, where a separation of the boundary layer would involve a strong decrease on the rotor performance.

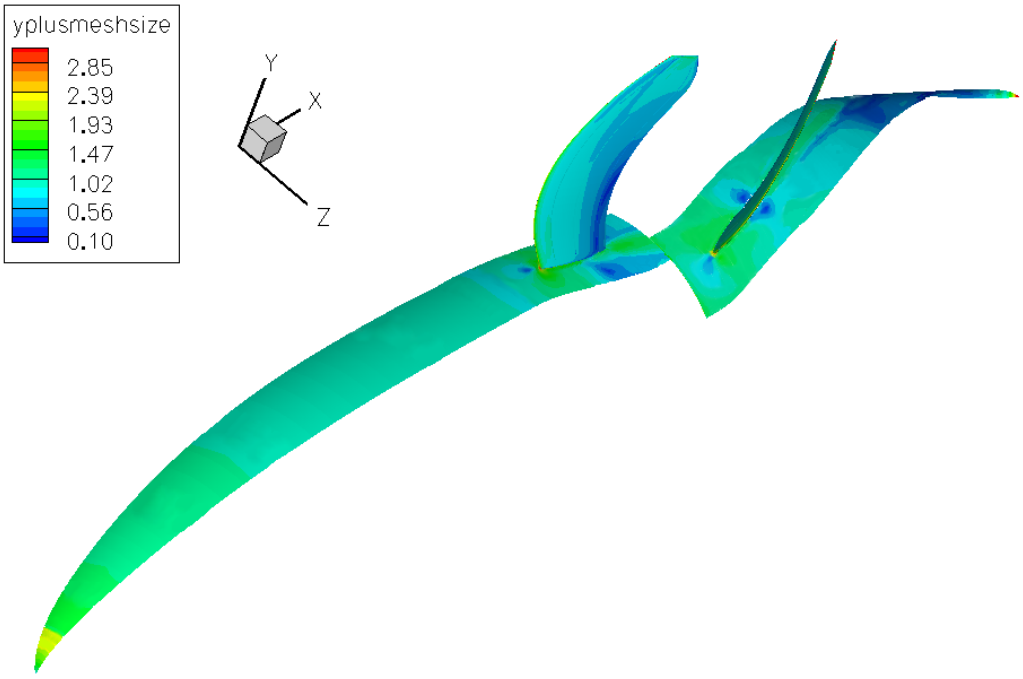

Figure 5.9: y^+ on the walls of the employed geometry

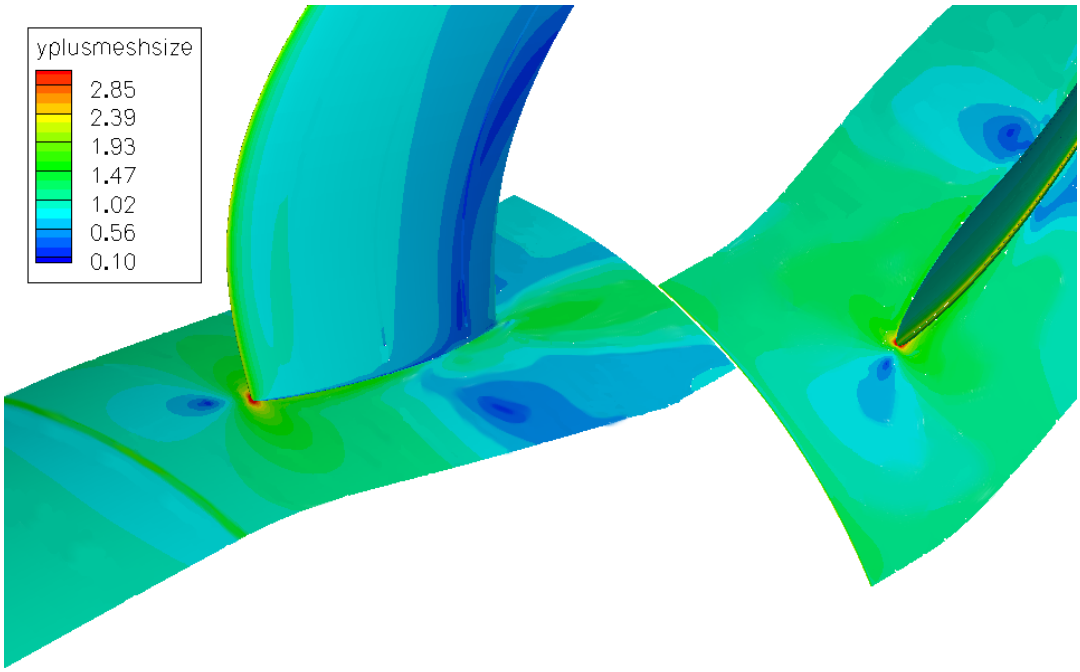

Figure 5.10: y^+ in the root regions

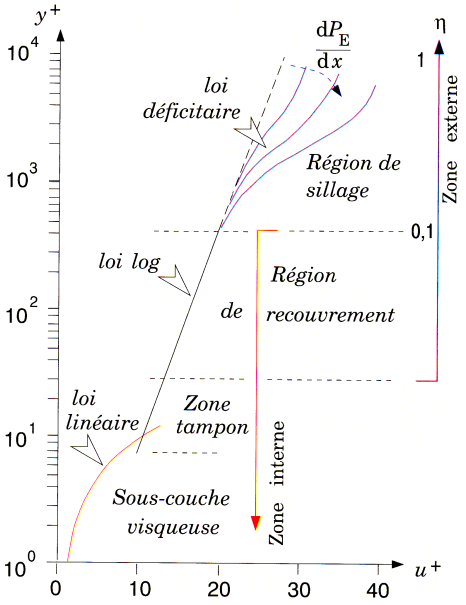

Figure 5.11: Boundary layer structure

5.5.2 Mesh Convergence

The influence of the number of points on the final solution has been evaluated for three mixing plane calculations. This choice is actually due to the time that would be necessary to perform this analysis by using chorochronic calculations. In fact the effects of the number and distribution of points would surely be different. Keeping a fine mesh on whole channel width would be necessary in order to capture the rotor-rotor interactions as, for example, the wakes of the

upstream rotor in the downstream channel. Nevertheless the mixing plane calculations can already give some important information, as described in the following. The three meshes have been compared by using the values of thrust calculated by each flow with the method described in the chapter 6. The first grid that has been used is the finest: 12 millions of points. On this mesh the mixing plane and chorochronic calculations have been tested and a good quality of the results, in terms of expected physical phenomena simulation, has been observed. Therefore the other two grids have been realized decreasing the number of point to respectively a half and a quarter. Actually the need of keeping three levels of multi-grid has not allowed to exactly obtain the fixed size. This last point has finally involved the application of a Newton solver to the implicit equation of the observed order (5.15 on page 77). The decreasing of the grid quality involved by the reduction of the number of points is shown in the tables 3.2 and 3.3 on page 32.

The Richardson technique, based on the grid characteristics that are described in the table 5.4, finally provides an observed order of $P_{obs} = 1.43$ which involves an extrapolated thrust of $T_{extr} = 5739.6$.

grid number	number of points	thrust	relative error %
grid 0	11.804.436	5964.0	3.9
grid 1	5.604.072	6388.7	11.3
grid 2	3.025.632	7374.3	28.5

Table 5.4: Characteristics of the compared grids

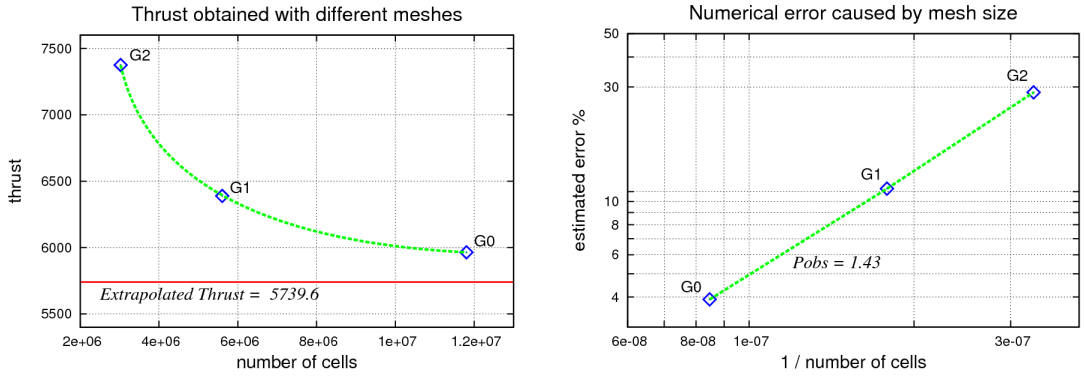

(a) Calculated and extrapolated thrusts **(b)** Spatial discretization Error

Figure 5.12: Results of the mesh convergence analysis

In order to have a confirmation of the good accuracy of the extrapolated T_{extr}, one can notice two principal points of the analysis, according to graphs 5.12:

- the trend of the error with respect to the number of cells is monotonous, with confirm that a finer mesh will provide better results;
- the observed order of convergence is not far from the theoretical Jameson scheme order: 2.

In conclusion, the error of 3.9 % involved by the finest grid can be accepted for the purpose of the present study. Nevertheless, in a future mesh convergence analysis performed by using chorochronic calculations, the hypothesis of using a finer grid at the place of the grid 2 here utilized, should be taken into account.

5.5.3 Multi-grid effects

The multi-grid technique, described in the chapter 4, has been applied to the steady mixing plane calculation in order to accelerate the convergence process. Graphs 5.13 show the residual trends obtained with different levels of multi-grid.

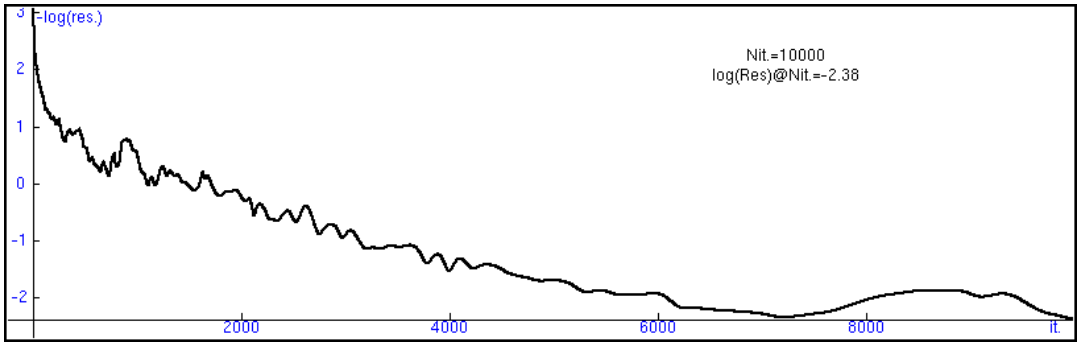

(a) No multi-grid acceleration

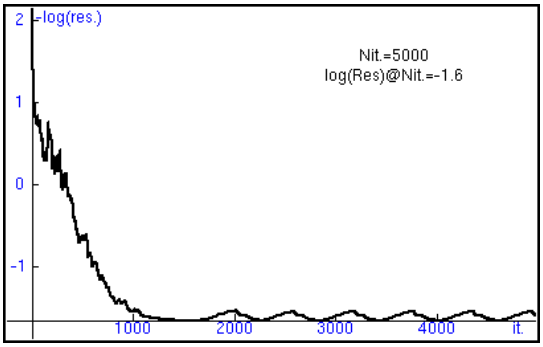

(b) Multi-grid applied with 1 coarse grid

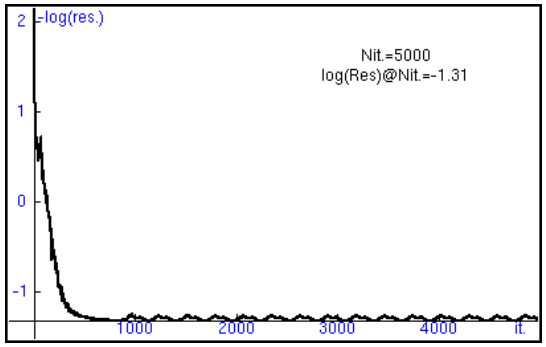

(c) Multi-grid applied with 2 coarse grids

Figure 5.13: Multi-grid effects on a mixing plane calculation

What is worth to notice is that without the application of the multi-grid technique the solution is reaching a converged state only after 10000 iterations, while the use of one coarse grid already allows to obtain the converged solution after 2000 iterations. A smaller gain can still be achieved by using 3 levels of multi-grid (that is 2 coarse grids).

The drawback of this method consists, first of all, in the constraint on the number of points of every topology block of the mesh, as described in chapter 4. Moreover each iteration becomes a little more expensive with the use of several grids, as can be observed in table 5.5, which shows the speed of the three calculations of figure 5.13 in terms of iterations per hour. Nevertheless the gain in terms of time of calculation is very important.

Multi-grid levels	Iterations to converge	Calculation speed	Time to converge
No multi-grid acceleration	10000	980 it/hour	10.2 h
2 multi-grid levels	2000	560 it/hour	3.6 h
3 multi-grid levels	1000	480 it/hour	2.1 h

Table 5.5: Multi-grid effects on mixing plane simulations

5.6 Effects of numerical scheme and turbulence model

The results obtained by different numerical schemes and turbulent models are compared in order to verify the influence of the solution method applied to the Navier Stokes system. In particular the tested numerical schemes are:

- Jameson scheme (second order centered scheme)
- Roe scheme with minmod limiter (second order upwind scheme)

While the turbulence models:

- $k-\omega$ with SST Menter modification
- Spalart Allmaras

Figures 5.15 and 5.16 show some fields corresponding to blade root and blade tip zones. The shown results have been obtained by chorochronic simulation and they have not been reconstructed because of the time this operation requires.

The biggest influence can be seen in the root regions between the two turbulence models. This may be caused be the influence of the spinner boundary layers, which might have developed different characteristics during its evolution from the stagnation point. Graphs 5.14 allow to easily evaluate this difference in a mixing plane simulation.

The thrust performances obtained by the tested methods are shown in tables 5.6 and 5.7. The calculation time shows that the converged solution is reached faster by the Roe scheme associated with the minmod limiter, even if the turbulence model applied in this studies with the Roe scheme is the two equations kω. Nevertheless the choice of the limiter is fundamental for the performance of the Roe numerical scheme. In fact also the third order extension has been tested (see section 4.4.1), but it has not been possible to obtain a converged solution because of the too long calculation time required (a calculation speed of 106 $[it/h]$ has been observed).

numerical scheme	thrust	calculation speed $[it/h]$	convergence time $[hours]$
Roe (minmod limiter)	6333.6	345	80
Jameson	6571.2	174	150

Table 5.6: Thrust performance and computational cost obtained with the tested numerical schemes (chorochronic simulations)

turbulence method	thrust	calculation speed $[it/h]$	convergence time time $[hours]$
kω (SST Menter)	6571.2	174	150
Spalart Allmaras	5001.6	260	100

Table 5.7: Thrust performance and computational cost obtained with the tested turbulence models (chorochronic simulations)

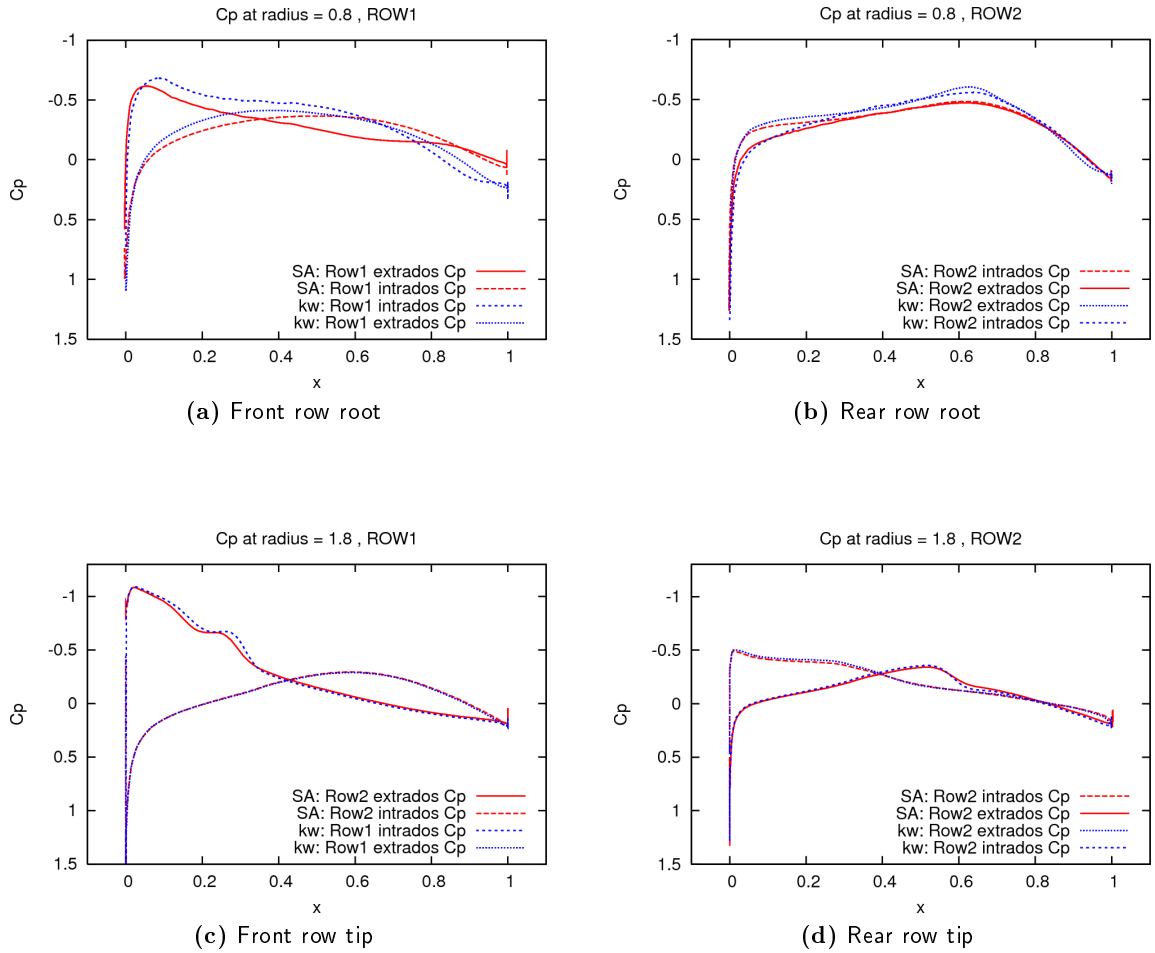

(a) Front row root **(b)** Rear row root

(c) Front row tip **(d)** Rear row tip

Figure 5.14: kω and Spalart Allmaras pressure coefficient distributions (mixing plane simulations)

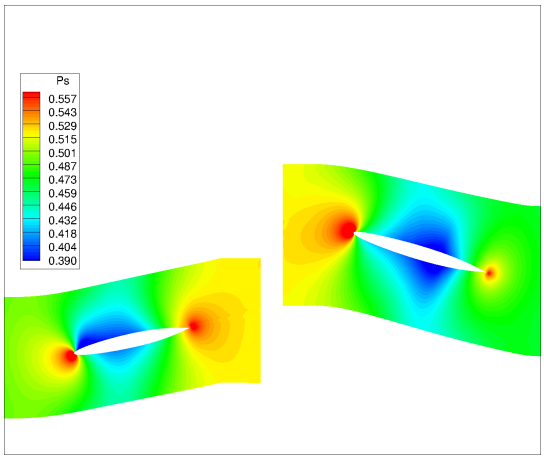

(a) Roe - kω (Static pressure)

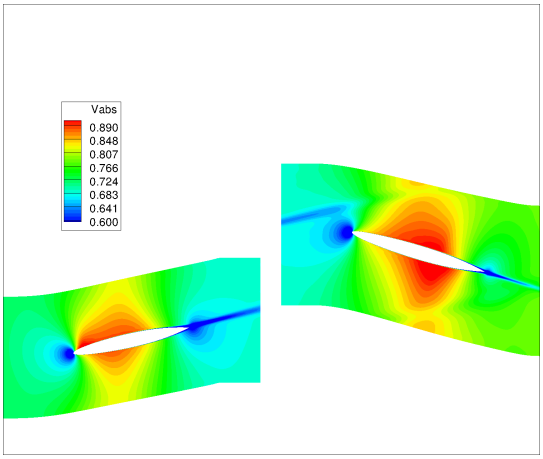

(b) Roe - kω (Absolute velocity)

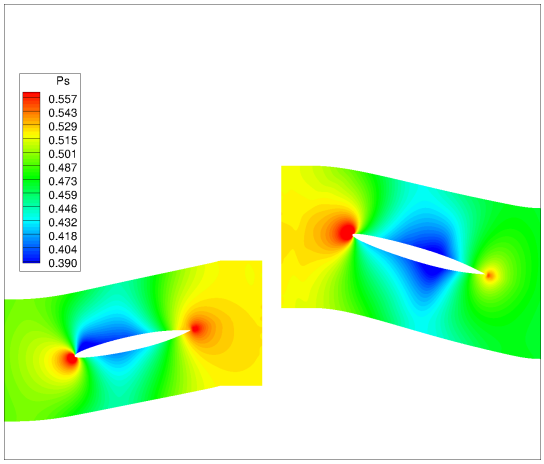

(c) Jameson - kω (Static pressure)

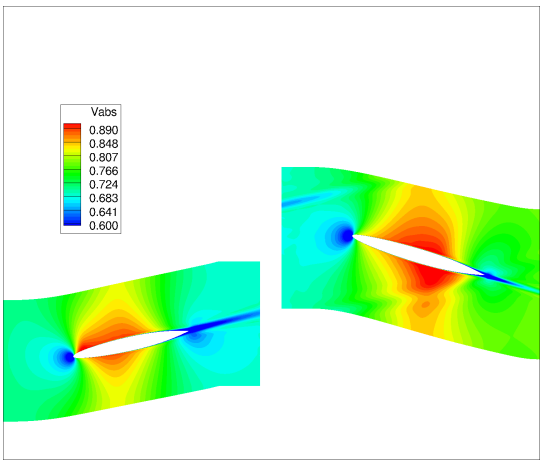

(d) Jameson - kω (Absolute velocity)

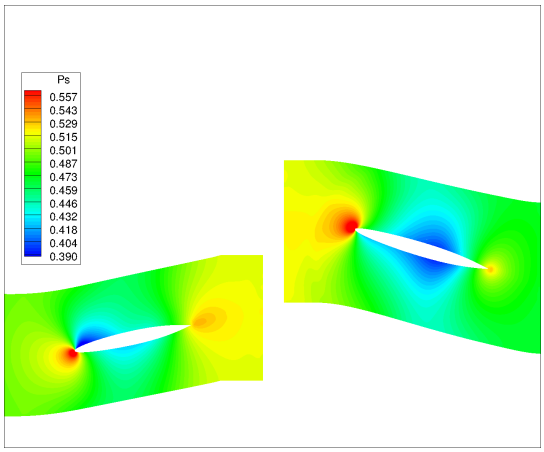

(e) Jameson - Spalart Allmaras (Static pressure)

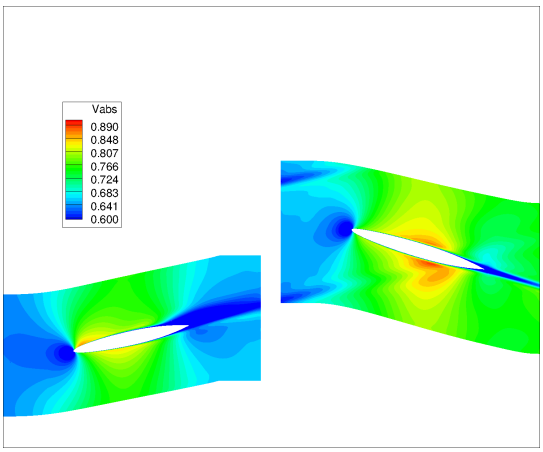

(f) Jameson - Spalart Allmaras (Absolute velocity)

Figure 5.15: Static pressure and velocity close to blade roots (chorochronic simulations)

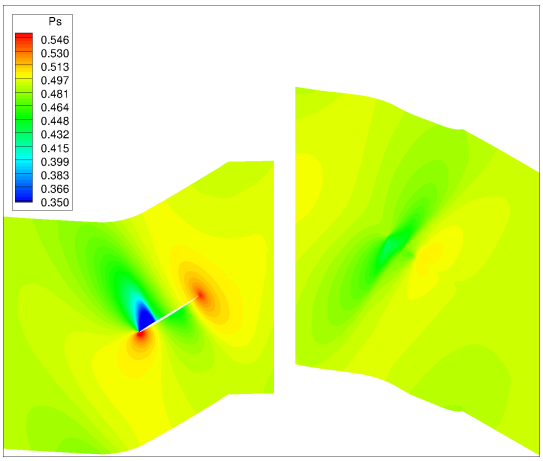

(a) Roe - kω (Static pressure)

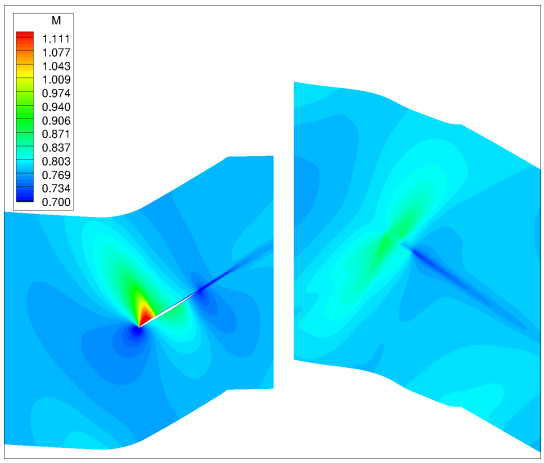

(b) Roe - kω (Mach number)

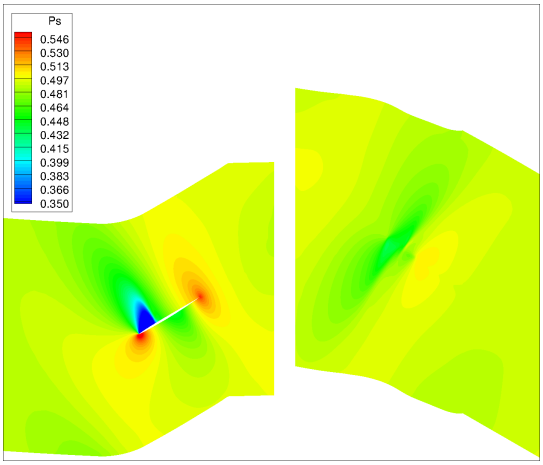

(c) Jameson - kω (Static pressure)

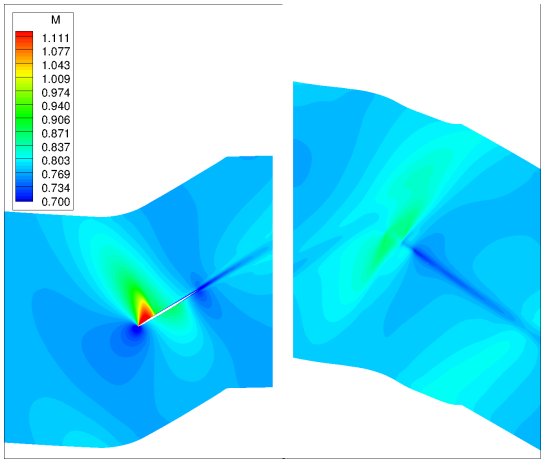

(d) Jameson - kω (Mach number)

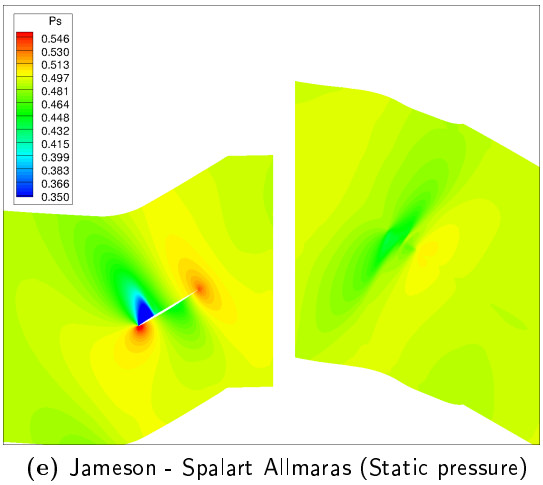

(e) Jameson - Spalart Allmaras (Static pressure)

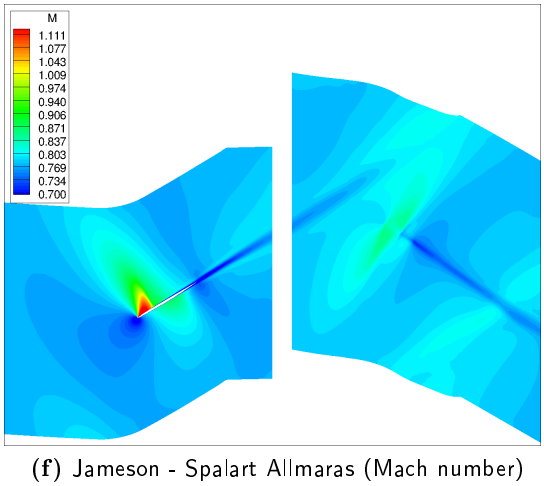

(f) Jameson - Spalart Allmaras (Mach number)

Figure 5.16: Static pressure and Mach number close to blade tips (chorochronic simulations)

Chapter 6

Validation of the solutions

Contents

6.1 Introduction

As mentioned in the introduction of this report, this chapter should compare the simulation results with the real flow, typically represented by a windtunnel experiment or an analytical solution. Unfortunately no terms of comparison were available to validate the solutions, thence a simple qualitative description of the existing dynamics is presented. This confirms the quality of the results, which are quite close to the predicted reality and to the expectations based on the theory of contra-rotating propellers.

6.2 Post processing of the results

6.2.1 Chorochronic reconstruction

As explained in section 2.5, the space coordinates of the grid points do not change during a chorochronic calculation. Nonetheless the boundary conditions simulate the rotation of the discretized blades around the machine, see figure 6.1a on the next page. This means that a process of reconstruction is needed to bring in the right position each result extraction and to obtain multi-channel fields.

The first step, once the field corresponding to a certain iteration is loaded on the mesh, is the rotation of the two sub-domains to the angular position reached by each blade during the calculation. This operation is possible thanks to the knowledge of the time stepΔT, the extraction iteration N, the initial position θ_0 and the rotation velocity of the rows Ω:

$$\theta = \theta_0 + \Delta T N \Omega \tag{6.1}$$

The figures 6.1b and 6.1c show the effect of the step 1.

Subsequently a multi-channel field can be obtained by assembling different extractions, that is single-channel fields corresponding to different time instants.

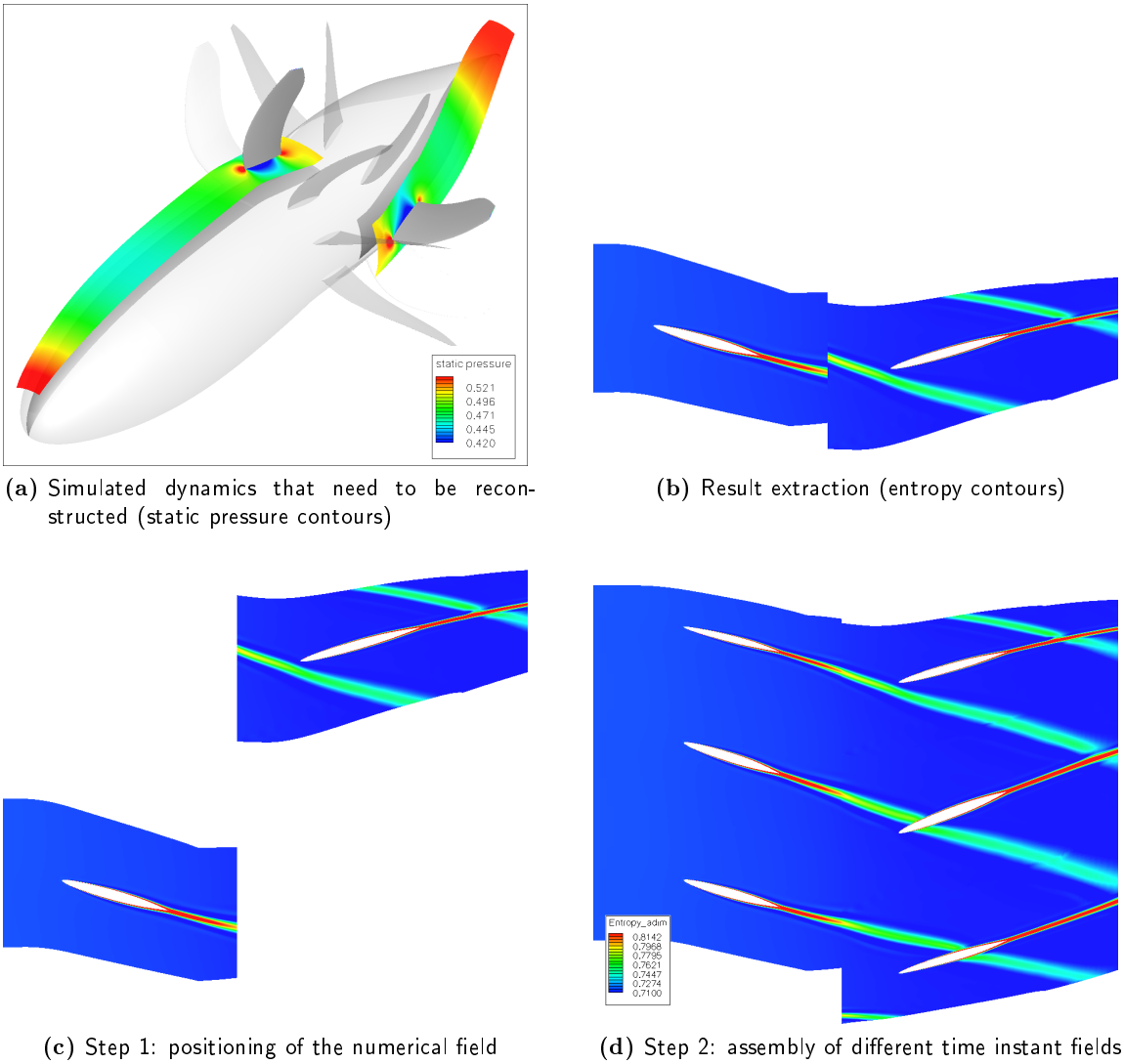

(a) Simulated dynamics that need to be reconstructed (static pressure contours)

(b) Result extraction (entropy contours)

(c) Step 1: positioning of the numerical field

(d) Step 2: assembly of different time instant fields

Figure 6.1: Chorochronic reconstruction steps (entropy contours)

The number of iterations that one has to wait in order to have the fields around two following blades can be determined as follows. It is worth to remind that the chorochronic period is defined as the necessary time step δt for the flow around a blade to occur around the next or the previous blade of the same row, and it is expressed by:

$$\delta t = \left| \frac{\frac{2\pi}{Z_1} - \frac{2\pi}{Z_2}}{\Omega_1 - \Omega_2} \right| \tag{6.2}$$

From this time one can obtain the corresponding number of iterations n_{it} by dividing it by the time step ΔT, which is defined as the time increase of each iteration:

$$\Delta T = \frac{2\,\pi}{Z_1\,Z_2\,|\Omega_1 - \Omega_2|\,Nq0} \tag{6.3}$$

$$n_{it} = \frac{\delta t}{\Delta T} = \frac{2\,\pi\,|Z_2 - Z_1|}{Z_1\,Z_2\,|\Omega_1 - \Omega_2|}\,\frac{Z_1\,Z_2\,|\Omega_1 - \Omega_2|\,Nq0}{2\,\pi} = |Z_2 - Z_1|\,Nq0 \tag{6.4}$$

This simple relation is fundamental to perform the extractions at the right iterations.

6.2.2 Pressure Coefficient distribution on the blade surfaces

The accuracy of the chorochronic method in capturing unsteady phenomena allows to observe the effects of the row interactions on the pressure coefficient distribution on the blade surfaces. The most remarkable case is when a downstream rotor blade passes through the wake of a front blade. Figures 6.2 to 6.6 refer to an airfoil positioned at about 95% of the rear rotor span. In particular, in figure 6.2 the distributions of pressure coefficient on the airfoil at four time instants are overlapped. The different instants correspond to the conditions represented by figures 6.3, 6.4, 6.5, 6.6, and show that the low velocity zone inside the wake, combined with the revolution motion of the crossing blade, causes a local peak of incidence. This is visible when the leading edge goes into the wake and an augmentation of local velocity occurs, corresponding to a pressure coefficient reduction, (see figure 6.3). A similar dynamics exists when the trailing edge is leaving the wake. These phenomena are more evident close the tips of the blades, where the tangential velocities are higher.

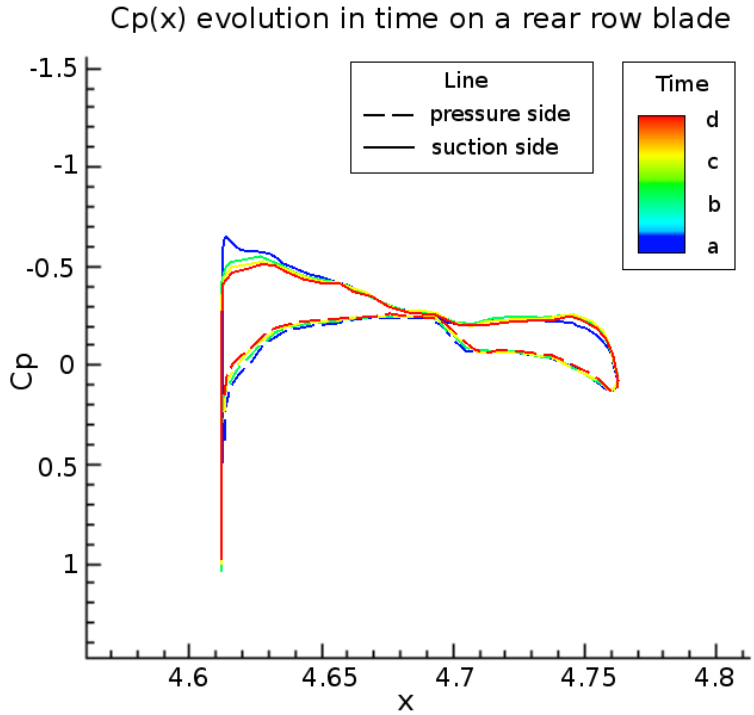

Figure 6.2: Pressure coefficient on a rear blade airfoil while crossing a front blade wake (see fig. 6.3, 6.4, 6.5, 6.6)

Taking into consideration the upstream blades, the potential effects of the second rotor also affect the pressure distribution, as can be observed by the signal of the probe 1 used to monitor the convergence (figure 5.5 on page 71). However these phenomena are less evident than the wake effect on the rear blades.

This kind of interactions is the origin of strong unsteadiness in the load distribution and they absolutely have to be taken into consideration during design steps and aeroelastic analysis.

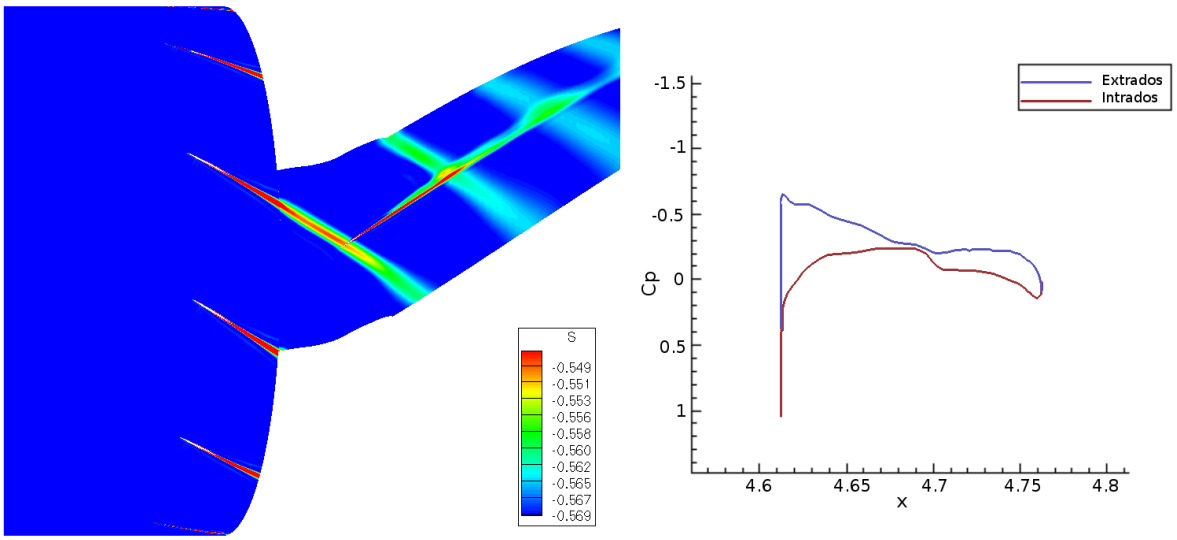

Figure 6.3: Entropy contours and pressure coefficient evolution on a downstream blade, instant **(a)**

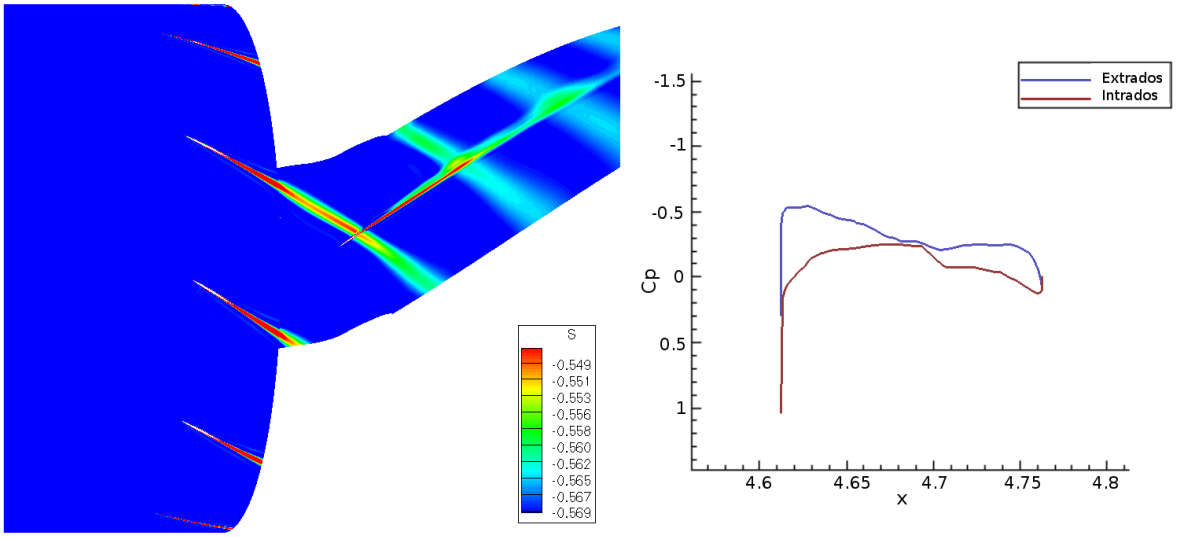

Figure 6.4: Entropy contours and pressure coefficient evolution on a downstream blade, instant **(b)**

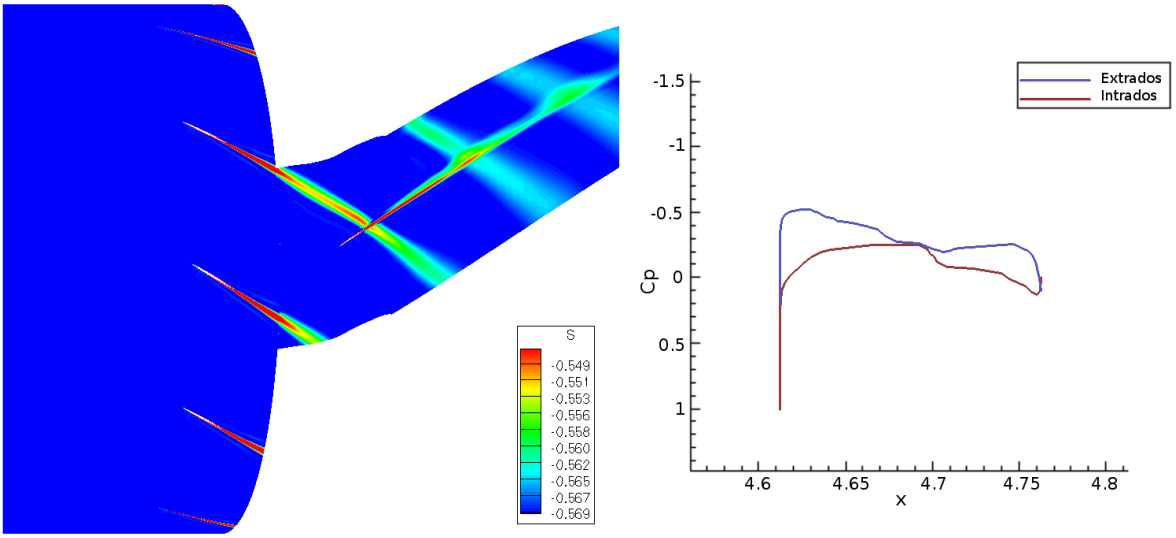

Figure 6.5: Entropy contours and pressure coefficient evolution on a downstream blade, instant **(c)**

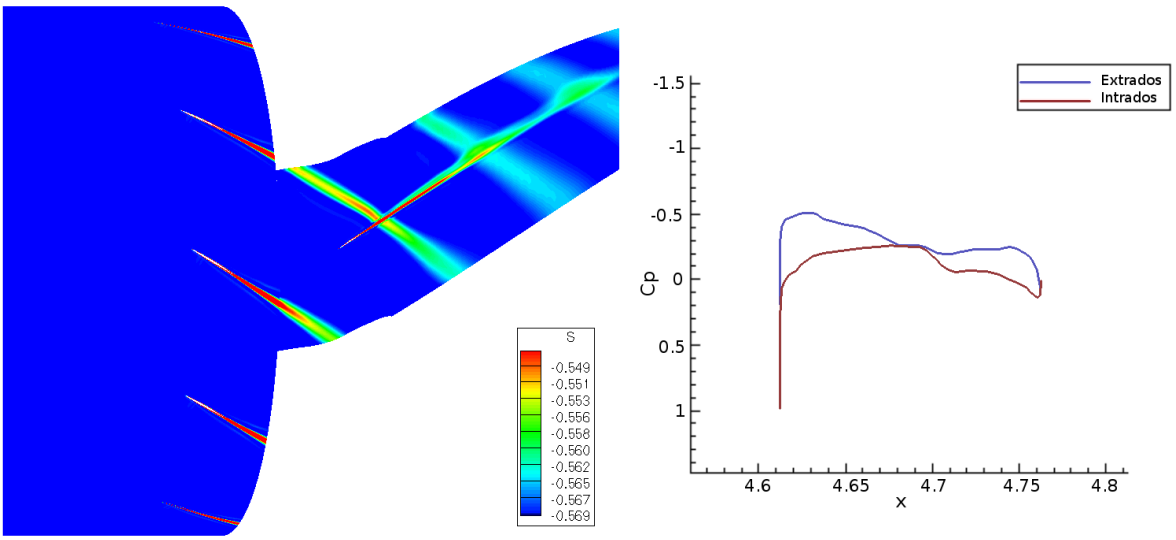

Figure 6.6: Entropy contours and pressure coefficient evolution on a downstream blade, instant **(d)**

6.2.3 CROR slipstream convection

A qualitative analysis of the flow convection in the slipstream of the propeller can be performed by the sequence 6.7. The point where two blade wakes cross themselves provide a practical reference to follow the convection. By the motion of these points one can remark that the downstream flow has almost no azimuthal component of velocity. Therefore the effect of the second contra-rotating rotor is what expected by the theory.

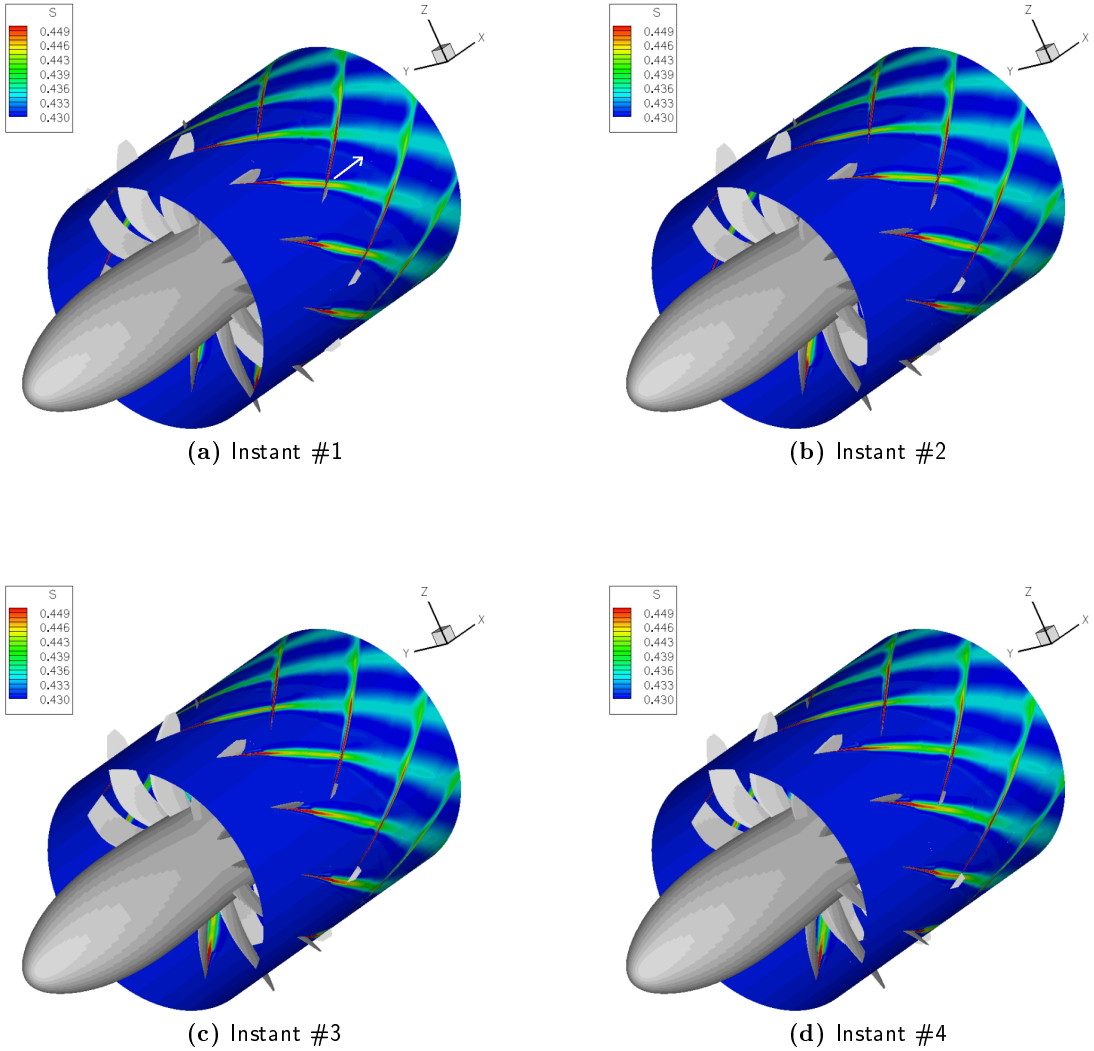

(a) Instant #1

(b) Instant #2

(c) Instant #3

(d) Instant #4

Figure 6.7: Unsteady potential effects between the two rotors (entropy contours)

6.2.4 Blade tip dynamics

An important element that characterizes the CROR configuration is the absence of the casing, which involves blade tip phenomena as tip vortices. For this reason a very fine mesh as been realized to discretize regions close to blade tips. As shown in figures 6.9 and 6.10 on the next page, this also allows to capture shock phenomena with a high precision.

Figure 6.8 shows the presence of tip vortices by using the Q criterion. This method allows to identify the vortex regions by means of the Q parameter, defined as:

$$S_{ij} = \frac{1}{2}\left(\frac{\partial u_i}{\partial x_j} + \frac{\partial u_j}{\partial x_i}\right) \tag{6.5}$$

$$\Omega_{ij} = \frac{1}{2}\left(\frac{\partial u_i}{\partial x_j} - \frac{\partial u_j}{\partial x_i}\right) \tag{6.6}$$

$$Q = \frac{1}{2}\left(\|\Omega\|^2 - \|S\|^2\right) \tag{6.7}$$

Therefore Q tends to zero outside vortices and it is greater than 1 inside. Nonetheless, in figure 6.8 the level of the Q parameter used to show the green surfaces is lower than 1, because of the difficulty of the post-processing software in calculating partial derivatives near the faces of the topological blocks of the grid. Thus, the presence of vortices can be observed, being aware that their real extension is much larger.

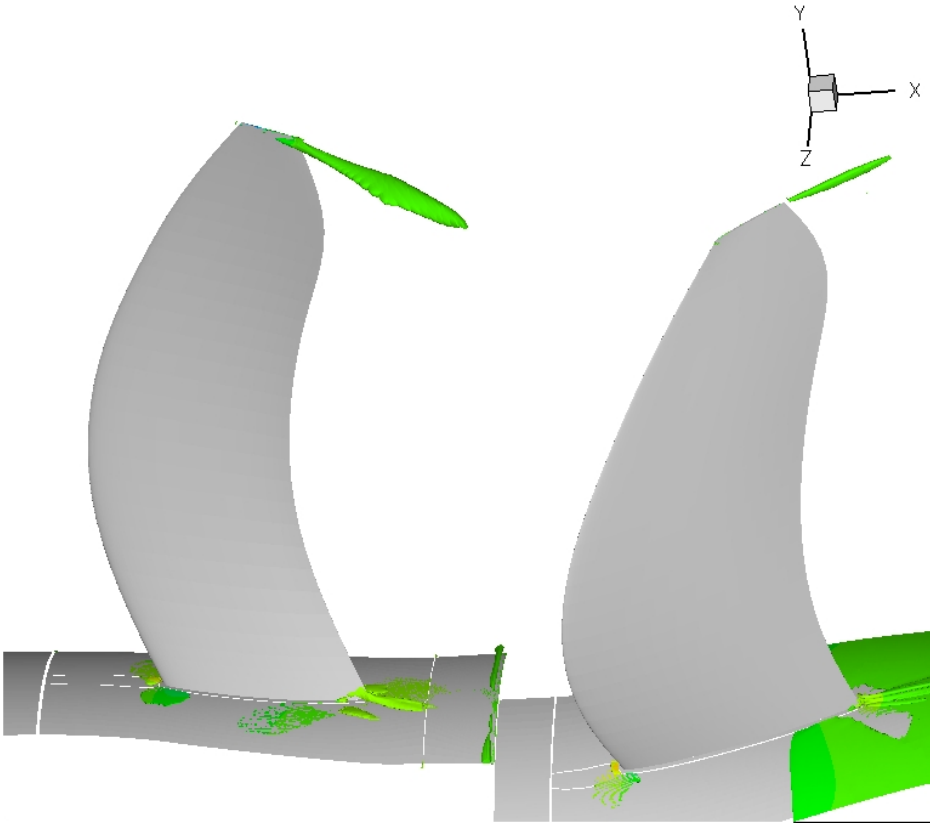

Figure 6.8: Tip vortices shown by using the Q criterion

The high mesh density allows to capture a shock wave on the suction side of the airfoil and to follow its high entropy wake being convected downstream. An accurate unsteady simulation of these kind of phenomena is also fundamental in the design of the blade shape. In fact they may cause aeroelastic dynamics due to transonic flutter, as well as compressibility losses of energy.

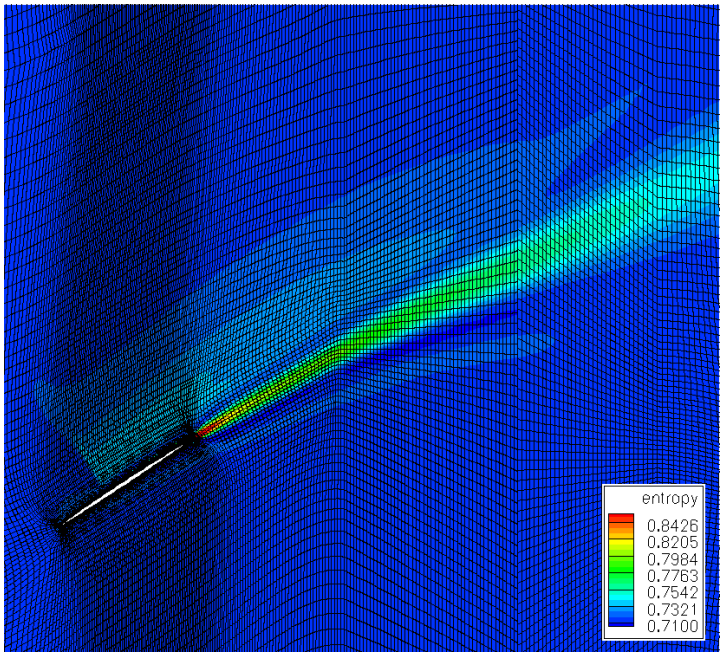

Figure 6.9: Shock wave captured thanks to the high mesh density (entropy contours)

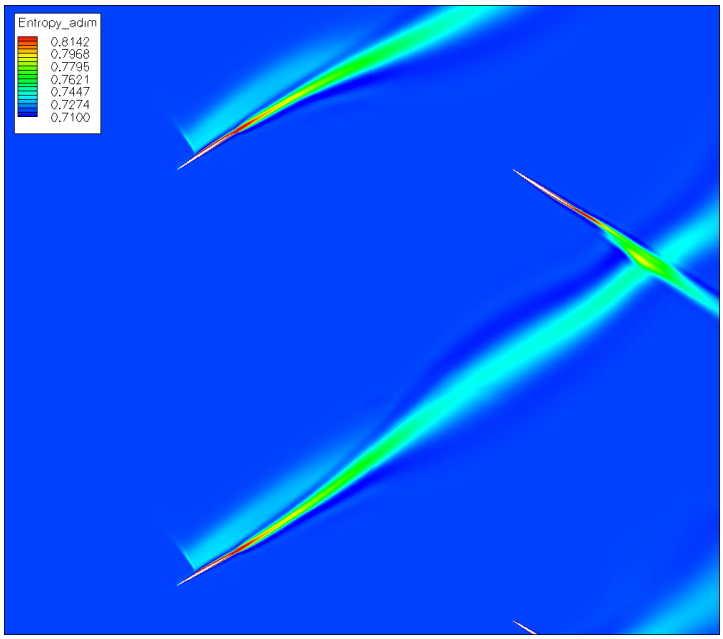

Figure 6.10: Convection of the high entropy regions caused by the shock waves (entropy contours)

6.2.5 Comparison between Mixing Plane and Chorochronic approaches

As expected by the method limits described in chapter 2, the entropy field of the mixing plane simulation (figure 6.11a) shows the mixing-out of the blade wakes at the interface plane, giving a non-physical flow field. In fact the rear rotor receives a constant and uniform inlet flow. Nonetheless the effect of the upstream rotor is well perceived by the second one. This can be seen by the uniform flow at the inlet zone of the rear rotor, since its degree of entropy is higher than that of the upstream undisturbed field. Moreover the potential effects of the downstream blades propagate towards the front row and they are transmitted to the upstream side of the interface. This con be observed in figure 6.12a, where the blue low Mach number regions close to the stagnation points at the trailing edge of the upstream blades, become wider near the interface. The difference between these regions and the shape of the rear blade wakes, clearly shows that the mixing plane method is able to model a kind of row interactions by a steady calculation, but providing a non-physical field.

In the chorochronic results the flow field characteristics are correctly transmitted through the interface between the rotors. This allows to capture the deterministic unsteadiness of the row interactions. For instance figure 6.11b shows the impact of the downstream blades with the upstream row wakes, which is the source of important acoustic phenomena. Moreover the effects of the front row wakes on the distribution of Mach number around the rear airfoils may cause periodic aeroelastic phenomena that have to be taken into account in the design step of the propellers (figure 6.12b).

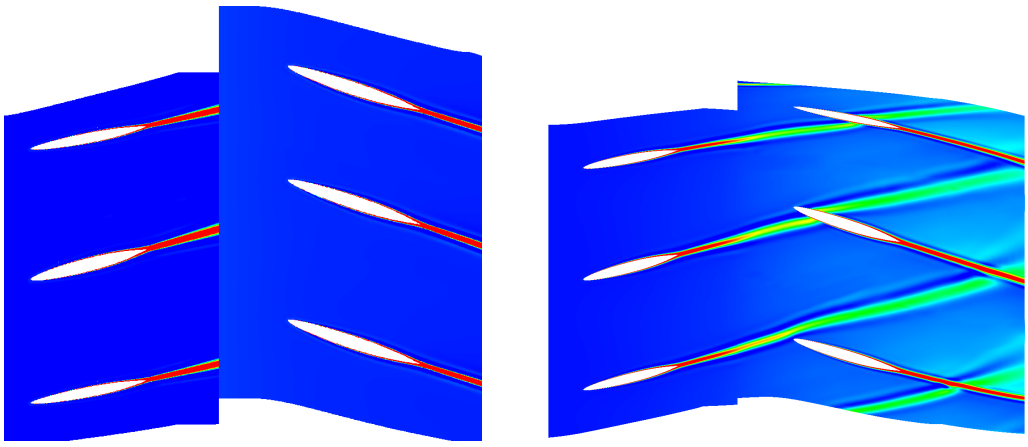

(a) Mixing plane simulation **(b)** Chorochronic simulation

Figure 6.11: Mixing plane and Chorochronic entropy flows

The thrust performance obtained by the two methods are shown in table 6.1, with the corresponding time necessary to reach a converged solution. As one can observe the steady calculation involves en error of -9.2 % with respect to the unsteady simulation, but the calculation time is 98% lower. The thrust difference is caused by the averaging process the mixing plane method is based on. In fact the conservation of the Riemann invariants applied in the presents study, causes an increase of entropy, which cannot be conserved because of the inherent non-linear nature of the conservation equations. According to the theory presented in section 2.3, the conservation of other averaged quantities can be imposed, and this may provide more accurate results. Unfortunately this kind of test has not been performed during the present work, but it may represent a motivation for future investigations.

method	thrust	calculation time [*hours*]
mixing plane	5964.0	2
chorochronic	6571.2	150

Table 6.1: Thrust performances obtained by the two methods and their computational cost

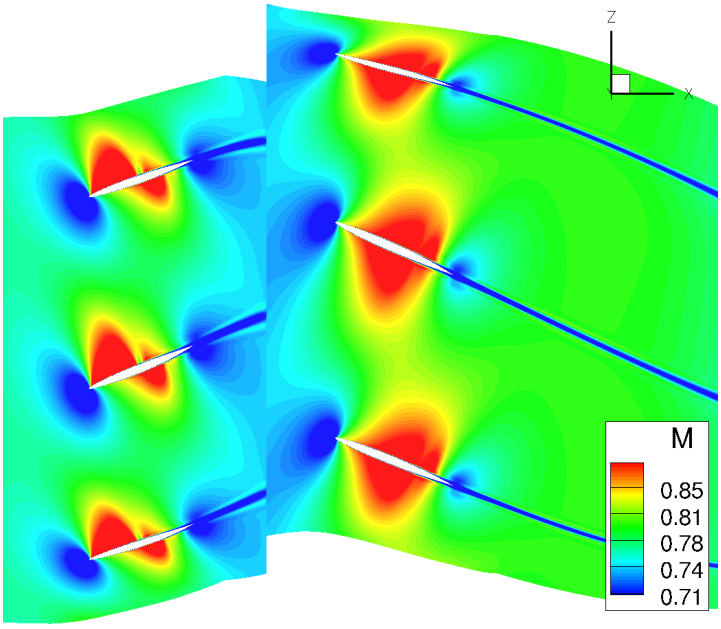

(a) Mixing plane simulation

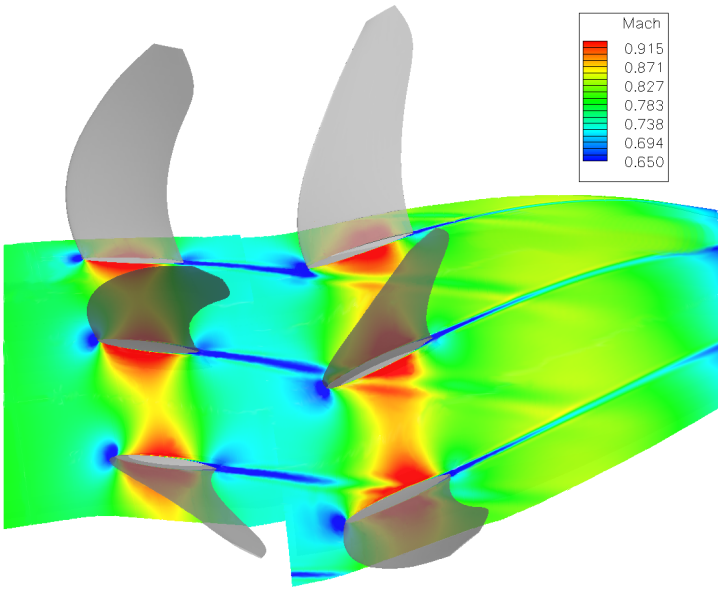

(b) Chorochronic simulation

Figure 6.12: Mixing plane and Chorochronic relative Mach numbers

Chapter 7

Conclusions and future developments

7.1 Conclusions

The first step of the work has been the set up of numerical simulations to a contra-rotating open rotor configuration. In particular the challenge was the application of turbomachine dedicated tools in presence of an open field. This purpose has been successfully achieved bringing into light some important points in the use of the code and the mesh generator. Among them the most important are:

- the low mesh quality in the external field, that may prevent the relative velocity formulation from being applied;
- the high number of grid points necessary to capture the rotor-rotor interaction phenomena;
- the very low time steps in relation to typical turbomachine simulations, necessary to capture high frequency dynamics caused by the open field (ex. tip vortices).

The remark of these particularities and their analysis, have allowed the achievement of a good experience in the use of the tools that have been applied, such as the mesh generator Autogrid and the Richardson extrapolation.

Moreover some useful techniques have been tested for the monitoring of the convergence. The efficiency of the multi-grid acceleration method has been verified. The Fourier analysis has proved to be an effective tool to analyze the periodicity of the signal captured by some well positioned probes, in the case of an unsteady calculation.

The second step has been the analysis of the results, in order to verify the capability to simulate the rotor-rotor unsteady interactions that represents the goal of this work. Unfortunately no terms of comparison were available to validate the solutions, thence a simple qualitative description of the present dynamics has been performed. This has confirmed the quality of the results, which are quite close to the predicted reality. In fact the chorochronic reconstruction that have been realized showed that the potential and the wake effects are clearly visible and affect the pressure distribution on the blades, which has a periodic trend. These visualizations also show that main direction of the flow in the wake is parallel to the propellers axis, as expected by the theory of contra-rotating propellers.

Moreover this step has allowed the comparison among different numerical schemes and turbulence models as well as time integration methods. These comparisons may open the

possibility to perform new analysis to understand in details the differences showed in this report.

7.2 Future developments

Starting from the present work conclusions, the difference that occurs between the thrust performances obtained by the mixing plane and the chorochronic approaches can be a motivation to investigate the possibility of imposing in the mixing plane model the conservation of averaged quantities other than the Riemann invariants. In fact this may reduce the gap with the unsteady simulations.

Otherwise, the next scheduled step in the CROR simulations with elsA is the application of the Time Spectral Method. This is a time integration method that will improve the calculation efficiency and open the possibility to extend the studies to installation effects as well as incidence working conditions. In fact, as mentioned in the introduction, the aeroelasticity dynamics between the blades and among them and the airframe, is one of the two major issues that this propeller configuration has to face to.

Subsequently the blade design will have a fundamental role in the noise emission reduction. Also for this purpose an acceleration in the convergence time of the unsteady calculations is needed.

Bibliography

[1] **Hager R. D.** and **Vrabel D.**, 1988 "Advanced Turboprop Project", NASA SP-495

[2] **Zachariadis A.** and **Hall Cesare A.**, 2009 "Application of a Navier-Stokes Solver to the Study of Open Rotor Aerodynamics", Whittle Laboratory, University of Cambridge

[3] **Strack W. C.**, **Knip G.**, **Weisbrich A. L.**, **Godston J.**, and **Bradley E.**, 1990, "Technology and Benefits of Aircraft Counter Rotation Propellers", NASA TM-82983

[4] **Dufour G.**, 2006, "Contributions à La Modélisation et au Calcul des Ecoulements dans les Conpresseurs Centrifuges: Application à la Conception par la Lois de Similitude", PhD thesis, ENSICA-DMF, Toulouse.

[5] **Callen H. B.**, 1985, "Thermodynamics and an Introduction to Thermostatistics", John Wiley, New York.

[6] **Galgani L.** and **Scotti A.**, 1970, "On subadditivity and convexity properties of thermodynamic functions", Pure and Applied Chemistry, vol. 22 .

[7] **Quartapelle L.** and **Auteri F.**, 2007, "Fluidodinamica", Appendice D, Politecnico di Milano.

[8] **LeVeque R. J.**, 2008, "Numerical Methods for Conservation Laws", Lectures in Mathematics, Birkäuser, Basel, Switzerland.

[9] **Baron A.**, 2005, "Fluidodinamica I", Parte 7, Politecnico di Milano.

[10] **Colin Y.**, 2007, "Simulation numérique de la distorsion générée par une entrée d'aire de moteur civil par vent de travers.", PhD thesis, CERFACS, Toulouse

[11] **Reynolds O.**, 1883, "An experimental investigation of the circumstances which determine whether the motion of water shall be direct and sinuous, and the law of resistance in parallel channels", Phil. Trans. Roy. Soc., 174:935-98.

[12] **Favre A.**, 1965, "Equations des gaz turbulents compressibles", J. Mec., Vol. 4.

[13] **Wilcox C. D.**, 1998, "Turbulence Modeling for CFD" 2nd Ed., DWC Industries, La Cañada.

[14] **Menter, F. R.**, 1994, "Two-Equation Eddy-Viscosity Turbulence Models for Engineering Applications", AIAA Journal, vol. 32, pp. 269-289.

[15] **Spalart, P. R.** and **Allmaras, S. R.**, 1992, "A One-Equation Turbulence Model for Aerodynamic Flows", AIAA Paper 92-0439.

[16] **Morkovin M. V.**, 1961, "Effects of compressibility on turbulent flows", Mechanics of Turbulence.

[17] **Kravchenko A.G.** and **Moin P.** 1997, "On the effect of numerical errors in large eddy simulations of turbulent flows", J. of Comput. Phys., 131: 310-322.

[18] **Hirsch C.**, 2009, "Numerical Investigation on Turbomachinery: State of the Art", VKI, LS 2009-08, Vrije Universiteit Brussel, Belgium.

[19] **Lazareff M.** and **Vuillot A.-M.** and **Cambier L.**, 2005, "ElsA: Theoretical Manual", ONERA, ELSA/STB-97020.

[20] **Hirsch C.**, 1988, "Numerics and Computation of Internal and External Flows", John Wiley & Sons, New York, NY.

[21] **Beam R. M.** and **Warming R. F.**, 1980, "Alternating direction implicit methods for parabolic equations with mixed derivative", Technical Report.

[22] **Chakravarhy S. R.**, 1988, "High resolution upwind formulation for the Navier-Stokes equations", VKI, LS, Von Karman Institute, Belgium.

[23] **Jameson A.** and **Schmidt R. F.** and **Turkel E.**, 1981, "Numerical Solutions of the Euler Equations by Finite Volume Methods Using Runge-Kutte Time Stepping Schemes", AIAA paper AIAA-81-1259.

[24] **Roe P. L.**, 1981, "Approximate riemann solvers, parameter vectors and difference schemes", Journal of Computational Physics, 43, 357-372.

[25] **Denton J. D.** and **Singh U. K.**, 1979, "Time Marching Methods for Turbomachinery Flow Calculation", VKI, LS 1979-7, Von Karman Institute, Belgium.

[26] **Arts A.**, 1982, "Etude de l'écoulement tridimensionnel dans un étage de turbine transsonique", PhD thesis, Université Catholique de Louvain and Von Karman Institute

[27] **Erodos J. I.** and **Alznert E.** and **McNally W.**, 1977, "Numerical solution of periodic transonic flow through a fan stage", AIAA Journal,15(11): 1559-1568

[28] **Adamczyk**, 1985, "Model Equation for Simulating Flows in Multistage Turbomachinery", ASME Paper No.85-GT-226

[29] **He L.**, 1990, "An Euler solution for unsteady flows around oscillating blades", Journal of Turbomachinery, 112(4): 564-571.

[30] **Giles M. B.**, 1988, "Calculation of unsteady wake/rotor interaction", Journal of Propulsion and Power, 4(4).

[31] **Giles M. B.**, 1990, "Stator/Rotor interaction in a transonic turbine", Journal of Propulsion and Power, 6(5).

[32] **Wang X.** and **Chen J. P.**, 2004, "A post-processor to render turbomachinery simulations", 43rd AIAA Aerospace Sciences Meeteng and Exhibit. Reno, number AIAA-2004-615.

[33] **Neubauer J.**, 2004, "Aérodynamique 3-D instationnaire des turbomachines axiales multiétages", PhD thesis, Université Paris 6.

[34] **Arnone A.** and **Pacciani R.**, 1996, "Rotor-stator interaction analysis using the Navier-Stokes equations and a multigrid method", Journal of turbomachinery, 118(4): 679-689.

[35] **Bardoux F.**, 2000, "Modélisation des interactions instationnaires rotor-stator en turbomachine multi-étages", PhD thesis, Ecole Centrale de Lyon, France.

[36] **Celik I.** and **Zhang W-M**, 1993, "Applicaton of Richardson Extrapolation to Some Simple Turbulent Flow Calculations", Proceedings of the Symposium on "Quantification of Uncertainty in Computational Fluid Dynamics", I. Celik et al. ASME Fluids Engineering Division Spring Meeting, Washington, C.C., June 20-24, pp. 29-38.